

GLASS FORMATION AND THERMAL HISTORY

by

PAULETTE IRENE KANTOR ONORATO

S.B., Massachusetts Institute of Technology  
1972

Submitted in partial fulfillment of the requirements  
for the degree of  
DOCTOR OF PHILOSOPHY  
at the  
Massachusetts Institute of Technology

June, 1977

Signature of Author ..... *Paulette I. K. Onorato* .....  
Department of Materials Science and Engineering  
May 5, 1977

Certified by ..... *[Signature]* .....  
Thesis Supervisor

Accepted by ..... *Harry Gates* .....  
Chairman, Departmental Committee on Graduate Students



## ABSTRACT

## GLASS FORMATION AND THERMAL HISTORY

by

PAULETTE IRENE KANTOR ONORATO

Submitted to the Department of Materials Science and Engineering on May 5, 1977 in partial fulfillment of the requirements for the degree of Doctor of Philosophy.

The kinetic treatment of glass formation is extended by the introduction of continuous cooling (CT) curves to estimate the cooling rates required to form glasses of various materials. The CT curves may be constructed from isothermal time-temperature-transformation curves following the approach originally suggested by Grange and Kiefer. The modified analysis is used to evaluate the effects of nucleating heterogeneities found in most liquids, those characterized by contact angles greater than about  $100^\circ$  have a negligible effect on the cooling rate required to form glasses. Heterogeneities with smaller contact angles can, however, have a significant effect on glass formation, with the critical cooling rate increasing with decreasing contact angle. The effects on glass formation of changes in the contact angle of nucleating heterogeneities are also compared with the effects of changes in the thermodynamic barrier to nucleation (in the crystal-liquid surface energy).

A simple method is suggested for the determination of the relative glass-forming behavior of materials. The critical cooling rate for glass formation can be determined through measurements of  $T_g$ , the melting point and the heat of fusion. The temperature at which the minimum time is required to form a given volume fraction of crystallites is found to be about 0.77 of the melting point for many materials and the viscosity at that temperature is crucial in predicting the minimum conditions for glass formation.

The theory of crystallization statistics is extended to include the quenching and subsequent reheating of glass-forming materials. The temperature of crystallization upon heating is predicted. Correlations between predicted and measured (by DTA or DSC) crystallization temperatures are good.

Heat flow calculations have been done which describe the two-stage cooling model for impact melts suggested by Simonds. The model involves initial phase of thermal equilibration between small unmelted particles (clasts) and the surrounding melt, and a second phase of heat loss from

the melt to the surroundings. In the first stage, the cooling is approximately logarithmic with time for about 90% of the overall change in melt temperature. The time to reach equilibrium is independent of the initial volume fraction of clasts. The dependence of the final volume fraction of clasts on initial temperature and initial volume fraction of clasts has been evaluated for several criteria for clast digestion. Small clasts are preferentially digested, resulting in an increase in the mean clast size. In the second stage of cooling, the boundary conditions have a large effect on the cooling behavior. Three sets of boundary conditions have been considered: (1) a melt sheet with essentially infinite cold insulating layers on both sides; (2) a melt sheet with infinite insulation on one side and radiation from the other side; and (3) a melt sheet with infinite insulation on one side and a thin cold blanket on top. Results showing the relationship between the time to cool to 1300°K and 900°K and the distance from the boundary are given for the first two sets of boundary conditions. The instantaneous cooling rates at these temperatures are also discussed as a function of distance from the boundary. Also considered is the thermal behavior with the third set of boundary conditions (with a 1 m cold blanket on top). At short times, the cooling behavior for the third set of boundary conditions is similar to that of the doubly-insulated case, while at long times the behavior is similar to the case with radiation at the boundary. The model was applied to the cooling of the Apollo 17 Station 6 Boulder and to the terrestrial impact site Manicouagan.

Non-isothermal diffusion in mineral systems is modelled to determine the thermal history of rocks. The partitioning of a solute between two phases has been modelled to determine the cooling rates of lunar samples 15065, 15075, 15076, and 15085 (18, 18, 25, 39 °C day<sup>-1</sup> respectively). The homogenization of zoned olivines has been modelled to determine the cooling rates of lunar samples 12002 and 15555 (10 and 5° C day<sup>-1</sup> respectively).

The effects of motion on the growth and dissolution of a bubble in a glass melt have been investigated. It is found that such motion can have a profound effect on the rates of growth and dissolution, particularly for large bubbles ( $\geq 0.1$  cm). Increasing the rate of motion, as by centrifugation, can further increase the rate of dissolution. The dissolution time and the growth rate can be dramatically changed by changing the relative saturation of the gas in the melt. The condition used to describe the concentration of gas at the bubble melt interface can have a significant effect on the dissolution time, particularly for small bubbles or under conditions where the concentration of gas in the melt is close to the solubility limit.

Thesis Supervisor: Donald R. Uhlmann  
Title: Professor of Ceramics and Polymers

TABLE OF CONTENTS

	<u>Page</u>
ABSTRACT	2
TABLE OF CONTENTS	4
LIST OF FIGURES	7
LIST OF TABLES	12
ACKNOWLEDGMENTS	13
I. INTRODUCTION	14
II. PREVIOUS WORK	15
A. Kinetics of Glass Formation	15
B. Thermal Histories	25
1. Impact Melts	26
2. Cooling Rate Indicators in Rocks	32
3. Elimination of Bubbles	37
III. PLAN OF WORK	49
IV. NUCLEATING HETEROGENEITIES AND GLASS FORMATION	51
A. The Model	51
B. Results	58
C. Discussion and Conclusions	65
V. A SIMPLIFIED MODEL FOR GLASS FORMATION	69
A. Model	69
1. Nucleation Barrier	72
2. Viscosity	75
B. Results	80
C. Discussion and Conclusions	82

	<u>Page</u>
VI. CRYSTALLIZATION STATISTICS	85
A. The Model	85
B. Results	91
C. Discussion and Conclusions	97
VII. THE THERMAL HISTORY OF IMPACT MELTS	103
A. The Model	103
B. Results	114
C. Discussion	128
D. Conclusions	140
VIII. COOLING RATES OF ROCKS	143
A. The Non-Isothermal Partitioning of a Solute in a Finite Couple	143
1. The Model	144
2. Results	148
3. Discussion	154
4. Conclusion	158
B. Diffusion in Olivine	160
1. The Model	160
2. Results	165
3. Discussion	168
4. Conclusion	172

IX. THE EFFECT OF MOTION ON THE FINING OF GLASS MELTS	173
A. The Model	173
B. Analytical Models	179
C. Results	182
D. Discussion	192
E. Conclusions	201
X. SUGGESTIONS FOR FURTHER WORK	203
APPENDIX A: SOURCES OF VISCOSITY AND GROWTH RATE DATA	205
APPENDIX B: THE THOMAS TRIDIAGONAL METHOD	206
APPENDIX C: DIFFUSION PROFILES IN OLIVINE	207
BIBLIOGRAPHY	211
BIOGRAPHICAL NOTE	218

LIST OF FIGURES

	<u>Page</u>
Fig. II-1	21
Isothermal time-temperature-transformation curves for salol corresponding to volume fractions crystallized of (A) $10^{-6}$ and (B) $10^{-8}$ (after Ref. 8).	
Fig. II-2	29
Relation between the extent of clast digestion and the initial melt temperature and initial fraction of clasts, assuming that all digestion takes place at the equilibrium temperature (after Ref. 35).	
Fig. IV-1	52
Measured and calculated growth rate vs. $T/T_E$ assuming parabolic least squares fit for lunar composition 65016, anorthite, and o-terphenyl.	
Fig. IV-2	54
Measured and calculated viscosity vs. $T/T$ relation assuming parabolic least squares fit for lunar composition 65016, anorthite, and o-terphenyl.	
Fig. IV-3	56
Schematic diagram illustrating construction of continuous cooling (CT) from isothermal time-temperature-transformation curves.	
Fig. IV-4	60
The TTT curves for $\text{Na}_2\text{O}\cdot 2\text{SiO}_2$ corresponding to a volume fraction crystallized of $10^{-6}$ . Curve A, homogeneous nucleation only, $\theta = 160^\circ$ , $\theta=120^\circ$ ; curve B, $\theta=100^\circ$ ; curve C, $\theta=80^\circ$ ; curve D, $\theta=60^\circ$ ; curve E, $\theta = 40^\circ$ .	
Fig. IV-5	61
The CT curves for $\text{Na}_2\text{O}\cdot 2\text{SiO}_2$ corresponding to a volume fraction crystallized of $10^{-6}$ . Curve A, homogeneous nucleation only, $\theta= 160^\circ$ , $\theta=120^\circ$ ; curve B, $\theta= 100^\circ$ ; curve C, $\theta= 80^\circ$ ; curve D, $\theta= 60^\circ$ ; curve E, $\theta= 40^\circ$ . Curves constructed from TTT curves following method showing in Fig. IV-3.	
Fig. V-1	79
$T_g/T$ normalization of viscosity of glass-forming liquids. •••• Least squares Vogel-Fulcher fit for lunar compositions.	
Fig. VI-1	92
Calculated $K_{g1}$ values vs. heating rate for $\text{SiO}_2$ , $\text{GeO}_2$ and salol.	

	<u>Page</u>	
Fig. VI-2	Measured and calculated crystallization temperature vs. heating rate relation of o-terphenyl.	94
Fig. VI-3	Measured and calculated $K_{g1}$ vs. heating rate relation of o-terphenyl, anorthite, and lunar composition 65016.	95
Fig. VI-4	Effect of cooling rate on calculated $K_{g1}$ vs. heating rate relation for lunar composition 70019.	96
Fig. VI-5	Calculated $K_{g1}$ values for anorthite as a function of assumed nucleation barrier.	98
Fig. VI-6	Constant cooling (CT) diagram for lunar composition 67975 corresponding to volume fraction crystallized of $10^{-6}$ , constructed from TTT diagram by technique described in Chapter IV.	100
Fig. VI-7	Nose of CT curve for lunar composition 67975 constructed from TTT diagram and from crystallization statistics.	101
Fig. VII-1	Mean temperature of melt. Initial temperature of melt = 1600 C. Initial volume fraction of clasts = 0.41.	115
Fig. VII-2	Mean temperature of melt. Initial temperature of melt = 1427 C. Initial volume fraction of clasts: (1) 0.61 (mean size = 1.94 mm); (2) 0.41 (mean size = 1.54 mm); (3) 0.40 (mean size = 1.97 mm); (4) 0.23 (mean size = 1.80 mm).	117
Fig. VII-3	Final volume fraction of clasts after first-stage cooling as a function of initial temperature and initial volume fraction of clasts.	118
Fig. VII-4	Temperature vs. distance in a representative 1 cm section in melt-clast system. Initial volume fraction of clasts = 0.21. Final volume of clasts = 0.19. Initial temperature = 1773 K. Equilibrium temperature = 1518 K. Times: _____ 0.0 sec; ---- 0.07 sec; — — 0.6 sec; — - 5.0 sec; ——— 30 sec.	120



	<u>Page</u>
Fig. VII-5	124
<p>Variation of temperature with time for various locations in a 10 m melt sheet covered by 1 m cold blanket on top. Distances measured from the boundary between melt sheet and cold blanket on top. A = at boundary; B = 2.5 m from boundary; C = 5 m from boundary; D = 10 m from boundary</p>	
Fig. VII-6	125
<p>Temperature profiles through a 10 m melt sheet for 3 sets of boundary conditions at times of <math>10^5</math>, <math>10^7</math>, and <math>10^8</math> sec. In all cases, a 30 m cold basement is taken below the melt; _____ = 30 m cold blanket above sheet; - - = 1 m cold blanket above sheet and radiation from top surface of blanket; ---- = radiation directly from top surface of melt.</p>	
Fig. VII-7	132
<p>Equilibrium temperature as a function of fractional clast digestion. dotted line - Simonds (35); triangles - assuming clasts melt only at liquidus of melt; solid circles - assuming 4 types of clasts melting at 4 distinct liquidus temperatures only; open circles - assuming 4 types of clasts, melting at 4 liquidus temperatures plus partial melting above solidus temperatures.</p>	
Fig. VII-8	135
<p>Time required for penetration of isotherms into 200 m melt sheet as a function of distance from edge.</p>	
Fig. VIII-1	149
<p>Solute concentration profiles for several times during cooling at <math>1000 \text{ K day}^{-1}</math> from 1400 K. <math>D_2(T) = 10D_1(T)</math>. Uniform initial solute distribution.</p>	
Fig. VIII-2	151
<p>Solute concentration profiles for several times during cooling at <math>3 \text{ K day}^{-1}</math> from 1400 K. <math>D_2(T) = 10D_1(T)</math>. Uniform initial solute distribution.</p>	
Fig. VIII-3	152
<p>Solute concentration profiles for several times during cooling at <math>3 \text{ K day}^{-1}</math> from 1400 K. <math>D_2(T) = 10D_1(T)</math>. Equilibrium initial solute distribution.</p>	

	<u>Page</u>
Fig. VIII-4 Solute concentration profiles for several times during cooling at $3 \text{ K day}^{-1}$ from 1400 K. $D_2(T) = D_1(T)$ . Equilibrium initial solute distribution.	153
Fig. VIII-5 Solute concentration ratio as a function of cooling rate.	155
Fig. VIII-6 Calculated composition profiles in grain of lunar composition 12002 at several temperatures during cooling at $10 \text{ C day}^{-1}$ from 1100 C.	166
Fig. VIII-7 Calculated composition profiles in grain of lunar composition 15555 at several temperatures during cooling at $5 \text{ C day}^{-1}$ from 1100 C.	167
Fig. VIII-8 Measured composition profiles and final composition profiles calculated for cooling rates of 1, 10 and $100 \text{ C day}^{-1}$ in lunar composition 12002.	169
Fig. VIII-9 Measured composition profiles and final composition profiles calculated for cooling rates of 1, 5, and $100 \text{ C day}^{-1}$ in lunar composition 15555.	170
Fig. IX-1 Diffusion field for moving bubble according to Levich (78)	176
Fig. IX-2 Radius of bubble (initially 0.1 cm) as a function of time $C_\infty/C_s = 1.0$ . Dashed lines indicate bubble would rise to surface before dissolving completely. (1) 1200 C, gravity = 1g; (2) 1200 C, gravity = 10g; (3) 1300 C, gravity = 1g; (4) 1300 C, gravity = 10g; (5) 1400 C, gravity = 1g; (6) 1500 C, gravity = 1g.	183

- Fig. IX-3 Radius of bubble (initially 0.1 cm) as a function of time.  $C_{\infty}/C_S = 0.9$ . 187  
 (1) 1200 C, gravity = 1g; (2) 1200 C, gravity = 10g; (3) 1300 C, gravity = 1g; (4) 1300 C, gravity = 10g; (5) 1400 C, gravity = 1g; (6) 1500 C, gravity = 1g; (7) 1400 C,  $C_O - C_S$ ; (8) 1400 C, Eq. IX-23; (9) 1400 C, Eq. IX-20.
- Fig. IX-4 Radius of bubble (initially 0.01 cm) as a function of time.  $C_{\infty}/C_S = 0.9$ . 188  
 (1) 1200 C, gravity = 1g; (2) 1200 C, gravity = 10g; (3) 1300 C, gravity = 1g; (4) 1300 C, gravity = 10g; (5) 1400 C, gravity = 1g; (6) 1500 C, gravity = 1g; (7) 1400 C,  $C_O - C_S$ ; (8) 1400 C, Eq. IX-23; (9) 1400 C, Eq. IX-20.
- Fig. IX-5 Radius of growing bubble as a function of time at 1400 C. 191
- Fig. IX-6 Height a growing bubble has risen as a function of time. 193  
 (1)  $A_O = 0.1$  cm,  $C_{\infty}/C_S = 1.1$ ; (2)  $A_O = 0.05$  cm,  $C_{\infty}/C_S = 1.1$ ; (3)  $A_O = 0.01$  cm,  $C_{\infty}/C_S = 1.1$ ; (4)  $A_O = 0.001$  cm,  $C_{\infty}/C_S = 1.1$ ; (5)  $A_O = 0.01$  cm,  $C_{\infty}/C_S = 1.2$ ; (6)  $A_O = 0.01$  cm,  $C_{\infty}/C_S = 1.05$ ; (7)  $A_O = 0.01$  cm,  $C_{\infty}/C_S = 1.1$ , gravity = 10g.
- Fig. IX-7 Time to dissolve vs.  $C_{\infty}/C_S$  at solid lines - Henry's Law at interface; dotted lines -  $C_O = C_S$  at interface; dashed line - stationary bubble according to Cable and Evans. 195
- Fig. IX-8 Time to dissolve vs. initial radius. Solid lines - Henry's Law at interface; dotted lines -  $C_O - C_S$  at interface; dashed lines - stationary bubble according to Cable and Evans. 198

LIST OF TABLES

	<u>Page</u>
Table IV-1 Lunar compositions investigated	59
Table IV-2 Effect of contact angle of heterogeneities ( $2 \times 10^7 \text{ cm}^{-3}$ ) on calculated critical cooling rates for glass formation.	63
Table IV-3 Effect of nucleation barrier on calculated cooling rates for glass formation (homogeneous nucleation)	64
Table V-1 Temperature of nose of TTT curve compared with melting point or liquidus temperature.	71
Table V-2 Relative undercoolings and $\sigma_M/\Delta H_{FM}$	76
Table V-3 Temperature and viscosity at the nose of TTT diagrams	81
Table V-4 Critical cooling rates for glass formation calculated from TTT and CT curves and using simplified method	83
Table VII-1 Clast digestion in Manicouagan	122
Table VII-2 Cooling of 10 m sheet from 1500°K	126
Table VII-3 Time required to cool to various temperatures for 200 m melt sheet	129
Table IX-1 Calculated dissolution times for oxygen bubbles in soda-lime-silicate melts under several sets of conditions	184
Table IX-2 The growth of oxygen bubbles in soda-lime-silicate melts under several sets of conditions	190

ACKNOWLEDGMENTS

I am indebted to Professor Donald R. Uhlmann for the many hours he has spent discussing the models presented in this thesis. He has been a source of countless suggestions and has enabled me to work with scientists of different backgrounds in areas of mutual interest. I would like to thank Dr. Chuck Simonds of the Lunar Science Institute for his interest in the development of heat flow calculations which describe his model for the thermal history of impact melts. To Dr. Larry Taylor of the University of Tennessee I am indebted for his measurements of diffusion profiles in olivine and his patience in helping me see a geologist's view of the importance of cooling rate determination. I thank Dr. Robert Hopper for his suggestions for the model of crystallization statistics. For their measurements of growth rate and viscosity and for stimulating discussions, I am grateful to Drs. George Scherer and Lisa Klein and Mrs. Carol Pettyjohn. For DTA measurements of lunar compositions I thank Professor Alex Reucoluschi of the Universite de Paris at Orsay. I am indebted to Dr. Peter Vergano and Owens-Illinois for their fellowship in Materials Science.

A deeply appreciative thank you also must go to Linda Sayegh for typing this thesis, especially all the equations.

To Joe, my husband, I give my love. His patience and understanding have encouraged me to persevere when I was tempted to quit.

To my Lord and Savior Jesus Christ I owe everything. It is he who enables me and it is to His glory that I dedicate this thesis.

## I. INTRODUCTION

Knowledge of the effect of thermal history on the state of crystallinity in a system is useful to the glass scientist in predicting the glass-forming behavior of materials and to the geologist in determining the origin of lunar and terrestrial rocks. Several approaches have been taken to determine the criteria for glass formation in a variety of materials and the thermal histories of specific lunar and terrestrial samples. To be considered are the effects of nucleating heterogeneities, simply measurable parameters, and nonisothermal histories on glass formation. In completely crystalline bodies, the effect of thermal history on solid state diffusion and homogenization has been investigated. Thermal histories have been calculated for lunar and terrestrial impact melt sheets with specific geometries and initial conditions of physical interest. These calculations are combined to provide a description of the thermal histories, and hence the origins, of a number of rocks.

The effect of several factors, including temperature and rate of bubble movement, on the fining of silicate melts has been investigated. A model has been developed which takes into account the effect of motion on the growth and dissolution of gas bubbles in glass melts.

## II. PREVIOUS WORK

### A. Kinetics of Glass Formation

The problem of glass formation has been approached from several points of view, with attention variously directed to structural (1,2,3) thermodynamic (4-7), and kinetic (8-12) aspects of the problem. Only kinetic treatments will be discussed here because of the potential which they offer for obtaining quantitative predictions of glass-forming behavior and because the question of glass formation primarily involves kinetic considerations. That is, nearly any liquid will form a glass if cooled sufficiently rapidly to a sufficiently low temperature, and will form a crystalline or partly crystalline body if cooled too slowly.

The essential question to be asked in considering glass formation is not whether a material will form an amorphous solid when cooled in bulk form from the liquid state, but how fast must it be cooled. Different models use different criteria as to the definition of what constitutes a glass. Sargeant and Roy (10) defined their critical cooling rate as "the rate which will not allow the growth of a  $10^{\circ}$  nucleus within a  $10^{\circ}$  interval." The results were very approximate which is not surprising considering the physical basis of the model. Specifically, the model assumes that the critical cooling rate is proportional to the melting point and to the molecular mobility at the melting point. While these are undoubtedly important quantities in describing glass formation, they are not sufficient to predict the critical cooling rate. Turnbull (12) and Vreeswijk et al. (9) assumed that the condition for

glass formation was the absence of even a single nucleation event

$$n = v \int_0^t I_o dt \quad n < 1 \quad (\text{II-1})$$

In both models, only homogeneous nucleation was considered. Turnbull used the expression for steady state nucleation rate

$$I_o = \frac{K}{\eta} \exp \left[ \frac{-16}{3kT} \frac{\sigma^3}{(\Delta G_v)^2} \right] \quad (\text{II-2})$$

where  $\sigma$  is the crystal-liquid specific surface free energy and  $G_v$  is the difference between the liquid and crystal phases of the standard Gibbs free energy per unit volume. Turnbull used the approximation that

$$\Delta G_v = \Delta H_v \frac{\Delta T}{T_E} \quad (\text{II-3})$$

where  $\Delta H_v$  is the latent heat of fusion per unit volume,  $T_E$  is the melting point, and  $\Delta T = T_E - T$  is the undercooling. This holds well for metals, but for large departures from equilibrium, the differences in enthalpy and entropy between phases must be taken into account.  $\Delta G_v$  may then be expressed as:

$$\Delta G_v \approx \Delta H_v \frac{\Delta T}{T_E} \frac{T}{T_E} \quad (\text{II-4})$$

This was the approximation used by Vreesswijk et al.

Turnbull's steady state nucleation frequency was then

$$I_o = \frac{K}{\eta} \exp \left[ \frac{-16\pi}{3} \frac{\alpha \beta T_E^2}{T \Delta T} \right] \quad (\text{II-5})$$



while that of Vreeswijk was

$$I_{\infty} = \frac{K}{\eta} \exp \left[ -\frac{16\pi}{3} \frac{\alpha^3 \beta T_E^5}{\Delta T^2 T^3} \right] \quad (\text{II-6})$$

where

$$\alpha = \frac{(N_0 \bar{V}^2)^{1/3}}{\Delta H_f} \quad (\text{II-7})$$

$$\beta = \frac{\Delta H_f}{RT_E} = \frac{\Delta S_f}{R} \quad (\text{II-8})$$

Results of droplet nucleation experiments on a variety of materials using Eqn. (II-5) with  $K = 10^{30}$  and  $\eta \approx 10^{-2}$  indicate  $\alpha \approx 0.4-0.5$  for metals and  $\alpha \approx 1/3$  for non metals (13). Vreeswijk et al. took  $\alpha = 0.32$ , suggested that the transient time in nucleation is important, and used the expression to determine a critical cooling rate.

$$I_0(t) = I_{\infty} \exp\left(-\frac{\tau}{t}\right) \quad (\text{II-9})$$

Turnbull's results confirmed the observation that in pure metals copious nucleation of crystals should be expected and a glass would not be formed even at the fastest attainable cooling rates ( $10^8 \text{ K/sec}^{-1}$ )-- save for very small samples or for materials with exceptionally high glass transition temperatures. The results of Vreeswijk et al. provide a basis for grouping materials into classes of good or bad glass-formers; however upon closer examination, the results indicating relative glass-forming ability of different materials are not in accord with experience.

Dietzel and Wickert (11) use the term "glassiness" for the

reciprocal of the growth rate, and carried out an extensive study of growth rates for various compositions in the  $\text{Na}_2\text{O-SiO}_2$  system. No quantitative relation between "glassiness" and cooling rates required to form different compositions as glasses was given. The work did list several factors which are critical in glass formation: (1) high viscosity; (2) large compositional difference from compounds noted in the phase diagram; and (3) low liquidus temperature. Suzuki and Saito (14) neglected the nucleation processes and considered only the growth rate and the rate of heat liberation at the solid-liquid interface. They defined the critical cooling rate for glass formation as that which will not allow the growth of a  $50 \text{ \AA}$  nucleus. The heat evolved during the growth of a  $50 \text{ \AA}$  nucleus is very small and could easily be absorbed by the surrounding melt. Furthermore, in many glass-forming systems, the growth process is limited not by the transport of heat away from the interface, but by interface kinetics (15).

The models mentioned thus far take into account either nucleation or growth and thus have only limited applicability. To include both aspects of the crystallization process, Uhlmann (8) adopted the formal theory of transformation kinetics (16, 17) which describes the fraction of a phase transformed in a given time at a given temperature. He assumed that the growth rate  $u$  and the homogeneous nucleation frequency  $I_v$  are not functions of time. The volume fraction transformed is

$$X = \frac{\pi}{3} I_v u^3 t^4 \quad (\text{II-10})$$

where  $X$  is small and the crystallites do not impinge on each other. The homogeneous nucleation frequency per unit volume is

$$I_v = N_v^0 v \exp - \frac{1.024T_E}{T^3 \Delta T^2} \quad (\text{II-11})$$

$$v = \frac{kT}{3\pi a_o^2 \eta} \quad (\text{II-12})$$

from the Stokes-Einstein equation,  $N_v^0$  is the number of single molecules per unit volume and  $a_o$  is the molecular diameter. In obtaining this relation, it was assumed that the free energy of forming the critical nucleus is  $50 kT$  at  $\Delta T/T_E = 0.2$  from the results of Turnbull and that  $\Delta G_v = \Delta H_{fv} \Delta T/T_E T/T_E$ . More recent measurements of nucleation frequency indicate that the nucleation barrier for lunar glasses is higher, about  $55$  to  $65 kT$  at  $\Delta T/T_E = 0.2$  (18).

This model does not include heterogeneous nucleation and therefore provides a minimum critical cooling rate for glass formation. The growth rate was expressed

$$u = f v a_o \left[ 1 - \exp \left( - \frac{\Delta H_{fm} \Delta T}{RT T_E} \right) \right] \quad (\text{II-13})$$

$f = 1$  for materials with small entropies of fusion ( $\Delta H_{fm}/T_E < 2R$ ) in which normal growth is expected;  $f \sim 0.2 \Delta T/T_E$  for materials with a large entropy of fusion ( $\Delta H_{fm}/T_E > 4R$ ) in which growth should take place at steps on the interface.

To determine the critical cooling rate for different materials, time-temperature-transformation (TTT) curves were constructed using

equations (II-10, II-13). Example of such curves are shown in Fig. II-1, for volume fractions crystallized of  $10^{-6}$  and  $10^{-8}$  in salol. In constructing these curves, the time required to form a given fraction of crystalline material is calculated at a given temperature and the calculation is repeated at other temperatures. The nose of a TTT diagram, which corresponds to the least time for the given volume fraction to crystallize, results from a competition between the driving force for crystallization, which increases with decreasing temperature, and the mobility, which decreases with decreasing temperature. The critical cooling rate was taken as:

$$\left. \frac{dT}{dt} \right|_{\text{critical}} = \frac{\Delta T_n}{\tau_n} \quad (\text{II-14})$$

where  $\Delta T_n = T_E - T_n$ ;  $T_n$  is the temperature at the nose of the TTT diagram and  $\tau_n$  is the time of the nose.

Estimates of the critical cooling rate employing equation (II-10) overestimate the difficulty of forming a glass. Equation (II-10) implicitly assumes that the crystallization kinetics over the full range of temperature between the melting point and the nose of the TTT curve are as rapid as the temperature of the nose. Grange and Keifer (19) developed a method for the construction of constant cooling (CT) diagrams from which a better estimate of the critical cooling rate can be determined. This technique will be covered in Chapter IV.

The models mentioned thus far which include nucleation take into account only homogeneous nucleation. In many cases, the nucleation event

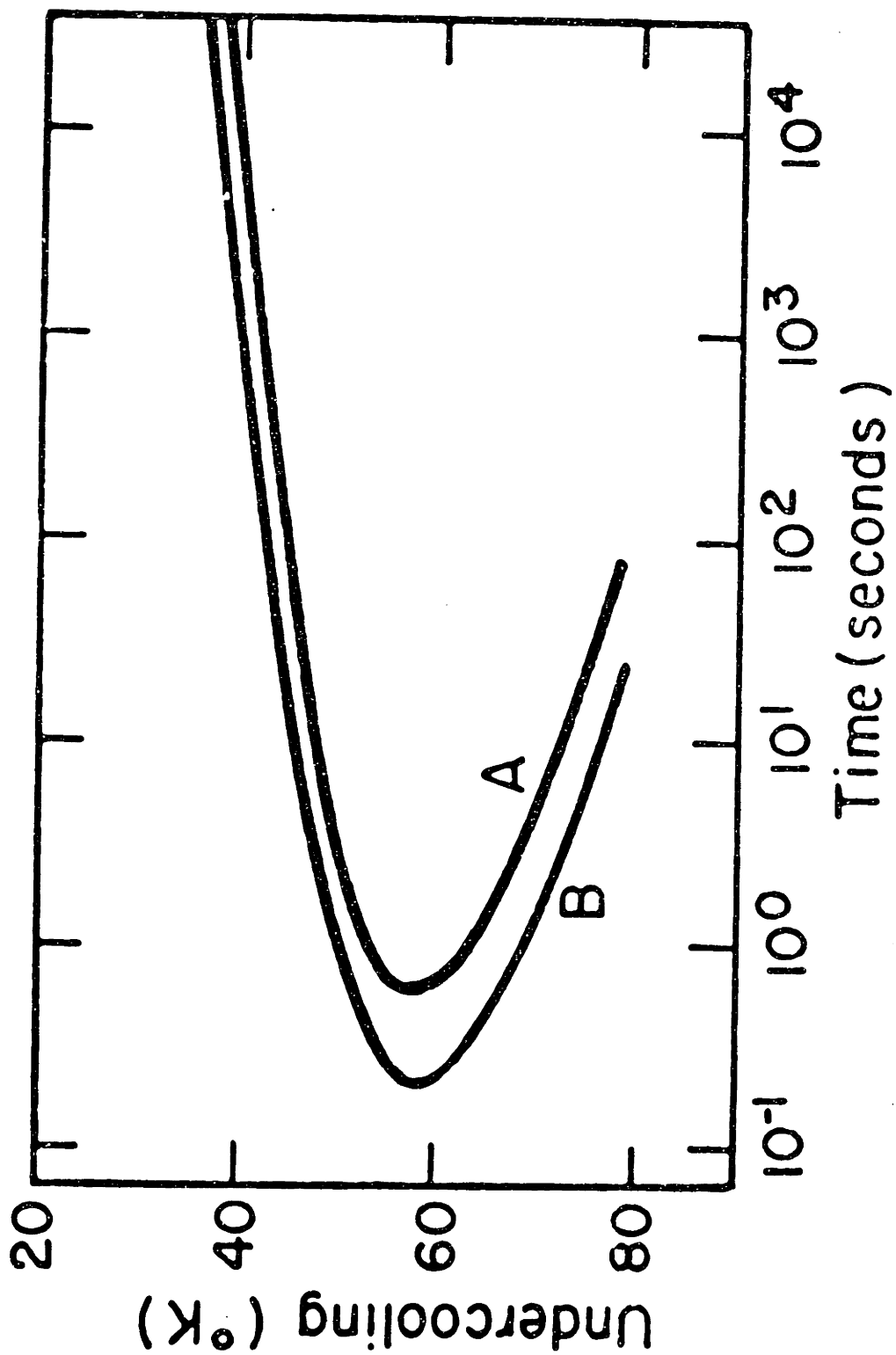


Figure II-1 - Isothermal time-temperature-transformation curves for salol corresponding to volume fractions crystallized of (A)  $10^{-6}$  and (B)  $10^{-8}$  (after Ref. 8).

takes place heterogeneously on container walls, impurity particles, or structural imperfections (20). Assuming a spherical cap nucleating on a flat surface, the nucleation barrier is

$$\Delta G^{\text{HE}*} = \Delta G^* [(2 + \cos\theta)(1 - \cos\theta)^2] / 4 \quad (\text{II-15})$$

where  $\Delta G^*$  is the homogeneous nucleation barrier and  $\theta$  is the contact angle between the nucleus and the substrate. The nucleation barrier is decreased because when a nucleus forms on a substrate, surface energy contribution to the free energy is decreased.

The heterogeneous nucleation frequency is

$$I_{\text{v}}^{\text{HE}} = A_{\text{v}} N_{\text{s}}^{\text{o}} \nu \exp - \frac{\Delta G^* [(2 + \cos\theta)(1 - \cos\theta)^2]}{4kT} \quad (\text{II-16})$$

where  $A_{\text{v}}$  is the area of nucleating substrate per unit volume of the melt,  $N_{\text{s}}^{\text{o}}$  is the number of molecules per unit area of substrate. Many studies of homogeneous nucleation (21-24) have indicated that a division of a specimen into 10-20  $\mu\text{m}$  diameter droplets is sufficient to ensure that about 99% of them do not contain a nucleating heterogeneity. These results indicate a density of heterogeneities of about  $2 \times 10^7 / \text{cm}^3$ . In many cases this value represents an upper limit to the expected density of nucleating heterogeneities as many materials--e.g., the transition metals and most lunar compositions--are characterized by appreciably smaller concentrations due to their greater fluxing ability.

The above models developed from transformation kinetics have proved to be very useful in predicting the glass-forming ability at different

materials. They provide, however, no direct information about the size and number distributions of crystals in a nominally glassy or partly devitrified body subject to a given thermal history. A later development of the analysis (25) does provide such information. It introduces a crystal density function  $\psi(r,t,R)$  to represent the distributions of the crystallites which form within a body subject to a given thermal history. This function is defined such that the number of crystals,  $dn$  in the volume  $dv$  at position  $r$  having radii between  $R$  and  $R+dR$  at time  $t$  is:

$$dn = \psi(r,t,R) \, dv dR \quad (\text{II-17})$$

This function provides essentially complete statistical information about the state of crystallinity in a sample; and the analysis is predictive in representing distributions of crystal sizes. These results were applied to the cooling of spheres of partially devitrified lunar glasses cooled by radiation (26). It was shown that for a given thermal history  $T(t)$  and growth rate  $U(T(t))$  there exists a one-to-one correspondence between  $R(r,t,t_0)$  and  $t_0$ . Here  $t_0$  is the time at which a particular crystal nucleated. The problem can be inverted and the calculations used to determine the thermal history of a sample from measurement of the crystal distributions. This model was applied to the determination of the thermal history of lunar samples 60095 and 14259. The number density and volume fraction crystallized were determined at various locations in a semi-transparent sphere cooling by radiation and in a quenched opaque slab cooling by conduction. It was assumed that  $\Delta G^* = 50 \, kT$  at  $\Delta T/T_E = 0.2$ . The results overestimated the difficulty of forming a body of glassy

material which was observed in the lunar sample. It was suggested that a nucleation barrier of 60-65 kT is sufficient to describe the experimental observations. Even without detailed measurements of crystal size distributions, this method can be used to model the extent of crystallization due to complex thermal histories. The volume fraction crystallized at  $(r,t)$  is

$$F_v(r,t) = \int_0^t \frac{4}{3} \pi R(r,t,t_0)^3 I_v[T(r,t_0)] dt_0 \quad (\text{II-18})$$

Hruby (27) has suggested a simple method of evaluating the glass-forming tendency of materials on the basis of the relative position of the glass transformation temperature,  $T_g$ , the melting temperature  $T_E$ , and the temperature of recrystallization upon heating  $F_v$ . He made three assumptions:

1. at  $T_g$  all glasses are in comparable states
2. The interval  $T_r - T_g$  is directly proportional to the glass-forming tendency
3. The interval  $T_E - T_r$  is inversely proportional to the glass-forming tendency.

He defined a parameter which is a numerical measure of the glass forming tendency

$$K_g = \frac{T_{cr} - T_g}{T_E - T_{cr}} \quad (\text{II-19})$$

Thornburg (28) pointed out the dependence of this parameter on heating rate and Lasocka (29) showed its dependence on quenching rate as



well as heating rate.

#### B. Thermal Histories

In order to confirm the applicability of the above theories to materials of unknown thermal history it is necessary to model the thermal history of these materials, apply the theory of transformation kinetics and compare the predicted degree of crystallinity to that which is observed. Simonds (30) has proposed a model to describe the origin of certain lunar and terrestrial samples which contain unmelted particles (clasts) in a glassy or partly crystalline matrix. Simonds suggested that the melt produced by a meteoritic impact is mixed with unmelted particles. These particles serve as heat sinks and quench the melt to some equilibrium temperature. In the process, some of the clasts melt. The fraction of clasts remaining and equilibrium temperature are functions of the initial melt temperature and the volume fraction of clasts initially present. Thereafter, the melt sheet as a whole cools by conduction and radiation to the surrounding. If the cooling rate is sufficiently rapid the melt will form a glassy or partly crystalline matrix.

When cooling rates are so low the sample becomes completely crystalline, it is still possible to determine cooling rates using the model of zoning suggested by Taylor (31). Concentration gradients within olivine grains can only persist if the cooling rate is sufficiently rapid. Diffusion in the solid state would promote homogenization within the grain.

Another aspect of the microstructure which bears consideration is the absence of bubbles in the clastic lunar and terrestrial rocks produced by impact events. It remains to be demonstrated whether the time-at-temperature is sufficient for the removal of substantially all gas bubbles and for the observed degree of homogenization.

#### 1. Impact Melts

Simonds (30) has proposed a two-stage cooling model to describe the thermal history of impact melts. The initial stage of melt cooling involves heat transfer between superheated silicate liquid and enclosed cold clasts. The second stage of cooling involves loss of heat from the melt sheet to its surroundings. Such sheets of impact melt are formed at mixtures of molten rock, fused near the point of impact, which is violently mixed with fine grained cold clastic debris. The fluid mixture is then laid down as a horizontal layer in or near the crater of excavation. If the cooling rate during the first-stage cooling is sufficiently high that the nose of the continuous cooling curve for  $X = 10^{-6}$  for the matrix material is avoided (32), and if the equilibration temperature is sufficiently low that detectable crystallization does not take place during the much slower second-stage cooling, then a glassy matrix breccia be formed. A breccia is a rock consisting of smaller fragments of rock embedded in a matrix. With progressively slower cooling and higher equilibration temperatures, breccias with partly crystalline matrices and eventually completely crystalline rocks will be formed. A quantitative analysis is made of the physical model suggested by

Simonds and the consequences of ranging the clast content, the initial temperature of the melt and the boundary conditions are explored. The model is applied to two impact structures, one lunar and one terrestrial.

The Apollo 17 Station and Boulder, which is actually a series of blocks, lies at the foot of the North Massif in the Taurus-Littrow Valley on the Moon. Simonds (30) argues that the boulder is a partial section through a horizontal sheet of impact melt, about 10 m thick, at least 1 km. long, and lying about 1/3 of the way up to 2 km high massif. The boulder is inferred to consist of a series of units differing in vesicularity and clast content (33); but the narrow range in chemical composition (30) and ages (34) suggest that all are part of a single melt sheet.

The Manicouagan structure is located 800 km northeast of Montreal. It has a diameter of 65 km and an original thickness estimated as 239 m. Its age has been measured as 214 million year (35). The structure is believed to have resulted from a meteorite impact which, due to its large kinetic energy (estimated as  $10^{30}$  ergs), melted about 200-600 km<sup>3</sup> of crustal material.

There is evidence (35) that this huge mass of rock cooled much more quickly than would be allowed by simple cooling to the surroundings. The clast distribution is not uniform; rather, there exists a gradient in the clast content such that the fraction of clasts decreases with increasing height above the basement rock.

In an analysis relevant to cooling a melt by heat flow to cold clasts, Carslaw and Jaeger (36) considered the change with time in the temperature of molten material upon introducing a spherical particle initially at a different temperature. They also considered the change in temperature of the sphere as a function of time. The melt was assumed to be well-stirred, i.e., to have infinite thermal conductivity. The effects of various volume fractions of particles can be evaluated by considering different ratios of the heat capacity of the particle to that of the melt. According to this model, the time for thermal equilibration increases somewhat as the volume fraction of particles decreases.

Simonds et al. (35) advanced a simplified model in which it was assumed that all digestion of clasts takes place at the temperature of thermal equilibrium reached at the end of the first-stage cooling. The equilibration temperature was determined by a simple energy balance, and the fraction of clasts melted was equated with the difference between the equilibration temperature and the solidus divided by the difference between the liquidus and solidus temperatures. Simonds et al. provided a graphical representation of the enthalpy of solid, partially melted, and completely melted silicates as a function of temperature.

The model was used to estimate the equilibrium temperature for various combinations of melt temperatures and initial volume fractions of clasts (Fig. II-2) and was applied to the formation of lunar rocks. It was suggested that for a given melt composition with a given glass-forming tendency, the model could be used to describe the microstructures

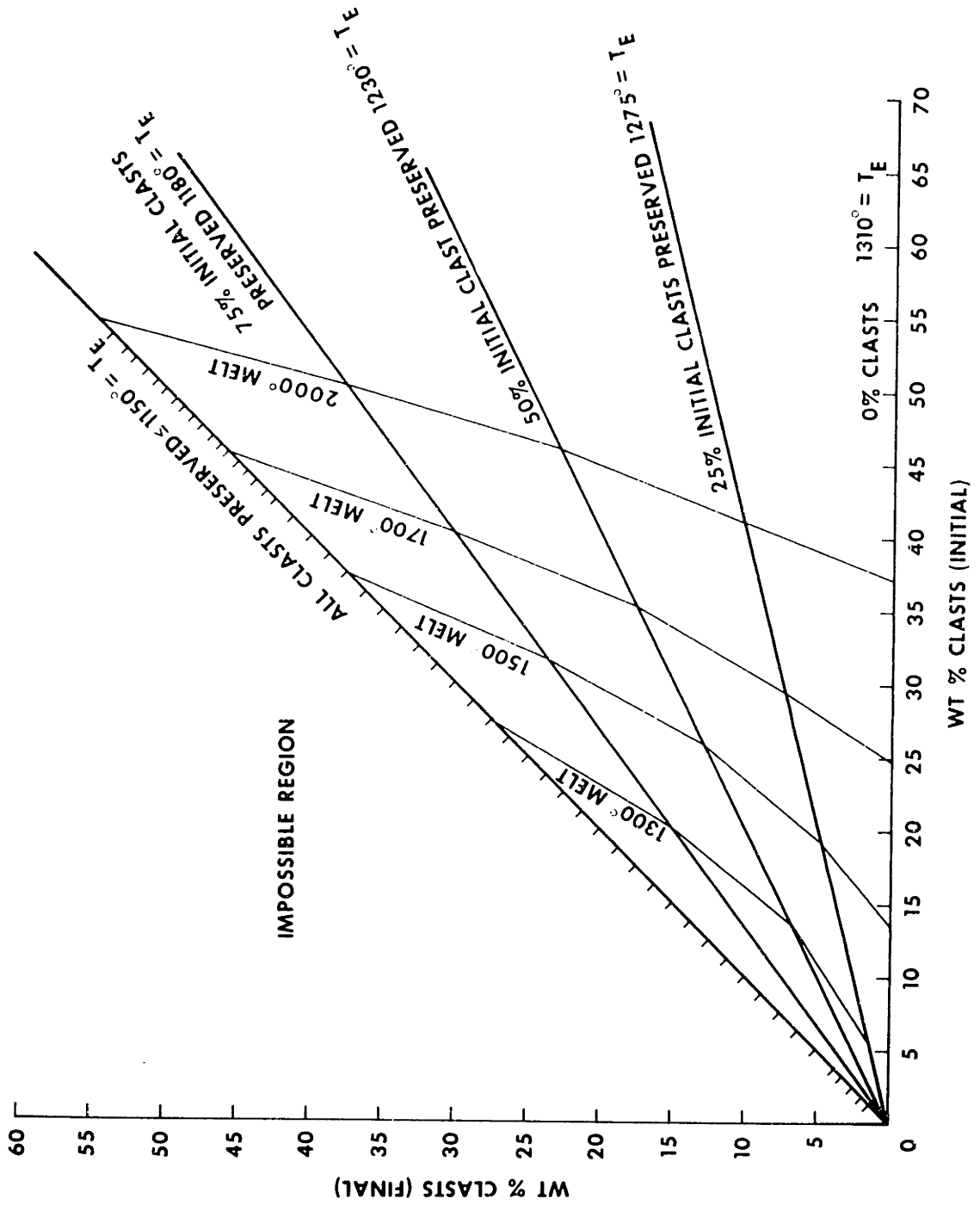


Figure II-2 - Relation between the extent of clast digestion and the initial melt temperature and initial fraction of clasts, assuming that all digestion takes place at the equilibrium temperature (after Ref. 35).

of materials produced in a melt sheet, from glassy matrix breccias to clast-free impact melts which are completely crystalline.

Analyses of heat flow appropriate for second-stage cooling, where a melt sheet loses heat to its surroundings, have been advanced by several authors. In general the equation to be solved is the one dimensional heat flow equation:

$$\rho C_p \frac{\partial T}{\partial t} = \frac{\partial}{\partial x} \left( K \frac{\partial T}{\partial x} \right) \quad (\text{II-20})$$

where K is the thermal conductivity and  $\rho$  is the density.

a. The treatment of a cooling intrusion by Lovering (37), who considered an intrusion as an infinite slab of finite thickness and initially uniform temperature, which is intruded into a medium which is also at a uniform temperature. Both the intrusion and the surroundings were assumed to have the same constant thermal conductivity. The latent heat of fusion was not explicitly included in the analysis. It was suggested, however, that the effects of latent heat might be approximated by increasing the scale or initial temperature of the melt sheet. The former modification would produce results that are applicable at short times and the latter at long times. The error function solution obtained by Lovering is an exact solution to the simplified problem.

b. The analysis of temperature distributions in cooling igneous bodies by Jaeger (38,39), who provided a highly insightful and rather comprehensive, albeit somewhat simplified, theory of heat flow in an magma initially at a uniform temperature. The magma was taken as

cooling by conduction into country rock which has the same thermal properties as the magma. Realistic complications were considered, including two finite sheets in contact, a finite sheet between two thick cold bodies, and flows with irregular boundaries. In the latter paper, it was suggested that the latent heat (L) could be included by replacing the heat capacity in the temperature range between the liquidus ( $T_L$ ) and the solidus ( $T_S$ ) with:

$$C_p' = C_p + L/(T_L - T_S) \quad (\text{II-21})$$

According to Jaeger (39), near the boundaries between the melt and the country rock, the distance of an isotherm from the boundary is proportional to  $t^{1/2}$ . Hence the mean cooling rate at a given temperature, defined as the temperature range through which a point cools divided by the time it takes to cool through this range, is proportional to  $Y^{-2}$ , where Y is the distance from the boundary.

Provost and Bottinga (40) numerically solved the heat flow equation for a lava flow of initially uniform temperature cooling by radiation or the upper surface and conduction into a cold basement. The top of the flow was assumed to radiate as a black body, with the energy loss given by the Stefan-Boltzmann law:

$$K \frac{\partial T}{\partial x} = \sigma (T_T^4 - T_V^4) \quad (\text{II-22})$$

Here  $\sigma$  is Stefan's constant,  $1.355 \times 10^{-12}$  cal/sec  $\text{cm}^2 \text{ } ^\circ\text{K}^4$ ;  $T_T$  is the temperature of the top surface of the flow; and  $T_V$  is the equivalent temperature of space above the flow. The thermal conductivity of the fluid lava was taken as infinite relative to that of the surroundings,

i.e., convection in the melt was assumed to reduce thermal gradients and produce an isothermal melt.

Provost and Bottinga considered the growth rate of crusts developed in both the upper and lower regions of the flow, and included the effects of latent heat generated at the crust-melt boundaries (the thermal flux was equated to the rate at which the heat of fusion is liberated:

$K \frac{\partial T}{\partial x} = L\rho \frac{dY}{dt}$ . They did not consider cooling rates directly, rather they derived an expression for the velocity at which the upper crust (near the radiating boundary) grows:

$$\frac{Y}{t} \propto Y^{-0.89} \quad \text{or} \quad Y \propto t^{0.53} \quad (\text{II-23})$$

The results were compared with observed isotherms in the upper crusts of two Hawaiian Lava lakes and to Apollo 11 basalts.

## 2. Cooling Rate Indicators in Rocks

When a rock is completely crystalline, it is difficult to apply transformation kinetics to determine the cooling history. Various other techniques have been used including the examination of phase-equilibria. The relaxation of compositional gradients brought about by segregation during normal freezing, and the subsolidus partitioning of minor constituents between two phases.

Walker et al. (41) studied the cooling history of lunar sample 12002, a rock containing coarse crystals in a finer-grained matrix and consisting of olivine, augite and small amounts of feldspar. They found that under



equilibrium conditions, phases crystallize in the order olivine, chromium spinel, pyroxene, plagioclase, and ilmenite. Under non-equilibrium, controlled cooling conditions, ilmenite and plagioclase reverse their order of appearance and silica crystallizes in the matrix. Comparing the microstructure of 12002 with the results of controlled cooling rate experiments, they deduced an initial cooling rate of about  $1 \text{ K hr}^{-1}$ , which subsequently decreased by at an order of magnitude or more. They suggested that the change in cooling rate was probably continuous, rather than relatively abrupt as suggested by the two stage cooling model for impact melts. The cooling rates during the first stage of Simonds model are much faster than  $1 \text{ K hr}^{-1}$ .

Studies of distribution coefficients during solidification and partitioning in two solid phases are based on the same simple theory. Let  $\mu_i$  be the chemical potential of a component in phase  $i$ . Then

$$\mu_i = \mu_i^\circ + RT \ln a_i \quad (\text{II-24})$$

where  $\mu_i^\circ$  is the standard state chemical potential and  $a_i$  is the activity. At equilibrium, the chemical potential of each component must be the same in both phases (solid and liquid, or two solid phases). Thus

$$\frac{a_1}{a_2} = \exp [-(\mu_1^\circ - \mu_2^\circ)/RT] \approx K_1(T) \quad (\text{II-25})$$

If  $x_i$  is the mole fraction of a species in phase  $i$ , and if the activity coefficients  $\gamma_i$  defined by  $a_i = \gamma_i x_i$  are constant over the range of composition involved,

$$\frac{X_1}{X_2} = \frac{Y_2}{Y_1} K_1(T) = K_2(T) \quad (\text{II-25})$$

If solidification is rapid and there is not enough time for substantial diffusion in the solid, there will be compositional gradients after solidification even in a system which exhibits complete solid solubility. One system of this type is the forsterite-fayalite ( $\text{Mg}_2\text{SiO}_4$ - $\text{Fe}_2\text{SiO}_4$ ) system, which is very common in lunar and terrestrial rocks and which exhibits zoning within individual olivine ( $(\text{Mg,Fe})_2\text{SiO}_4$ ) grains.

There are two sets of isothermal diffusion data for this system. Misener (42) found that the dependence of the interdiffusion coefficient,  $\tilde{D}$ , upon temperature and composition is given by

$$\tilde{D} = (1.53 \pm 0.25 - 1.12N_2) \times 10^{-2} \exp\left(-\frac{49.83+4.5+9.05N_2}{RT}\right) \quad (\text{II-26})$$

where  $N_2$  is the atomic fraction of Mg. This applies in the temperature range  $900 \leq T \leq 1100$  and the composition range  $0.10 \leq N_2 \leq 0.60$ . He also found that the interdiffusion coefficient is a function of crystallographic direction  $\tilde{D}_a > \tilde{D}_b$ , and that  $\tilde{D}$  decreases with increasing pressure. He did not take into account the oxygen fugacity, which is of importance in dealing with transport in this system.

Buening and Buseck (43) did take the oxygen fugacity into account. They found that the interdiffusion coefficient in olivine in the  $\vec{c}$  direction at  $p_{\text{O}_2} = 10^{-12}$  is given by:

$$\tilde{D}_c = \exp[-0.045 X_{\text{Fe}_2\text{SiO}_4} - 3.47] \exp -[(2.143 \text{ ev} - 0.0096 X_{\text{Fe}_2\text{SiO}_4})/kT]$$

(II-27a)

at  $T > 1125\text{C}$

and

$$\tilde{D}_c = \exp[-0.0501 (X_{\text{Fe}_2\text{SiO}_4})^{-14.03}] \exp -[(1.373 \text{ ev} - 0.0095 X_{\text{Fe}_2\text{SiO}_4})/kT]$$

(II-27b)

at  $T < 1125\text{C}$

They also found that the anisotropy of the diffusion coefficient increases with decreasing temperature,  $D_a$  being less than  $D_c$  by a factor of about 3.4 at 1100 C, 4.0 at 1050 C and 4.7 at 1000 C. They also found that the interdiffusion coefficient is a function of the oxygen fugacity

$$D \propto P_{\text{O}_2}^{0.172} \quad \text{(II-28)}$$

with an accuracy of  $\pm 0.022$  in the exponent. This was consistent with a vacancy diffusion mechanism by which  $D$  should be proportional to  $P_{\text{O}_2}^{1/6}$ .

When a small amount of solute is partitioned between two phases in a cooling system, the inhomogeneity can increase rather than decrease with time. Taylor and Uhlmann and their co-workers (44) advanced a simplified model to describe partitioning under continuous cooling conditions, and a more realistic and detailed treatment of isothermal partitioning. Partitioning is controlled by both the partition coefficient and the diffusion coefficient, both of which may be functions of temperature and therefore, in the nonisothermal case, time.

Analytical solutions were obtained for a finite isothermal system. The system was assumed to be in equilibrium at the interface, i.e.:

$$C_1(0^-, t) = K C_2(0^+, t) \quad (\text{II-29})$$

where the subscript indicates the phase. The diffusivity was taken as constant within each phase.

The solutions to the isothermal partitioning problem are not directly applicable to the determination of the thermal histories of lunar or terrestrial samples, but are of utility in interpreting laboratory isothermal partitioning experiments aimed at providing estimates of  $K(T)$ ,  $D_1(T)$  and  $D_2(T)$ .

The simplified analysis (44) was used to estimate the cooling rate of a lunar sample whose observed partitioning ratio equals that of an isothermal laboratory experiment carried out at temperature  $T_0$ . It was assumed that the characteristic diffusion distance below  $T_0$  and after time  $t_0$  is approximately the grain size  $X_g$  of the sample:

$$\left[ \int_{t_0}^{t_f} D(t') dt' \right]^{1/2} = X_g \quad (\text{II-30})$$

If the cooling were faster, less partitioning could occur at temperatures below  $T_0$  over a region of size  $X_g$  and the observed partitioning ratio would correspond to a higher temperature. A constant cooling rate,  $a$ , and an Arrhenius form for the diffusivity  $D = D_0 \exp(-\frac{A}{T})$  were assumed. An expression for the cooling rate as a function of  $T_0$  and  $X_g$  was found for the partitioning of Zr between ilmenite and spinel.

$$\log a = \log \frac{D_o}{AX_g^2} + 2 \log T_o - 0.434 \frac{A}{T_o} - 0.868 \frac{T_o}{A} \quad (\text{II-31})$$

### 3. Elimination of Bubbles

The elimination of bubble can be used to estimate the rate of cooling of breccias and glasses. The processes by which gas bubbles are removed from silicate melts are relatively slow; and in commercial practice, the rate at which molten glass of high quality can be withdrawn from the tank is often limited by this process. In the case of clastic lunar (and terrestrial) rocks produced by impact events, it remains to be demonstrated whether the time-at-temperature is sufficient for the removal of substantially all bubbles.

The process by which gas bubbles are eliminated from glass melts is termed fining. In industry the batch from which glasses are made usually contain carbonates of sodium and calcium. These decompose upon heating to form CO<sub>2</sub> bubbles. Even when glass is produced by adding only cullet to bubble-free melts, bubbles are formed (45) due to gases absorbed on the surface of the batch particles and entrained air.

#### a. Experimental Results.

The mechanism of fining and the effects of fining agents have long been a subject of discussion among glassmakers. Many fining agents have been used effectively including As<sub>2</sub>O<sub>3</sub>, Sb<sub>2</sub>O<sub>3</sub>, CaF<sub>2</sub>, Na<sub>2</sub>SO<sub>4</sub>, NaCl, and NaNO<sub>3</sub> (45, 47). Of the two most intensively studied fining agents, the use of As<sub>2</sub>O<sub>3</sub> goes back to the middle ages when it was referred to as "glassmaker's soap." (48) The importance of Na<sub>2</sub>SO<sub>4</sub> was recognized as

early as 1866 (49).

It was originally believed that fining agents volatilize and form large bubbles which rise to the surface, sweeping out the smaller bubbles. Turner and his associates (50) showed that most of the arsenic added is retained and is found in the melt in the oxidized state. It was then hypothesized that at high temperatures, oxygen is evolved from the melt, leading to the growth of the bubbles and their rise to the surface. Greene and his colleagues (51-53) measured the size of a bubble as a function of time by rotating the sample to maintain the bubble at a fixed position. Oxygen bubbles were found to dissolve easily in melts refined with arsenic in the temperature range 1000-1300 C, with the dissolution rate increasing with increasing temperature. Boffe et al. (54) reported that CO<sub>2</sub> bubbles also shrink rapidly.

Cable et al. (54) found that at 1400 C, when arsenic is added to the batch, the composition of the gas in a bubble changes from CO<sub>2</sub> to O<sub>2</sub>. Cable and Haroon (52) found that at 1200 C, with or without arsenic the composition of the gas changes from CO<sub>2</sub> to O<sub>2</sub>, and that the addition of arsenic increased the rate of this reaction. The most rapid change of gas composition is observed with the addition of arsenic that produces the fastest refining. Furthermore, the rate of decrease of the carbon dioxide concentration was more than ten times greater than the rate of increase of oxygen concentration in the bubbles, despite the fact that the diffusivity and solubility of CO<sub>2</sub> in soda-lime-silica glass are smaller than those of O<sub>2</sub> (56). It was concluded that the most important function

of a refining agent is to permit the melt to absorb  $\text{CO}_2$ . Considering the small volume of gas involved, Cable suggested this occurred by increasing the rate of reaction with little or no change in the equilibrium solubility. There is no evidence to indicate that the presence of arsenic in the melt increases the solubility of  $\text{CO}_2$ . It does, however, increase the  $\text{O}_2$  solubility at melting temperatures (57). There is also some evidence that at high temperature,  $\text{As}_2\text{O}_5$  dissociates into  $\text{As}_2\text{O}_3$  and  $\text{O}_2$  (58). If this dissociation occurs in glass, the transport of this oxygen to the bubbles would cause their growth. It is found, however, that  $\text{As}^{+5}$  is the predominant species in glass under ambient conditions (58, 59). The addition of oxidizing agents such as  $\text{KNO}_3$  or  $\text{NaNO}_3$  diminishes the loss of arsenic by vaporization (59) in accord with the suggestion that  $\text{As}^{+5}$  is more stable in glass at melting temperatures than  $\text{As}^{+3}$ .

Konijnendijk and Buster (60) recently showed that the  $\text{As}^{+5}/\text{As}^{+3}$  ratio of  $30\text{K}_2\text{O}\cdot 70\text{SiO}_2$  glasses containing about 1 mole percent  $\text{As}_2\text{O}_3$  is approximately 12 and does not change significantly over the temperature range between 1000 and 1600 C. In soda-lime-silica glasses there was also no significant decrease in the amount of  $\text{As}^{+5}$  on increasing the melt temperature from 1250 to 1400 C (59).

Some contradictory evidence has been presented by Nemeč (61), who showed that above 1400 C, the bubbles in a soda-lime-silica melt grew rather than shrank when fining agents were added to the batch. If no fining agents were added, there were no changes in bubble size. During cooling, the bubbles ceased to grow and began to shrink at a temperature between 1370 and 1400 C. In interpreting these results, it was assumed

that  $\text{CO}_2$  is inert. This does not agree with the results of Cable who showed that the change in gas composition in the bubble involves more than simply the diffusion of  $\text{O}_2$  into the bubble with a concomitant dilution of the  $\text{CO}_2$ . Rather, the evidence indicates that the  $\text{CO}_2$  dissolves in the melt. The evidence presented thus far, indicates that arsenic aids in fining by increasing the rate of  $\text{O}_2$  dissolution over the whole temperature range.

A second and even more widely used fining agent is  $\text{Na}_2\text{SO}_4$  (saltcake). Lyle (62) showed that the effectiveness of sulfates in decreasing the fining time (the minimum time to produce a bubble-free melt after the addition of batch to a previously bubble-free melt) depends strongly on the glass composition. With a constant  $\text{SO}_3$  addition of 0.3%, the  $\text{Na}_2\text{O}-\text{CaO}-\text{SiO}_2$  phase diagram was divided into two regions of relatively constant fining times. The boundary between the regions was a straight line,  $(\% \text{SiO}_2) - 2.2(\% \text{Na}_2\text{O}) = 44.3$ . A sulfate content of 0.3%  $\text{SO}_3$  was found to produce good fining for the high silica-low alkali glasses, while glasses containing less  $\text{SiO}_2$  had shorter fining times with only 0.1%  $\text{SO}_3$ .

Cable (63) studied two melt compositions predicted to have quite different fining characteristics but similar viscosities and batch-free times. The two glasses were designated Bad ( $16\text{Na}_2\text{O}, 12\text{CaO}, 72\text{SiO}_2$ ) and Good ( $13\text{Na}_2\text{O}, 13\text{CaO}, 74\text{SiO}_2$ ) according to Lyle's predictions. It was reported necessary to add 0.46%  $\text{SO}_3$  to the batch to obtain a glass containing 0.3%  $\text{SO}_3$ , but only 0.395%  $\text{SO}_3$  to the batch to obtain a glass containing 0.35%  $\text{SO}_3$ .

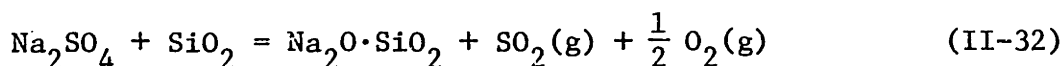


For both glasses at 1475 C, bubbles in the size range 0.20-0.40 mm. disappeared at about the rate predicted for removal by rise to the surface, and smaller bubbles disappeared much faster than this mechanism would predict. The "Bad" glass contained more bubbles than "Good" glass at the batch-free time, and it fined more slowly--in agreement with Lyle's predictions. Without sulfur at 1475 C, the "Good" glass refined more slowly than the "Bad". The addition of 0.30%  $\text{SO}_3$  increased the fining rate of the "Good" glass significantly, but not that of the "Bad". Further increases to 0.35 and 0.40%  $\text{SO}_3$  improved the fining behavior of the "Bad" glass.

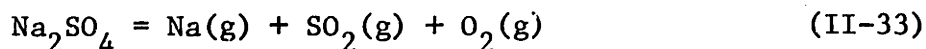
Using additional fining agents it was also found that the best results could be obtained by reducing the "Bad" glass (adding  $\text{As}_2\text{O}_3$ ) and by oxidizing the "Good" glass (adding  $\text{Na}_2\text{O}_2$ ).

It was suggested that the grouping (à la Lyle) of compositions into good and bad fining behavior at 1475 C represents a condition of constant  $\text{SO}_3$  solubility, and it was indicated that the mechanism of sulfate fining cannot be elucidated from available information. It is clear, however, that dissolution of gas bubbles in the melt is important and that the gas in the bubbles is predominantly  $\text{SO}_2$  (64). Greene and Platts (65) measured the size of  $\text{SO}_2$ ,  $\text{O}_2$  and  $\text{SO}_2+\text{O}_2$  bubbles in soda-lime-silica melts with and without fining agents. The rate of absorption of both  $\text{O}_2$  and  $\text{SO}_2$  increased as the temperature was increased from 1090 C to 1235 C. It was found that  $\text{Na}_2\text{SO}_4$  alone has no effect on the shrinkage of  $\text{O}_2$  or  $\text{SO}_2$  bubbles. The shrinking of an  $\text{SO}_2$  bubble in a glass with  $\text{NaNO}_3$  and  $\text{As}_2\text{O}_3$  was very

rapid but the addition of  $\text{Na}_2\text{SO}_4$  to the batch decreased the rate of absorption of  $\text{SO}_2$ . However, glass containing  $\text{Na}_2\text{SO}_4$ ,  $\text{NaNO}_3$  and  $\text{As}_2\text{O}_3$  absorbed  $\text{O}_2$  faster than a glass containing only  $\text{NaNO}_3$  and  $\text{As}_2\text{O}_3$ . The size of the bubbles was found to decrease as the square root of time, suggesting that the rate-limiting step is diffusion. The mechanism of  $\text{SO}_2$  solution was suggested to involve oxidation by  $\text{As}_2\text{O}_5$  to  $\text{SO}_3$  which is readily soluble in the glass. Conroy and coworkers (66, 67) examined the melting and fining behavior of soda-lime-silica glasses with and without the addition of sulfates. Under a hot stage microscope they observed that without sulfate, bubbles which formed earlier in the melting process and unmelted batch showed little or no movement. When sulfate is added, bubble formation and movement is rapid and solid particles "literally scoot over the surface of the melt." It was suggested that at low temperatures (above about 1050 C) sulfate acts as a surfactant, collecting at solid-melt and bubble-melt interfaces. It promotes rapid dissolution of the batch and the rise of bubbles to the surface. Above about 1100 C, appreciable reaction of the sulfate with the melt takes place to form sodium metasilicate.

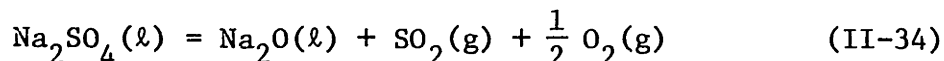


$\text{Na}_2\text{SO}_4$  and  $\text{Na}_2\text{O} \cdot \text{SiO}_2$  are completely visible but  $\text{Na}_2\text{SO}_4$  is essentially insoluble in more siliceous melts (68). Above about 1315 C, it was suggested that the sulfate decomposes according to the reaction



As decomposition proceeds the reaction products, particularly the highly soluble sodium and oxygen, pass easily into the melt, disrupting the liquid  $\text{Na}_2\text{SO}_4$ -melt interfacial forces and creating a convective motion at the interface. Above about 1450 C the partial pressure of the reaction products reaches one atmosphere and new bubbles are formed. It was suggested that these bubbles serve in the homogenization of the melt as they rise through the melt, growing when they enter a region of high  $\text{Na}_2\text{O}$  concentration and shrinking when they enter a region of high  $\text{SiO}_2$  concentration. When the glass is cooled,  $\text{Na}_2\text{SO}_4$  condenses on the surface of the bubble and the bubbles collapse.  $\text{Na}_2\text{SO}_4$  as well as sulfur have been found on the surface of bubbles (69).

Holmquist (68, 70) studied the thermodynamics of  $\text{Na}_2\text{SO}_4$  in sodium silicate melts. He suggested that  $\text{Na}_2\text{SO}_4$  decomposes according to the following reaction:



He suggested that the gas is dissolved in the melt by reacting with free oxygen ions,  $\text{O}^{2-}$ , to form  $\text{SO}_4^{2-}$ . This agrees with Poole's (71) results which show the importance of the partial pressures of  $\text{SO}_2$  and  $\text{O}_2$ . He suggested that the most important effect of  $\text{Na}_2\text{SO}_4$  was not its effect as a fining agent but its ability to promote melting of sand grains and to decrease the batch-free time. It was necessary to supply oxygen to the melt so the  $\text{SO}_2$  would be oxidized to  $\text{SO}_3$  which can be dissolved in the melt. It was found that a deficiency of  $\text{O}_2$  as by adding a reducing agent C would result in bubbles containing  $\text{SO}_2$  and  $\text{CO}_2$ . Too much  $\text{O}_2$  would

result in bubbles containing  $O_2$ .

Kenworthy (49) suggested that  $SO_3$  is formed within the bubble. Near the interface the  $SO_3$  concentration was suggested to be high, the  $Na_2O$  concentration be low, and the system may be represented by Eqn. II-32. If the  $Na_2O$  concentration is very small, in order to restore the equilibrium conditions, more gas is produced, and the pressure is increased until boiling occurs. The interface is thus disrupted and the rate of mass transfer is increased. He suggests that the mechanism of sulfate fining is the disruption of the bubble-melt interface and the subsequent increase in the rate of transfer of the gases in the bubble into the melt.

#### b. Mathematical Models

Several models have been proposed to describe the dissolution of gas-bubbles in molten glass. Greene and Gaffney (51) observed that the radius of a bubble decreases with the square root of time, and suggested that dissolution is a diffusion-controlled process.

Doremus (72) presented a model which assumed: (1) diffusion of the solute in the solution is the only process which affects the size of the bubble; (2) the concentration of solute in the sphere ( $C_s$ ), at the interface ( $C_i$ ) and in the bulk ( $C_\infty$ ) are constant; and (3) the diffusion coefficient is not a function of concentration. He suggested that a plausible expression for the bubble size as a function of time is

$$R_o^2 - R^2 = 2D\beta t \left( 1 + \frac{2R_o}{\sqrt{\pi D t}} \right) \quad (II-35)$$

where  $R_0$  is the initial radius and  $\beta = (C_i - C_\infty)/(C_s - C_i)$ . This solution provided good agreement with the data of Greene and Kitano, at least for the early stages of dissolution; and it was shown that the dilution of oxygen by another gas such as  $N_2$  could not account for the deviation at longer times. The deviation was suggested as caused by the finite size of the specimen, with oxygen diffusing into the melt from the surroundings, causing an increase in the bulk concentration.

Cable (56) recognized that the pressure within a bubble is not constant but increases as the bubble shrinks. He assumed that Henry's law is obeyed at the gas-melt interface, increasing the gas concentration at the interface as the bubble dissolves.

Readey and Cooper (73) numerically solved the diffusion equation for a stationary bubble in a melt, taking into account the moving boundary. They also included the effect of the change in volume of the glass caused by the transfer of material across the interface. This last effect is found to be negligible for a gas dissolving in molten glass. Cable (74) also considered the moving boundary problem for a stationary bubble. Cable and Evans (75) assumed that the interface concentration was constant, as was the concentration within the bubble, and that initial concentration at the interface was a step function. The effect of the radial flow was found to make a sphere dissolve more slowly than predicted by models such as that of Doremus, since as the boundary moves inward, the size of the diffusion layer increases.

For growing bubbles, Cable and Evans found that errors may be

introduced unless the dissolution rate is small and the concentration field around the sphere expands faster than the sphere itself.

Data and Vrentas (76) advanced a perturbation solution to describe the dissolution or growth of a bubble. The first term of their solution is the same as the solution of Doremus. They also advanced a finite difference solution to the problem of the growth or dissolution of a bubble. This solution was compared with the finite difference solution of Cable and Evans. Both of these models took account of the effects of the moving boundary, and both assumed a constant concentration of gas at the bubble-melt interface.

All the models described thus far apply to a stationary bubble. Except for exceptional melting conditions and very small bubbles, however, a gas bubble in a glass tank is not stationary. Further, recent developments at Owens-Illinois concerned with centrifugation fining (77), together with interest in melting glasses under microgravity conditions, have directed attention to the effects of motion on the growth and dissolution of bubbles.

Greene and Lee (53) showed that when a bubble is allowed to rise through the melt, the rate of dissolution is an order of magnitude faster than that for a stationary bubble. As the bubble rises, it moves away from its diffusion field. Levich (78) obtained a solution for the diffusional flux to a moving drop. The concentration distribution in the boundary layer was described by

$$V_r \frac{\partial c}{\partial r} + \frac{V_\theta}{r} \frac{\partial c}{\partial \theta} = D \frac{\partial^2 c}{\partial r^2} \quad (\text{II-36})$$

Here  $V_r$  and  $V_\theta$  are the radial and tangential components of the velocity of the fluid as it moves relative to the bubble. This expression does not take into account terms which relate concentration with respect to radius, the tangential components of the concentration gradient, or the effect of the moving boundary. Levich assumed that the concentration at the interface is constant. The bubble is found to rise faster than the Stokes law velocity predicted for a solid sphere. Due to the mobility of the interface, the tangential component of the velocity is now zero. This leads to a decrease in the energy dissipated in the liquid, so with the same driving force (gravity), the velocity of a fluid within a fluid should be greater than the velocity of a solid sphere. The presence of surfactants would make the bubble behave more like a solid and would decrease its velocity.

The diffusional flux to or from the surface of a bubble of radius  $a$  is

$$j = D \left( \frac{\partial c}{\partial r} \right)_{r=a} = \frac{D(C_\infty - C_0)}{\delta} \quad (\text{II-37})$$

where  $\delta$  is the boundary layer thickness

$$\delta = \sqrt{\frac{\pi}{3}} \left( \frac{aD}{V_0} \right)^{1/2} \sqrt{\frac{2+\cos \theta}{(1+\cos \theta)^2}} \quad (\text{II-38})$$

and  $V_0$  is the velocity of the bubble

$$V_0 = \frac{\rho g a^2}{3\eta} \quad (\text{II-39})$$

Here  $\rho$  is the density of the melt,  $\eta$  is its viscosity, and  $g$  is the gravitational constant. Levich assumed that the diffusion layer is small compared with the size of bubble. Hence Eqns. (II-37) and (II-38) would not hold for small bubbles, but since the velocity is small, the solutions for a stationary sphere would be sufficient.

Using the results of Levich, Nemeč (61) derived an expression for the size of a bubble as a function of time, assuming that the bubble behaved as a solid sphere:

$$a = a_0 + 0.38(C_\infty - C_i) \frac{D^{2/3} g^{1/3} \rho^{1/3}}{\eta^{1/3} \rho'} t = a_0 + kt \quad (\text{II-39})$$

Here  $\rho'$  is the density of the diffusing gas. This relation indicates that the bubble size changes linearly with time, in accord with Nemeč's experimental results but at variance with the experimental data of others and with other theoretical models. A linear change in bubble size with time indicates that the bubble moves out of its diffusion field so rapidly that the scale of the diffusion field is constant.



### III. PLAN OF WORK

In the work that follows, several aspects of glass formation are investigated, including crystallization kinetics, thermal history, and fining. Special emphasis is given to the determination of the thermal history of materials by modelling the conditions of formation and comparing aspects of the microstructure predicted by model to those observed in lunar, terrestrial and laboratory samples. Each model is presented and discussed in turn.

First, the effect of heterogeneous nucleation on the minimum cooling rate for glass formation is investigated. The efficiency of various types of nucleating sites is determined.

Second, a simple model for the prediction of the glass forming ability of many materials is presented. This is derived from the more complex model of transformation kinetics proposed by Uhlmann (8) and several time-temperature-transformation curves calculated from his model.

Third, the model of Hopper et al. (25), which describes crystallization statistics in glass-forming systems, is examined and expanded to include the reheating of samples after initial cooling. The crystallization temperature is determined as a function of cooling rate, heating rate, and nucleation barrier, and the predictions of the model are compared with DSC experiments on several materials.

Fourth, heat flow calculations are presented which model the two-stage cooling process proposed by Simonds (30) to describe the thermal

histories of certain lunar and terrestrial impact sites. The extent of clast digestion in the first stage of cooling by heat flow to cold clasts is estimated. For the second stage cooling by heat flow to the surroundings, several sets of boundary conditions are used. The results are used to compare the effects of boundary conditions on the overall cooling of impact melt sheets.

Fifth, nonisothermal diffusion in the solid state is modelled to determine the thermal history of samples exhibiting incomplete solute redistribution or zoning. The results are compared with the model proposed by Taylor et al. (31).

Sixth, the fining process is examined. Three models are proposed to describe the growth or dissolution of a moving bubble. The effects of temperature, relative solubility and gravity are discussed.

#### IV. NUCLEATING HETEROGENEITIES AND GLASS FORMATION

##### A. The Model

In evaluating the effects of heterogeneous nucleation on glass formation, we shall utilize the expression for the volume fraction  $X$ , crystallized in a time  $t$ , provided by the normal theory of transformation kinetics. When the nucleation rate  $I_v$  and the crystal growth rate  $u$  are independent of time, the volume fraction crystallized is

$$X \approx \frac{1}{3} \pi I_v u^3 t^4 \quad (\text{IV-1})$$

for small values of  $X$ . The assumption of a time-independent nucleation frequency should be good in nearly all cases of homogeneous nucleation and in many cases of heterogeneous nucleation. The assumption of a time-independent growth rate should be good for crystallization without a change of composition, as well as for many cases involving large compositional changes on crystallization.

In using Eqn. (IV-1) to describe glass formation, measured growth rates are used whenever possible. To determine the growth rate over the whole temperature range of interest, the computer was used to determine a parabolic least squares fit of the growth rate vs. temperature in order to interpolate and extrapolate the data for each material. A comparison of the measured and calculated growth rates is shown in figure IV-1. Where such data are unavailable, the growth rate was calculated from the relation

$$u = f v a_o [1 - \exp(-\Delta H_{fm} \Delta T / RT T_E)] \quad (\text{IV-2})$$

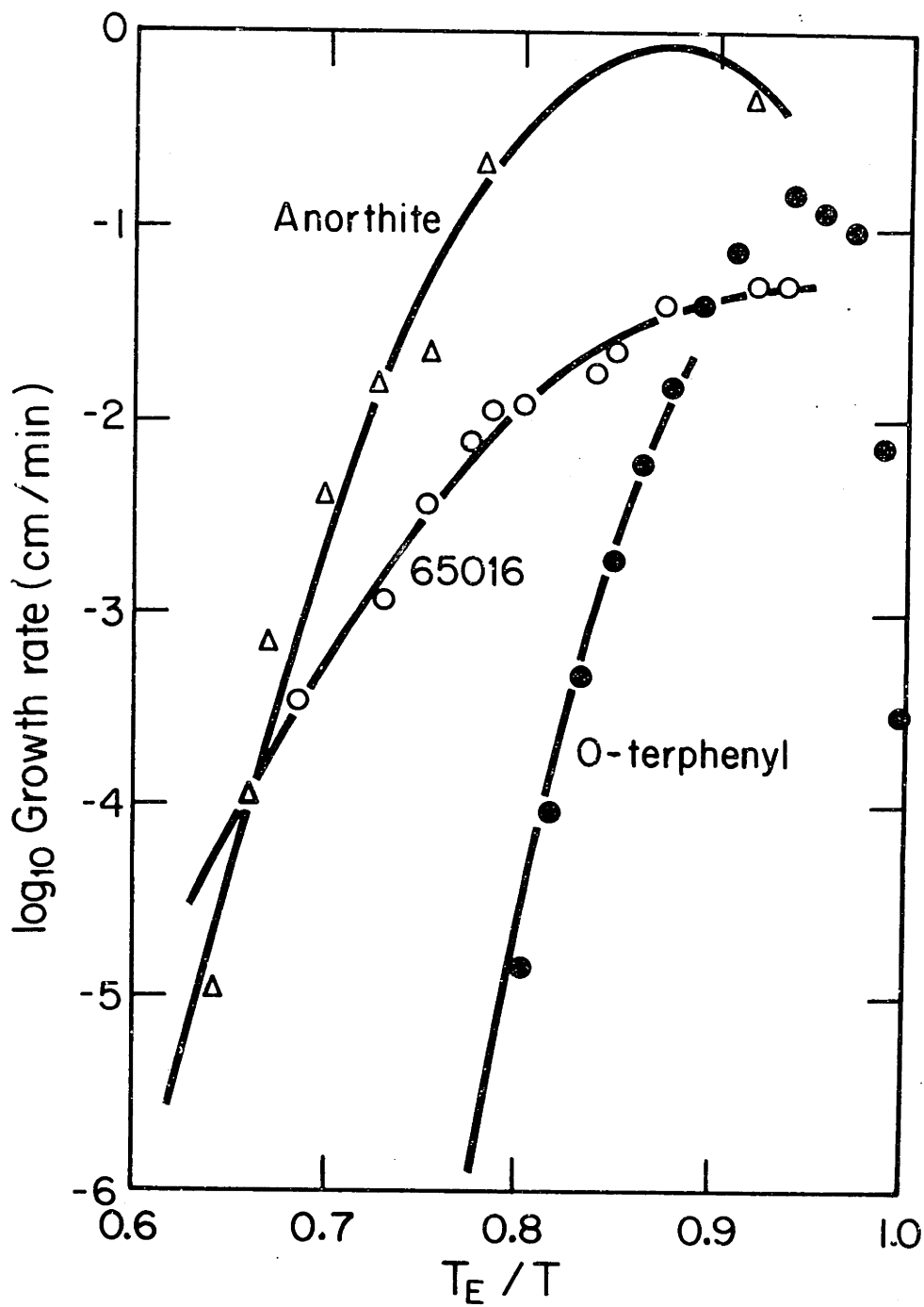


Figure IV-1 - Measured and calculated growth rate vs.  $T/T_E$  assuming parabolic least squares fit for lunar composition 65016, anorthite, and o-terphenyl.

where  $\nu$  is the frequency of atom transport at the crystal-liquid interface,  $a_0$  is a molecular diameter,  $\Delta H_{fM}$  is the molar heat of fusion,  $\Delta T$  is the undercooling,  $R$  is the gas constant, and  $f$  is the fraction of preferred growth sites on the interface. According to the Stokes-Einstein approximation, the frequency factor  $\nu$  is

$$\nu = kT/3\pi a_0^3 \eta \quad (IV-3)$$

where  $\eta$  is the viscosity. Again, a parabolic least squares fit of the available viscosity data was used to predict the viscosity vs. temperature relation over the temperature range of interest. A comparison of the measure and calculated viscosities is shown in Figure IV-2.

When only homogeneous nucleation of crystals is considered, the nucleation frequency can be expressed as

$$I_v^{HO} \approx N_v^0 \nu \exp(-Q) \quad (IV-4)$$

where  $N_v^0$  is the number of single molecules per unit volume and  $Q$  is given by

$$Q = .02048B T_E^5/T^3 \Delta T^2 \quad (IV-5)$$

This is based on the standard treatment of homogeneous nucleation with a nucleation barrier of  $B k T$  at  $\Delta T/T_E = 0.2$ . In most cases a nucleation barrier of  $60 kT$  is assumed.

The critical cooling rate can be approximated from TTT diagrams by

$$\left(\frac{dT}{dt}\right)_c \approx \frac{\Delta T_N}{\tau_N} \quad (IV-6)$$

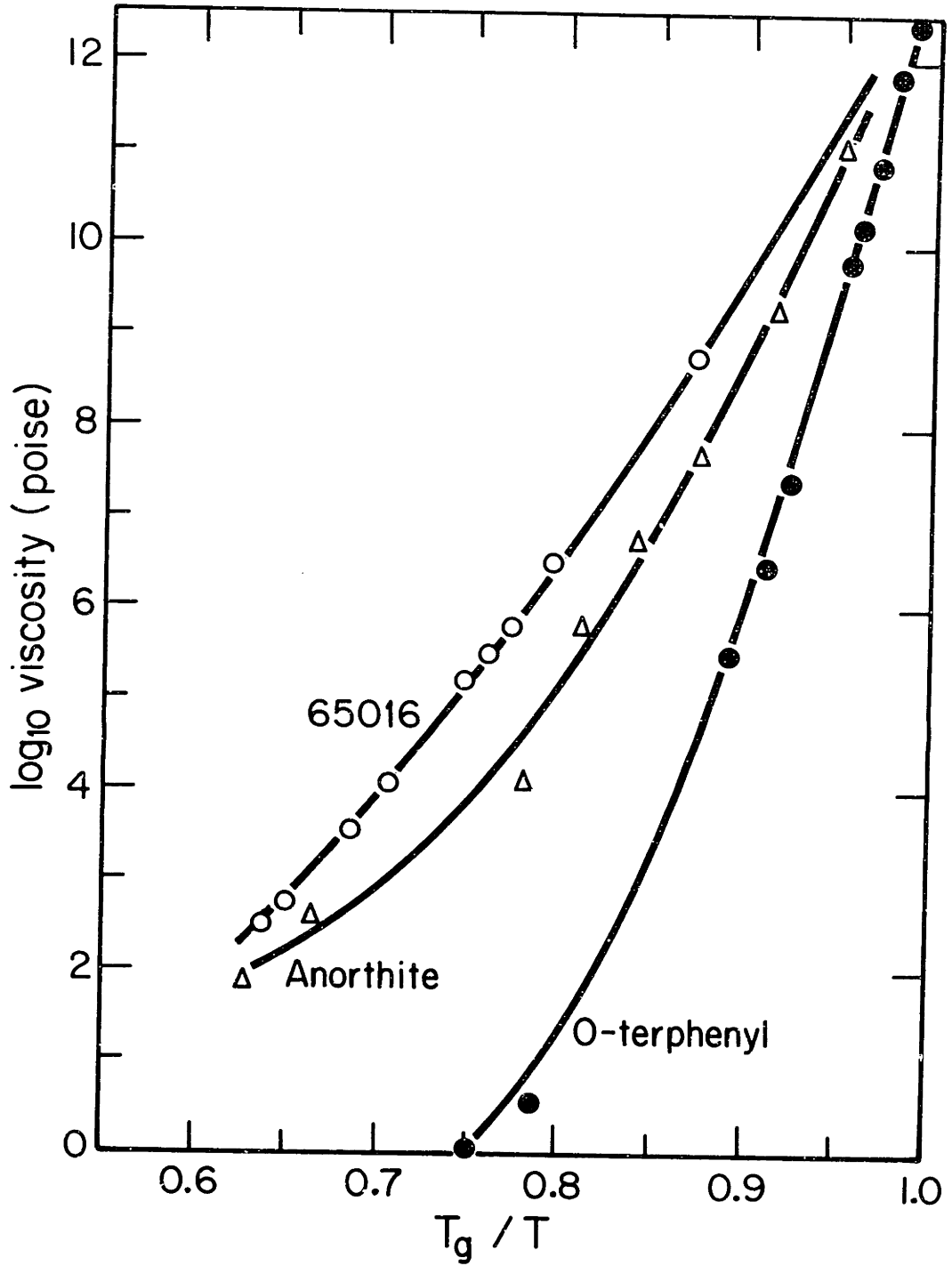


Figure IV-2 - Measured and calculated viscosity vs.  $T_g/T$  relation assuming parabolic least squares fit for lunar composition 65016, anorthite, and o-terphenyl.

where  $\Delta T_N = T_E - T_N$ ,  $T_N$  is the temperature at the nose of the TTT curve;  $T_E$  is the liquidus, and  $\tau_N$  is the time at the nose.

Equation (IV-6) as calculated from isothermal TTT diagrams overestimate the difficulty of forming a glass because the method of construction assumes that the kinetics during cooling from the liquidus to the temperature of the nose of the TTT diagram are as rapid as at the temperature of the nose. Uhlmann and Klein (79) and Onorato and Uhlmann (80) followed the procedure of Grange and Keifer (19) in the construction of continuous cooling (CT) curves which were originally developed for use in steelmaking. In this approach, the fractional changes in the degree of crystallinity was determined for times  $dt$  in the temperature range  $dT$ . The critical assumption is that on cooling through a limited temperature range, for example the range from  $T_1$  at time  $t_1$  to  $T_2$  at  $t_2$ , the amount of crystallization is substantially equal to the amount indicated by the isothermal TTT curve at the mean temperature  $(T_1 + T_2)/2$  after a time interval  $t_2 - t_1$ .

The transition from TTT curves to CT curves is illustrated in Fig. IV-3. For a cooling rate  $R_1$ , the volume fraction  $X_1$  is not reached at temperature  $T_0$ , or even at the temperature  $T_1$ . Only at  $T_2$  is  $X_1$  reached: the isothermal point corresponding to A on the CT curve is A' at  $[(T_0 + T_2)/2, t_2 - t_0]$ . For a slower cooling rate  $R_2$ , the volume fraction  $X_1$  will be reached at point B (temperature  $T_3$ ); while for a faster cooling rate  $R_3$ ,  $X_1$  will be reached at point C (temperature  $T_4$ ). The locus of points such as A, B, C defines the CT curve for a fraction crystallized

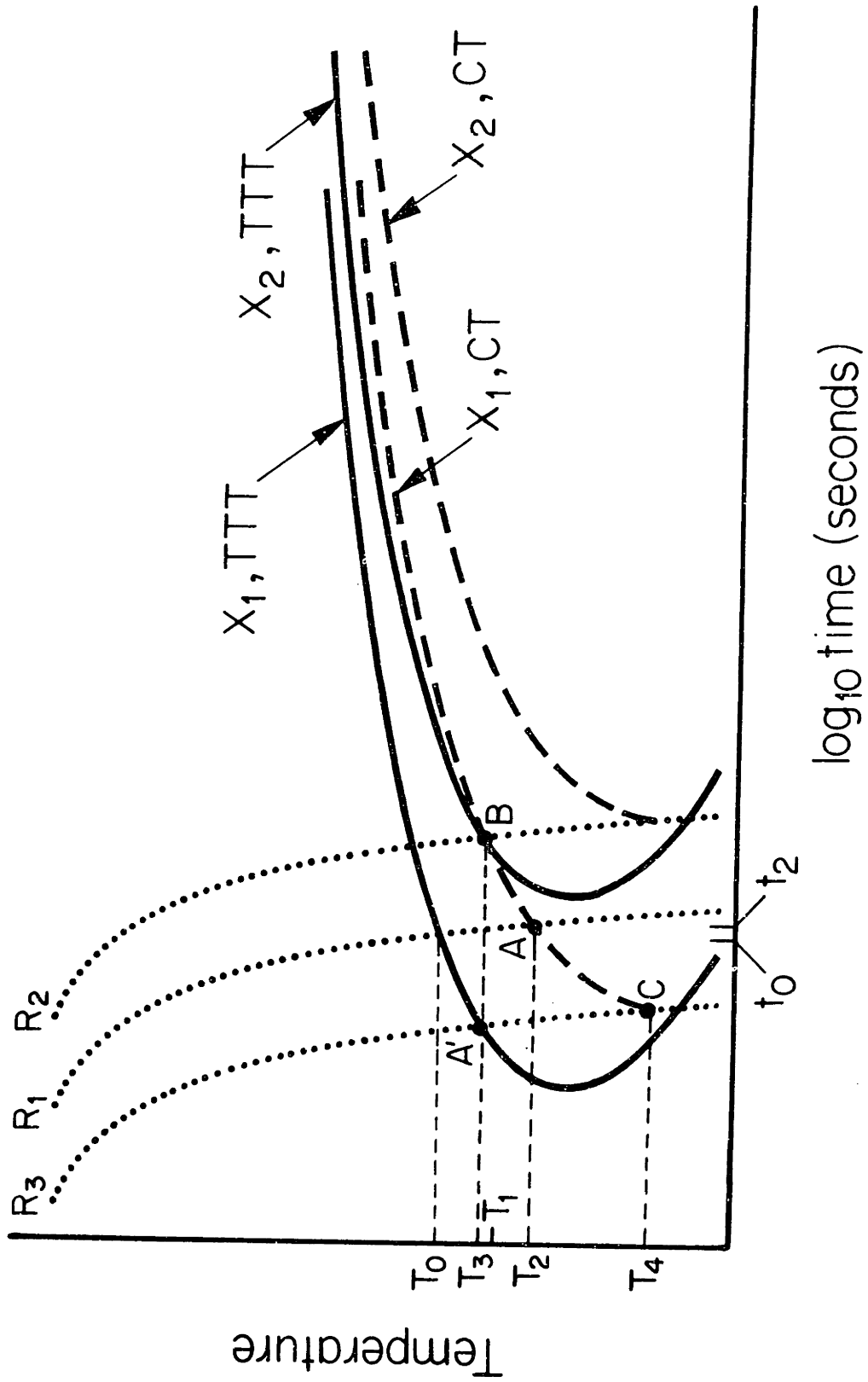


Figure IV-3 - Schematic diagram illustrating construction of continuous cooling (CT) from isothermal time-temperature transformation curves.



of  $X_1$ . When this procedure is repeated for a different fraction crystallized  $X_2$ , results such as those shown in Fig. IV-3 are obtained.

In terms of that figure, cooling rates between  $R_3$  and  $R_2$  will result in fractions crystallized between  $X_1$  and  $X_2$ ; and cooling rates greater than  $R_3$  are required to avoid a fraction crystallized of  $X_1$ . As seen in Fig. IV-3, the curves describing crystallization during continuous cooling indicate that a given degree of crystallization is developed at lower temperatures and longer times than a cursory examination of the isothermal TTT curves or use of Eqn. (IV-6) would suggest. This technique has been successfully applied to the determination of the thermal histories of lunar samples (32, 79, 80).

In assessing the effect of nucleating heterogeneities on glass formation, it is convenient to use the familiar spherical cap model of the heterogeneous nucleus. In terms of this model, the nucleation frequency for a heterogeneity characterized by a contact angle  $\theta$  can be expressed as

$$I_v^{HE} = A_v N_s^0 v \exp[-Qf(\theta)] \quad (IV-7)$$

where  $A_v$  is the area of nucleating substrate per unit volume of the melt,  $N_s^0$  is the number of molecules per unit area of substrate, and  $f(\theta)$  is given by

$$f(\theta) = [(2+\cos\theta)(1-\cos\theta)^2]/4 \quad (IV-8)$$

In accord with previous nucleation experiments, the value of  $2 \times 10^7$  heterogeneities/cm<sup>3</sup> was used together with an assumed area of  $1.5 \times 10^{-10}$  cm<sup>2</sup>

per particle (corresponding to particles  $500 \text{ \AA}$  in extent). With these values,  $A_v \approx 3 \times 10^{-3} \text{ cm}^{-1}$ ; and the rate of heterogeneous nucleation can be calculated from Eqn. (IV-7). The overall nucleation rate is the sum of the rates of homogeneous and heterogeneous nucleation:

$$I_v = I_v^{\text{HO}} + I_v^{\text{HE}} \quad (\text{IV-9})$$

The TTT and CT curves corresponding to a just-detectable degree of crystallinity ( $X = 10^{-6}$ ) have been constructed for the following materials:  $\text{SiO}_2$ ,  $\text{GeO}_2$ ,  $\text{Na}_2\text{O} \cdot 2\text{SiO}_2$ ,  $\text{CaO} \cdot \text{Al}_2\text{O}_3 \cdot 2\text{SiO}_2$ , o-terphenyl, salol,  $\text{H}_2\text{O}$ , a silver-like metal, and several lunar compositions. The lunar samples and their compositions are listed in Table IV-1. For  $\text{H}_2\text{O}$  and the metal, the growth rates were calculated using Eqn. (IV-2) with  $\Delta H_{\text{FM}}(\text{H}_2\text{O}) = 1430 \text{ cal/mole}$  and  $\Delta H_{\text{FM}}(\text{metal}) = 2700 \text{ cal/mole}$ . In all other cases, measured growth rates were used.

## B. Results

Typical results for the effects of nucleating heterogeneities on glass formation are shown by the TTT curves in Fig. IV-4 for  $\text{Na}_2\text{O} \cdot 2\text{SiO}_2$ . As seen there, heterogeneities characterized by modest contact angles ( $\theta < 100^\circ$ ) can have a pronounced effect on the time required to achieve a given degree of crystallinity--and hence on glass-forming ability--while heterogeneities characterized by large contact angles ( $\theta > 120^\circ$ ) have a negligible effect on glass-forming ability.

The corresponding CT curves for  $\text{Na}_2\text{O} \cdot 2\text{SiO}_2$  are shown in Fig. IV-5. From these curves, critical cooling rates are calculated according to

Table IV-1Lunar Compositions Investigated

(wt. %)

	<u>15418</u>	<u>60095</u>	<u>70019</u>	<u>65016</u>	<u>79155</u>
SiO <sub>2</sub>	45.0	46.4	41.3	44.2	34.1
TiO <sub>2</sub>			8.4	0.6	13.7
Al <sub>2</sub> O <sub>3</sub>	26.7	23.5	12.4	26.5	3.5
FeO	5.4	6.9	16.1	5.5	22.6
MgO	5.4	10.5	10.2	7.3	11.1
CaI	16.1	12.1	11.2	15.3	10.6
Na <sub>2</sub> O			0.3	0.4	0.2
K <sub>2</sub> O		0.8		0.1	

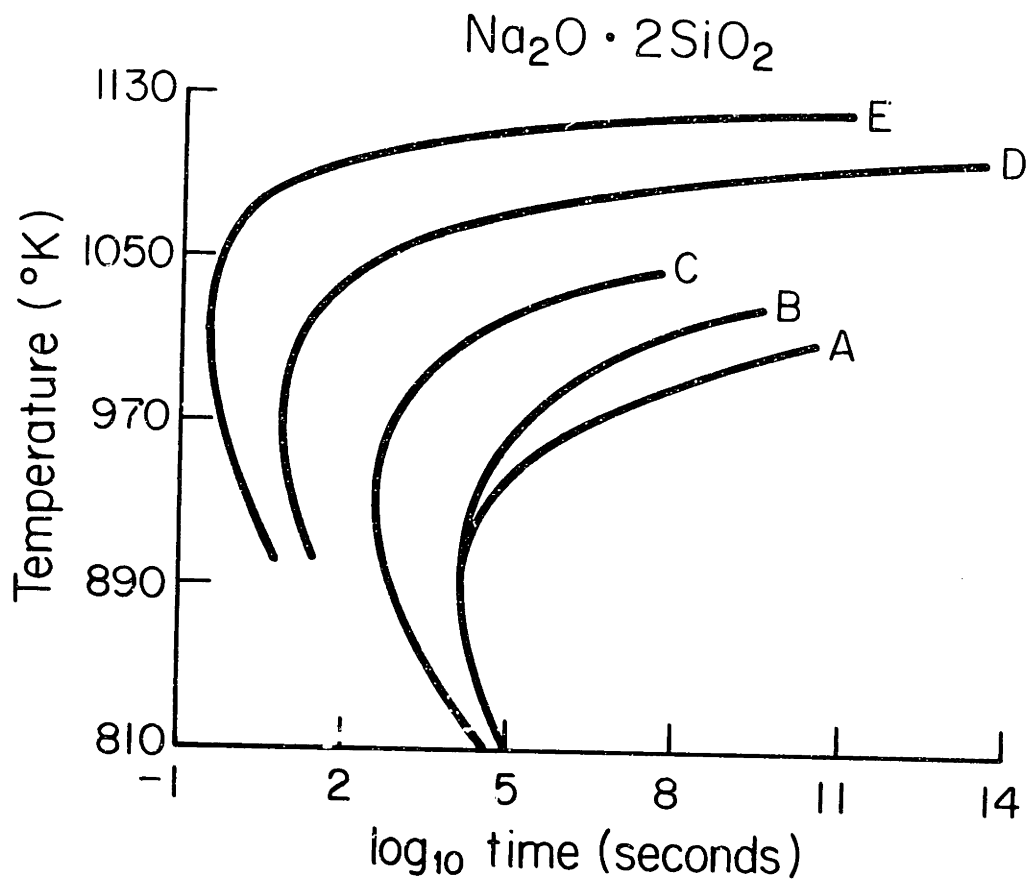


Figure IV-4 - The TTT curves for  $\text{Na}_2\text{O} \cdot 2\text{SiO}_2$  corresponding to a volume fraction crystallized of  $10^{-6}$ . Curve A, homogeneous nucleation only,  $\theta=160^\circ$ ,  $\theta=120^\circ$ ; curve B,  $\theta=100^\circ$ ; curve C,  $\theta=80^\circ$ ; curve D,  $\theta=60^\circ$ ; curve E,  $\theta=40^\circ$ .

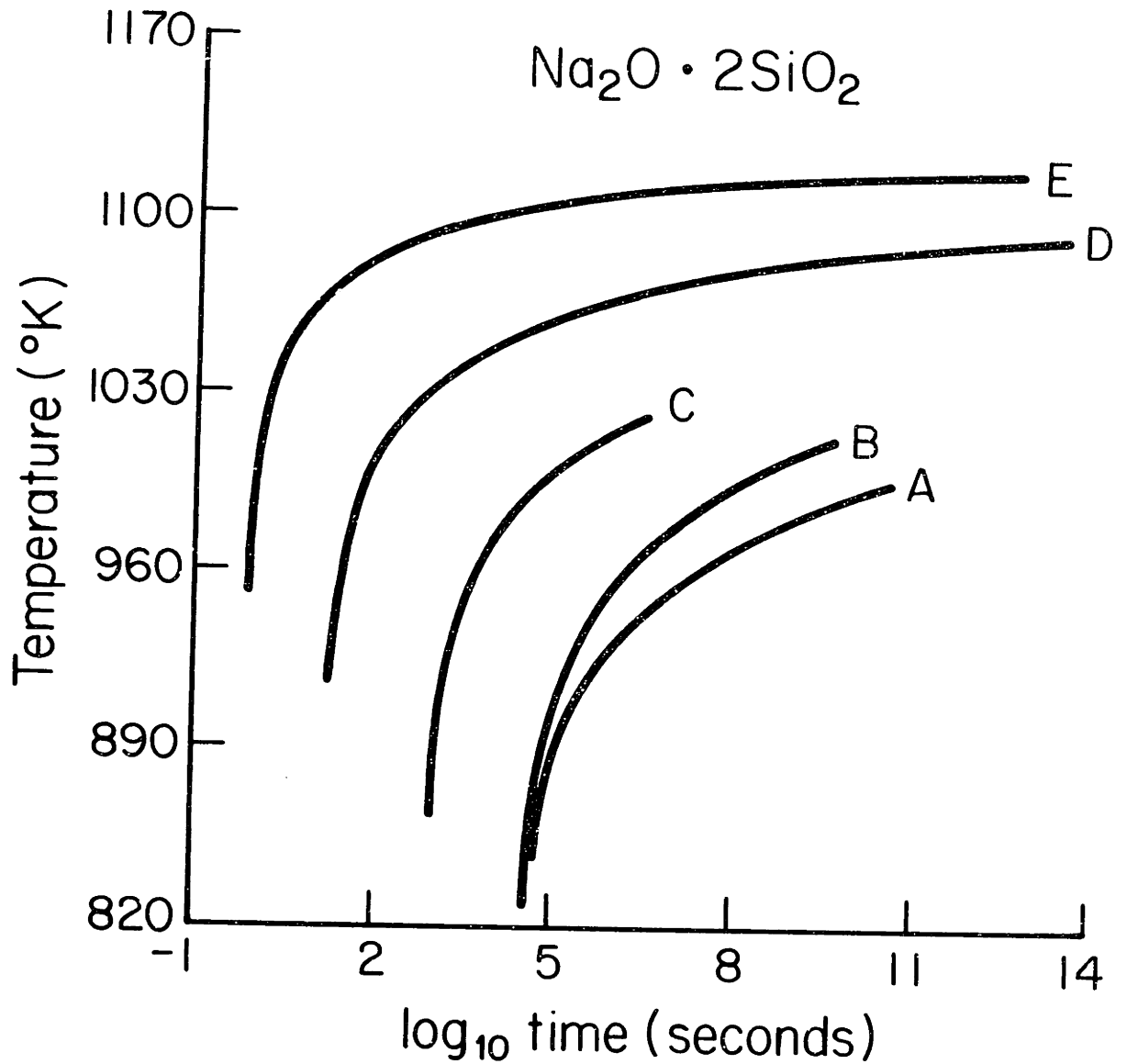


Figure IV-5 - The CT curves for  $\text{Na}_2\text{O} \cdot 2\text{SiO}_2$  corresponding to a volume fraction crystallized of  $10^{-6}$ . Curve A, homogeneous nucleation only,  $\theta=160^\circ$ ,  $\theta=120^\circ$ ; curve B,  $\theta=100^\circ$ ; curve C,  $\theta=80^\circ$ ; curve D,  $\theta=60^\circ$ ; curve E,  $\theta=40^\circ$ . Curves constructed from TTT curves following method showing in Fig. IV-3.

Eqn.(IV-6) where the subscript N refers to the nose of the CT curve rather than the TTT curve. The cooling rates required to allow a volume fraction crystallized of  $10^{-6}$  are about 300, 10, 0.3,  $8 \times 10^{-3}$  and  $6 \times 10^{-3}$  K sec<sup>-1</sup> are for samples containing heterogeneities with contact angles of 40°, 60°, 80°, 100°, and (120°, 160°, only homogeneous nucleation). As suggested above, the cooling rate required to make a glass of the sample with  $\theta=120^\circ$  heterogeneities is closely similar to that required for a. By comparison, the critical cooling rates calculated according to Eqn. (IV-6) from TTT diagrams represent an overestimate of the cooling rate necessary to form a glass, the cooling rates being about 400, 30, 0.6,  $2 \times 10^{-2}$  and  $6 \times 10^{-3}$  K sec<sup>-1</sup> for the  $\theta$  values cited above.

The results of similar calculations for a variety of materials, including oxides, metals, organics, and water--indicate that nucleating heterogeneities present in the indicated concentration with  $\theta$  values greater than about 100° quite generally have a negligible effect on glass-forming ability. The results are illustrated by the comparison in Table IV-2 between the critical cooling rates estimated assuming only homogeneous nucleation, and those estimated with the indicated density of heterogeneities all characterized by contact angles of 40, 60, 80, and 100°. The sources for the experimental data used in the calculations are given in Appendix A.

The effects on glass formation of changes in the barrier to nucleation are shown in Table IV-3, where critical cooling rates calculated from CT curves are compared for barriers to homogeneous nucleation at  $\Delta T/T_E = 0.2$

Table IV-2

Effect of Contact Angle of Heterogeneities ( $2 \times 10^7 \text{ cm}^{-3}$ )  
on Calculated Critical Cooling Rates for Glass Formation

Material	Homogeneous nucleation	$\theta=100^\circ$	$\theta=80^\circ$	$\theta=60^\circ$	$\theta=40^\circ$
	$\text{K s}^{-1}$	$\text{K s}^{-1}$	$\text{K s}^{-1}$	$\text{K s}^{-1}$	$\text{K s}^{-1}$
$\text{SiO}_2$	$9 \times 10^{-6}$	$10^{-5}$	$2 \times 10^{-4}$	$8 \times 10^{-3}$	$2 \times 10^{-1}$
$\text{GeO}_2$	$3 \times 10^{-3}$	$3 \times 10^{-3}$	$3 \times 10^{-2}$	1	20
$\text{Na}_2\text{O} \cdot 2\text{SiO}_2$	$6 \times 10^{-3}$	$8 \times 10^{-3}$	$3 \times 10^{-1}$	10	$3 \times 10^2$
$\text{CaO} \cdot \text{Al}_2\text{O}_3 \cdot 2\text{SiO}_2$	$3 \times 10^2$	$3 \times 10^2$	$5 \times 10^3$	$2 \times 10^5$	$2 \times 10^6$
lunar comp. 15418	60	60	$7 \times 10^2$	$2 \times 10^4$	$2 \times 10^5$
lunar comp. 60095	20	20	$3 \times 10^2$	$10^4$	$10^5$
lunar comp. 70019	$10^{-1}$	$10^{-1}$	6	$5 \times 10^2$	$2 \times 10^4$
lunar comp. 79155	7	2.5	80	$5 \times 10^3$	$1 \times 10^5$
lunar comp. 65016	30	32	$3 \times 10^2$	$1 \times 10^4$	$1 \times 10^5$
o-terphenyl	$1 \times 10^{-3}$	$4 \times 10^{-3}$	8	$2 \times 10^2$	$1 \times 10^4$
salol	$2 \times 10^{-2}$	$3 \times 10^{-2}$	1	$10^2$	$8 \times 10^3$
$\text{H}_2\text{O}$	$5 \times 10^5$	$5 \times 10^5$	$5 \times 10^6$	$10^8$	$10^9$
metal	$9 \times 10^8$	$9 \times 10^9$	$2 \times 10^9$	$10^{10}$	$5 \times 10^{10}$

Table IV-3

Effect of Nucleation Barrier on Calculated Cooling Rates  
for Glass Formation (Homogeneous Nucleation)

Material	$\Delta G^*=50 \text{ kT}$	$\Delta G^*=60 \text{ kT}$	$\Delta G^*=70 \text{ kT}$
	at $\Delta T/T_E=0.2$	at $\Delta T/T_E=0.2$	at $\Delta T/T_E=0.2$
	$\text{K s}^{-1}$	$\text{K s}^{-1}$	$\text{K s}^{-1}$
$\text{SiO}_2$	$7 \times 10^{-5}$	$9 \times 10^{-6}$	$10^{-6}$
$\text{GeO}_2$	$2 \times 10^{-2}$	$3 \times 10^{-3}$	$4 \times 10^{-4}$
$\text{Na}_2\text{O} \cdot 2\text{SiO}_2$	$6 \times 10^{-2}$	$6 \times 10^{-3}$	$9 \times 10^{-4}$
$\text{CaO} \cdot \text{Al}_2\text{O}_3 \cdot 2\text{SiO}_2$	$3 \times 10^3$	$3 \times 10^2$	40
lunar comp. 15418	$4 \times 10^2$	60	9
lunar comp. 60095	$10^2$	20	2
lunar comp. 70019	$9 \times 10^{-1}$	$10^{-1}$	$10^{-2}$
lunar comp. 79155	17	2.3	$3 \times 10^{-1}$
lunar comp. 65016	$2 \times 10^2$	$3 \times 10^1$	6
o-terphenyl	$2 \times 10^{-2}$	$1 \times 10^{-3}$	$8 \times 10^{-5}$
salol	$2 \times 10^{-1}$	$2 \times 10^{-2}$	$2 \times 10^{-3}$
$\text{H}_2\text{O}$	$4 \times 10^6$	$5 \times 10^5$	$10^5$
metal	$4 \times 10^9$	$9 \times 10^8$	$2 \times 10^8$



of 50, 60, and 70 kT. As seen there, these effects can also be substantial. When the calculated rates for various oxides, including a number of lunar compositions, are compared with experience in the laboratory, the difficulty of forming glasses is generally overestimated when it is assumed that  $\Delta G^* = 50 \text{ kT}$  at  $\Delta T/T_E = 0.2$ ; that is, the calculated cooling rates, even neglecting nucleating heterogeneities, are consistently higher than those required to form glasses in the laboratory. Reasonable agreement between calculated rates and laboratory experiments can be obtained by taking somewhat larger values for  $\Delta G^*$  (in the range 55-65 kT at  $\Delta T/T_E = 0.2$ ). Recent measurements of the nucleation frequency by Klein and Uhlmann (79) for the 70019 composition indicate a nucleation barrier of 55 kT at  $\Delta T/T_E = 0.2$ .

### C. Discussion and Conclusions

The analysis of glass formation in the preceding section is based on using the formal theory of transformation kinetics, together with an identification of  $10^{-6}$  as a just-detectable degree of crystallinity. In estimating the critical cooling rates required to form glasses of different materials, TTT curves are constructed from calculated nucleation rates, calculated or measured growth rates, and measured viscosities. Continuous cooling (CT) curves are then constructed from the TTT curves, and critical cooling rates are estimated directly from the CT curves. The critical cooling rates obtained in this way are more reliable than those obtained directly from TTT curves because the latter approach makes the implicit assumption that the crystallization kinetics over the whole cooling range

are as rapid as they are at the nose of the TTT curve. Relative comparisons of the glass-forming ability of different materials can, however, be made using either TTT or CT curves.

In evaluating the effects of nucleating heterogeneities on glass formation, use has been made of the spherical cap model of the heterogeneous nucleus, together with a density of heterogeneities inferred from many nucleation studies. The results presented above indicate that while all heterogeneities characterized by contact angles  $\theta < 180^\circ$  are properly described as nucleating heterogeneities, only those with  $\theta$  smaller than about  $100^\circ$  have significant effect on glass-forming ability, at least for concentrations of nucleation sites in the range of  $10^7 \text{ cm}^{-3}$  or less. Nucleating heterogeneities characterized by larger contact angles become effective only at large undercoolings where they have little effect on the overall crystallization kinetics.

The contact angle is a function of the interfacial surface energies ( $\gamma$ ) between the crystal nucleus (c), the substrate (s) and the liquid (l):

$$\gamma_{cl} \cos\theta = -\gamma_{sc} + \gamma_{sl} \quad (\text{IV-10})$$

Assuming that  $\gamma_{cl}$ , the interfacial energy between crystal nucleus and liquid is constant, effective nucleating substrates (those with small  $\theta$ 's) are those with  $\gamma_{sl}$  or low  $\gamma_{sc}$ . In assessing the effects of heterogeneous nuclei, we have used concentrations of such nuclei inferred from experiments on a variety of materials. It should be noted, however, that the assumed concentrations may represent overestimates of the actual

densities of nucleation sites in some cases; and smaller concentrations would be expected for liquids which serve as effective fluxes. Such liquids include the transition metals, many of which can be undercooled in bulk form by hundreds of degrees without crystallization; multicomponent oxide melts containing sizable concentrations of transition metal oxides; many materials which require very high temperatures for their initial melting; and many silicate compositions containing large concentrations of PbO. It is recognized that superheating a material well above its liquidus temperature is conducive to the elimination of heterogeneous nuclei.

The effects on glass-forming ability of changes in the surface energy barrier to homogeneous nucleation have also been explored. Changes in the corresponding free energy barrier over the range between 50 and 70 kT at a relative undercooling of 0.2 can change the critical cooling rate for glass formation by nearly two orders of magnitude. As shown above for  $\text{Na}_2\text{O}\cdot 2\text{SiO}_2$ , such changes are comparable with those which result from only homogeneous nucleation being operative to heterogeneities with contact angles of about  $70^\circ$  being present in concentrations of  $2 \times 10^7 \text{ cm}^{-3}$ . From this result, it may be inferred that the concentration of relatively potent nucleating heterogeneities has a more pronounced effect on glass formation than the magnitude of the surface energy barrier to nucleation (for both quantities considered in a reasonable range).

The results shown in Tables IV-2 and IV-3 for water and for the metal are subjected to considerable uncertainty. For both, the viscosity data had to be extrapolated over a wide range of temperature in carrying

out the calculations, and in the case of the metal, a high value was assumed for the glass transition temperature (which is unknown) to ensure consideration of the minimum conditions for glass formation. The results should simply be taken as indicating that it is unlikely, with or without heterogeneities, that a pure metal can be found as a glass from the melt.

The present analysis takes no direct account of the crystal size and number distributions of crystals within a melt. The method by which the CT curves are derived from the TTT curves does not allow for the continuation of the CT curve beyond its intersection with the TTT curve; nor does it take into account more complex thermal histories which include reheating. In cases where these factors are important, a more complete analysis of crystallization statistics (25) is required. This will be discussed in a later chapter.

## V. A SIMPLIFIED MODEL FOR GLASS FORMATION

### A. The Model

The determination of the critical cooling rate for glass formation has been determined for many materials using the formal theory of transformation kinetics. In order to apply this theory to a particular material, it is necessary to know the viscosity and the crystal growth rate over a wide range of temperature. It is also important to know the magnitude of the nucleation barrier in the material. Unfortunately, such information is not available for many materials; and measurements of this type are time consuming. It would therefore be useful to have a simple model which could be applied with limited data to determine the critical cooling rate necessary to form a glass. This is particularly important for lunar glasses whose thermal histories are of considerable interest.

When determining the critical cooling rate from a TTT diagram, the only part of the curve which is ultimately required is the nose of the curve. If the time and temperature of the nose could be predicted, the critical cooling rate could also be predicted. According to transformation kinetics, the volume fraction transformed at a time  $t$  is

$$x = \frac{\pi}{3} I_v u^3 t^4 \quad (V-1)$$

where  $I_v$  is the volume nucleation frequency which for homogeneous nucleation only may be expressed:

$$I_v(T) = \frac{N_v^0 kT}{3\pi a_o^3 \eta(T)} \exp - \frac{.02048B T_E^5}{T^3 \Delta T^2} \quad (V-2)$$

and  $U$  is the crystal growth rate, which for normal growth is

$$U(T) = \frac{kT}{3\pi a_o^2 \eta(T)} \left(1 - \exp - \frac{\Delta H \Delta T}{RT T_E}\right) \quad (V-3)$$

Substituting these expressions into Eqn. (V-1) one obtains:

$$x = \frac{N_v^o k^4 T^4 t^4}{243 \pi^3 a_o^9 (\eta(T))^4} \exp\left[-\frac{.02048B T_E^5}{T^3 \Delta T^2}\right] \left[1 - \exp\left[-\frac{\Delta H \Delta T}{RT T_E}\right]\right]^3 \quad (V-4)$$

The time for a volume fraction  $x$  to crystallize is:

$$t(T) = C \frac{\eta(T)}{T} \exp \frac{.02048B T_E^5}{4T^3 \Delta T^2} \left(1 - \exp - \frac{\Delta H \Delta T}{RT T_E}\right)^{-3/4} \quad (V-5)$$

where

$$C = \frac{x^{1/4} (243)^{1/4} \pi^{3/4} a_o^{9/4}}{(N_v^o)^{1/4} k} \quad (V-6)$$

If the temperature of the nose of the TTT diagram is known, the critical cooling rate can be estimated:

$$\left. \frac{dT}{dt} \right|_{\text{crit}} = \frac{T_E - T_{\text{nose}}}{t(T_{\text{nose}})} \quad (V-7)$$

The application of the theory of transformation kinetics to a wide range of materials has produced many TTT and CT curves. The temperatures at the nose are shown in Table V-1 for several classes of materials. If the temperature of the nose is compared with the liquidus temperature, it can be seen that the ratio of these temperatures is approximately constant:

$T_{\text{nose}}/T_E \sim .77$ . Changing the barrier to homogeneous nucleation changes the temperatures of the nose only slightly. The only material which

Table V-1  
Temperature of Nose of TTT Curve Compared with Melting  
Point or Liquidus Temperature

Material	$T_{\text{melt}}$ (K)	$T_{\text{nose}}$ (K) at $\Delta T/T_E = 0.2$	$T_{\text{nose/melt}}$
Apollo 15 Green Glass	1543	1140 (60kT)	.739
Lunar comp. 15286	1483	1129 (60kT)	.761
Lunar comp. 15498	1543	1176 (60kT)	.762
Lunar comp. 60095	1543	1165 (60kT)	.755
Lunar comp. 65016	1633	1207 (60kT)	.739
Lunar comp. 70019	1453	1132 (55kT)	.779
Lunar comp. 79155	1523	1176 (60kT)	.772
$\text{Na}_2\text{O} \cdot 2\text{SiO}_2$	1146	894 (50kT)	.78
$\text{GeO}_2$	1389	1040 (50kT)	.749
Salol	316.6	240 (70kT)	.757
Metal	1234	784 (50kT)	.635
$\text{H}_2\text{O}$	273	202 (50kT)	.74
$\text{SiO}_2$	1996	1540 (50kT)	.772
Anorthite	1823	1389 (60kT)	.762
O-terphenyl	328	269 (50kT)	.82
Lunar comp. 67975	1483	1184 (60kT)	.80

differs significantly from the rest is the silver-like metal, for which a highly approximate  $\eta$ - $T$  relation was used extensively--since neither growth rate data nor even the glass transition temperature is available.

Making the approximation that for all materials

$$T_{\text{nose}} = 0.77 T_E \quad (\text{V-8})$$

Eqn. (V-7) becomes:

$$\left(\frac{dT}{dt}\right)_{\text{crit}} = \frac{T_E - .77T_E}{t(.77T_E)} = \frac{.77(.23)(T_E)^2}{C\eta(.77T_E)} \exp\left(-\frac{.02048B}{4(.77)^3(.23)^2}\right) \left(1 - \exp\left(-\frac{\Delta H(.23)}{RT_E .77}\right)\right) \quad (\text{V-9})$$

or

$$\left(\frac{dT}{dt}\right)_{\text{crit}} = \frac{.177 T_E^2}{C\eta(.77T_E)} \exp\left(-.2117B\right) \left(1 - \exp\left(-\frac{.3\Delta H}{RT_E}\right)\right)^{3/4} \quad (\text{V-10})$$

To predict the critical cooling rate for a material of unknown glass-forming ability, all that remains is to determine or estimate the heat of fusion, the nucleation barrier, and the viscosity at  $.77T_E$ . The heat of fusion is readily measured, but the other two quantities are more elusive.

### 1. Nucleation Barrier

When Turnbull (12) applied nucleation rate theory to his measurements of homogeneous nucleation in liquid metals, he took the free energy for forming a critical nucleus as

$$\Delta G^* = \frac{16\pi}{3} \frac{\sigma^3}{(\Delta G_V)^2} \quad (\text{V-11})$$



where  $\sigma$  is the crystal-liquid specific surface free energy and  $\Delta G_v$  is the difference between the volume free energies of the liquid and crystal. Turnbull used the approximation:

$$\Delta G_v \approx \frac{\Delta H_v \Delta T}{T_E} \quad (V-12)$$

Studies of crystal nucleation have been carried out on a variety of liquids. In estimating the nucleation frequency, and thence the crystal-liquid surface energy, from measurements of the temperature range of homogeneous nucleation, all workers have used the approximation of Eq. (V-12). The values of the surface energy per unit area,  $\sigma$ , have been converted to the surface energy per mole,  $\sigma_M$ , and compared with the molar heat of fusion,  $\Delta H_{fM}$ . The results of the original studies indicated  $\sigma_M/\Delta H_{fM} \sim 1/2$  for metals, and  $\sigma_M/\Delta H_{fM} \sim 1/3$  for non metals.

Vreeswijk and coworkers (9) used a value of  $\sigma_M/\Delta H_{fM} = 0.32$  in calculating critical cooling rates for forming glasses of some materials. They assumed, however, that

$$\Delta G_v \approx \Delta H_v \frac{\Delta T}{T_E} \frac{T}{T_E} \quad (V-13)$$

which is applicable for large undercoolings where account must be taken of the temperature variation of the enthalpy and entropy difference between the crystal and liquid phases. This is not taken into account in Eqn. V-12.

Taking  $\Delta H_{fM} = \Delta S_{fM} T_E$  and  $\sigma_M/\Delta H_{fM} = 0.32$ , Eqns. (V-11) and (V-13):

$$I_v = N_v^\circ v \exp \frac{-0.549 \Delta S_{fM} T_E^5}{R T^3 \Delta T^2} \quad (V-14)$$

For typical values of  $\Delta S_{fM}$ , this indicates high nucleation barriers. For example,  $\Delta S_{fM}$  for  $\text{Na}_2\text{O}\cdot 2\text{SiO}_2$  is about  $4R$ . The exponent in the expression for the nucleation barrier is then  $2.196 T_E^5/T^3 \Delta T^2$ , which corresponds to a nucleation barrier of  $107 \text{ kT}$  at a relative undercooling  $(\Delta T/T_E)$  of  $0.2$ . For  $\Delta S_{fM}$  values of  $5R$ , which correspond to lunar compositions, this would indicate a nucleation barrier of  $134 \text{ kT}$  at a relative undercooling of  $0.2$ . This does not agree with Klein's (18) measurement of  $55 \text{ kT}$  at  $\Delta T/T_E = 0.2$  for lunar composition 70019. Vreeswijk et al. used values of  $\sigma$  calculated according to Eqn. (V-12) with  $I_v$  calculated according to Eqn. (V-13). In order to calculate the crystal nucleation frequency it is necessary to develop an approach which is consistent.

To find a more reasonable approximation for  $\sigma_M/\Delta H_{fM}$  to be used for large undercoolings where Eqn. (V-13) is preferred, the original data were re-examined. The experiments divided various materials into fine droplets, supercooled them and noted the temperature at which they crystallized. In this way, heterogeneous nucleation was avoided in about 99% of the droplets. Following Thomas et al. (23) we assumed that the nucleation rate was  $1 \text{ droplet}^{-1} 10 \text{ sec}^{-1}$ . The calculated nucleation barrier is insensitive to all factors except the undercooling at which crystallization takes place. The nucleation rate may be expressed:

$$I_v = \frac{10 \times 4\pi}{3} r^3 10^{32} \exp\left(\frac{\sigma_M}{\Delta H_{fM}}\right)^3 \frac{\Delta H_{fM} T_E^4}{RT^3 T^2} \text{ sec}^{-1} \text{ cm}^{-3} \quad (\text{V-15})$$

where  $r$  is the radius of the droplet in the nucleation experiment. Taking  $I_v = 0.1 \text{ droplet}^{-1} \text{ sec}^{-1}$  and for solving  $\sigma_M/\Delta H_{fM}$

$$\frac{\sigma_M}{\Delta H_{fM}} = \left( -\frac{3R}{16\pi} \frac{\Delta T^2 T^3}{T_E} \frac{(\ln \frac{.075}{\pi} - 2.303 \times 32 - 3 \ln r)^{1/3}}{\Delta H_{fM}} \right) \quad (\text{V-16})$$

The data and resultant values for  $\sigma_M/\Delta H_{fM}$  are shown in Table V-2. The  $\Delta H_{fM}$  data were taken from the CRC Handbook whenever possible. When the CRC Handbook did not include information on a particular material, the  $\Delta H_{fM}$  data was calculated from Staveley's results. When  $\Delta H_{fM}$  values calculated from Staveley's results are used for all materials, the average value of  $\sigma_M/\Delta H_{fM}$  decreases to 0.27. These values are quite different from the average values determined using Equ. (V-12). If  $\sigma_M/\Delta H_{fM} = 0.25$ , a not uncommon value, the nucleation frequency is

$$I_v = N_v^0 v \exp \frac{-0.26 \Delta S_M T_E^5}{RT^3 \Delta T^2} \quad (\text{V-17})$$

For  $\Delta S_M = 4R$  the exponent is then  $1.04 T_E^5 / T^3 \Delta T^2$ , which corresponds to a nucleation barrier of 51 kT at a relative undercooling ( $\Delta T/T_E$ ) of 0.2. For  $\Delta S_{fM}$  values of  $5R$ , the exponent is  $1.30 T_E^5 / T^3 \Delta T^2$ , which corresponds to a nucleation barrier of 63 kT at a relative undercooling of 0.2.

## 2. Viscosity

A number of theoretical models have been proposed to describe the viscous flow of liquids (81-83). Cukierman (84) found that the free volume model provided the best fit to the high temperature data for anorthite, which is frequently a major constituent of lunar compositions. He also found that the free volume theory described the high temperature

Table V-2

Relative Undercoolings and  $\sigma_M/\Delta H_{FM}$ 

	$\Delta T/T_E$	$\Delta H_{FM}$ (cal mole <sup>-1</sup> )	radius (microns)	$\sigma_M/\Delta H_{FM}$
Mercury	.247	557.2	10	.419
Gallium	.250	1336	10	.342
Tin	.208	1720	10	.349
Bismuth	.166	2505	10	.285
Lead	.133	1224	10	.336
Antimony	.150	4770	10	.260
Aluminum	.140	2550	25	.317
Germanium	.184	8300	7.5	.262
Silver	.184	2700	10	.383
Gold	.172	3030	10	.367
Copper	.174	3110	10	.368
Manganese	.206	3450	25	.401
Nickel	.185	4200	25	.377
Cobalt	.187	3640	10	.394
Iron	.164	3560	15	.379
Palladium	.182	4120	15	.380
Platinum	.181	4700	10	.374
Water	.143	1430	10	.254
Boron Trifluoride	.123	480	25	.278
Cyclopropane	.122	1248*	35	.202
Methyl Bromide	.136	2616	25	.179
Methyl amine	.199	1445*	25	.261
Sulfur dioxide	.167	1778*	25	.233
Chloroform	.250	2103.5	25	.264
Thiophene	.216	1187.2	25	.315
Methyl Chloride	.317	1526*	25	.296
NH <sub>3</sub>	.206	1352*	25	.278

Table V-2 (cont'd.)

	$\Delta T/T_E$	$\Delta H_{fM}$ (cal mole <sup>-1</sup> )	radius microns	$\sigma_M/\Delta H_{fM}$
CCl <sub>4</sub>	.202	783	25	.36
H <sub>2</sub> O	.148	1430	25	.263
C <sub>6</sub> H <sub>6</sub>	.252	2379	25	.280
Br·(CH) <sub>2</sub> ·Br	.235	2591	25	.267
Diphenyl <sup>1</sup> .	.250	4065*	25	.250
Naphthalene	.267	4494	25	.249
CBr <sub>4</sub>	.226	2747*	25	.280
C <sub>6</sub> H <sub>5</sub> CO <sub>2</sub> H	.304	4111*	25	.276
LiF	.210	2360	1.5	.396
LiCl	.210	3200	1.5	.331
LiBr	.240	2900	1.5	.351
NaF	.220	7000	1.5	.292
NaCl	.160	7220	1.5	.239
NaBr	.160	6140	1.5	.248
KCl	.160	6410	1.5	.246
KBr	.170	5000	1.5	.272
KI	.150	4100	1.5	.269
RbCl	.160	4400	1.5	.274
CsF	.140	2450	1.5	.308
CsCl	.170	3600	1.5	.294

\* Calculated from results of De Nordwall and Stavely (22) and Thomas and Staveley (23). Other values are from CRC Handbook.

flow behavior of four organic glass-forming liquids.

Laughlin and Uhlmann (85) found that the glass transition temperature provided a useful normalization of the viscosity data of several liquids. The glass transition temperature was taken as the temperature corresponding to a viscosity of  $10^{15}$  p. It was found that the viscosity vs. reduced temperature  $T_g/T$  for  $\text{SiO}_2$  is similar to that for  $\text{GeO}_2$ . Both exhibit less curvature than the corresponding relation for  $\text{B}_2\text{O}_3$ ,  $\text{Na}_2\text{O}\cdot 2\text{SiO}_2$ ,  $\text{K}_2\text{O}\cdot 2\text{SiO}_2$ , and two standard NBS silicate liquids; and these display a less steeply curved  $\log \eta$  vs.  $T_g/T$  relation than four simple organic glass-forming liquids. If the viscosity vs. reduced temperature relations for lunar compositions are compared with the results of Laughlin and Uhlmann, the flow behavior of the lunar glasses is found to lie between that of oxide liquids and that of simple organic and metal alloy liquids (Fig. V-1).

Using  $T_g$  as a corresponding states parameter, we have obtained a least-squares fit of the Vogel-Fulcher relation

$$\log_{10} \eta = A + \frac{B}{T/T_g - \alpha} \quad (\text{V-18})$$

to the flowdata on 13 lunar compositions. Values of A and B were determined for all compositions with  $\alpha$  varying from 0.8 to 1.2 at intervals of 0.01. The mean and the standard deviation of both A and B were determined at each value of  $\alpha$ . It was found that the best overall fit to the viscosity data for lunar compositions was

$$\log_{10} \eta = -1.60 + \frac{3.12}{T/T_g - 1.83} \quad (\text{V-19})$$

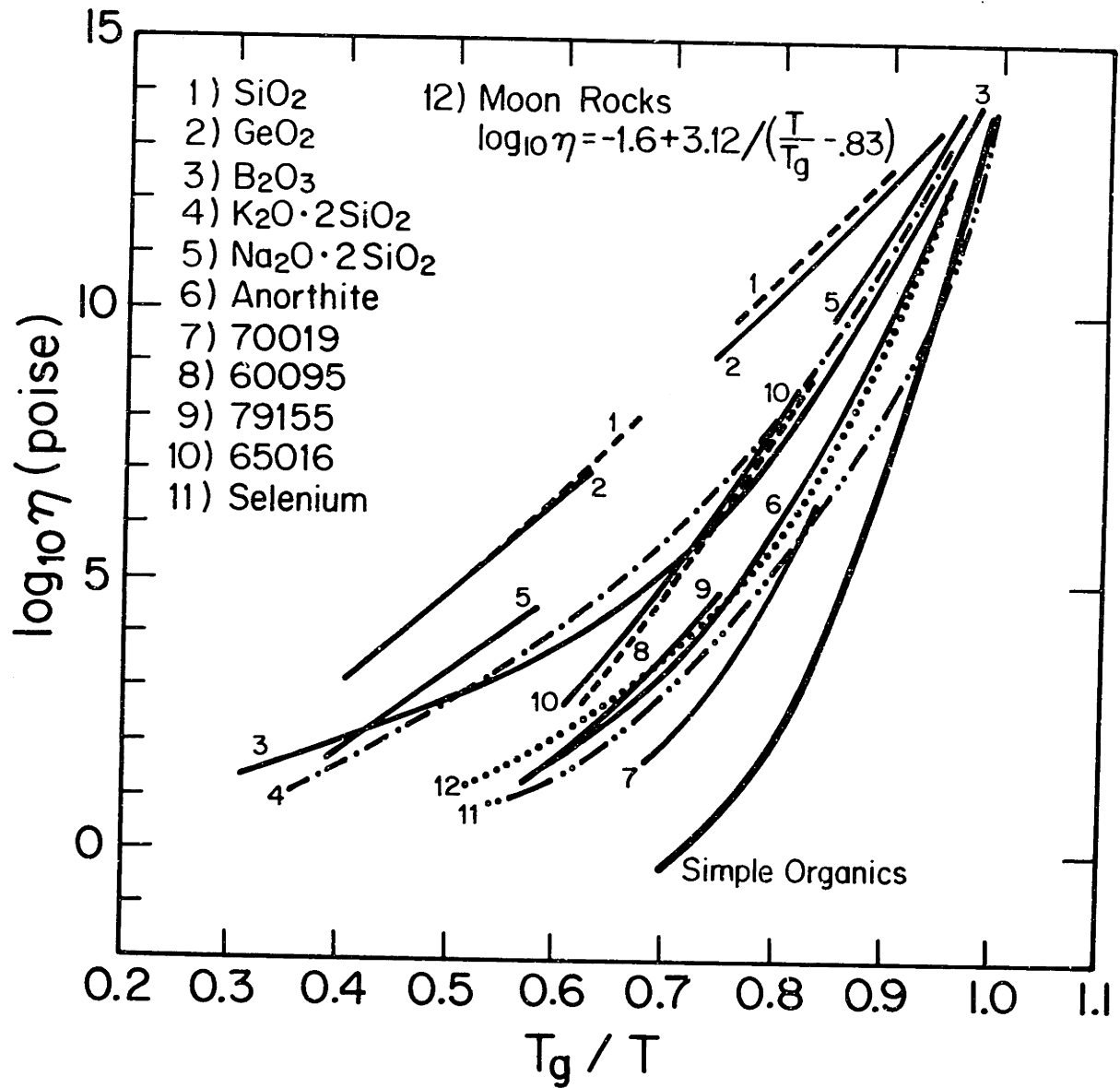


Figure V-1 -  $T_g/T$  normalization of viscosity of glass-forming liquids.

• • • Least squares Vogel-Fulcher fit for lunar compositions.

This relation describes the viscosity at the temperature of interest ( $0.77 T_m$ ) within about an order of magnitude of that interpolated from measurements (see Table V-3).

## B. Results

As a first approximation Eqns. (V-10) and (V-19) were combined to calculate the critical cooling rate for glass formation for several compositions, assuming a uniform nucleation barrier of 60 kT at  $\Delta T/T_E=0.2$ . As a second approximation, the nucleation barrier was then varied by the substitution of Eqn. (V-17) into the expression for critical cooling rate. It was assumed that  $\Delta H_{FM} = \Delta S_M T_E$  for all materials, with  $\Delta S_M=5R$  for lunar compositions and  $\Delta S_M = 6R$  for anorthite. The critical cooling rates for glass formation calculated according to both approaches are shown in Table V-4. These rates are compared with the critical cooling rates calculated from TTT and CT diagrams (18).

The agreement between the first approximation and the TTT diagram from which it is derived, is quite good. The second approximation increases the nucleation barrier to 64 kT for lunar materials and 77 kT for anorthite (both at  $T/T_E=0.2$ ). This change in nucleation barrier decreases the critical cooling rate calculated from TTT and CT diagrams by about a factor of two for the lunar compositions and about a factor of 23 for anorthite. The simplified method agrees in general with the TTT and CT diagrams which use measured values of the viscosity and the growth rate.



Table V-3  
Temperature and Viscosity at the Nose of  
TTT Diagrams

Material	$T_g$ (K)	$T_E$ (K)	$.77 T_E$ (K)	$\log_{10}$ (meas.)	$\log_{10}$ (calc.)
Lunar comp. 67975	940	1483	1142	7.05	6.51
Lunar comp. 14259	970	1513	1165	7.40	6.81
Lunar comp. 14310	950	1583	1219	6.45	5.29
Lunar comp. 15555	900	1548	1192	5.0	4.71
Lunar comp. 68502	1000	1603	1234	6.25	6.12
Lunar comp. 74220	930	1473	1134	6.77	6.41
Lunar comp. 65016	1013	1633	1257	5.30	5.99
Anorthite	1120	1823	1404	5.20	5.77
Lunar comp. 60095	933	1543	1188	5.85	5.44
Lunar comp. 15418	1000	1613	1242	6.35	5.97
Lunar comp. 15498	940	1543	1188	6.37	5.59
Lunar comp. 15286	850	1483	1142	6.25	4.48
Green Glass	850	1543	1188	5.00	3.90

### C. Discussion and Conclusions

The results shown in Table V-4, which are derived using Eqn. (V-17), agree well with experience. The Apollo 15 Green Glass is in fact the most difficult composition to form as a glass among all the lunar compositions tested. Composition 79155 is a relatively poor glass former, and 70019 and 67975 are good glass-formers. The nucleation barrier for the lunar compositions is not significantly different from that calculated assuming  $\Delta G^*=60$  kT at  $\Delta T/T_E=0.2$ . As noted above, Eqn. (V-17) corresponds to a nucleation barrier of 64 kT at  $\Delta T/T_E=0.2$  for  $\Delta S_M=5R$  and a nucleation barrier of 77 kT at  $\Delta T/T_E=0.2$  for  $\Delta S_M=6R$ .

Materials such as anorthite, which have high values of  $\Delta S_M$ , should have high nucleation barriers. In fact, anorthite is a reasonably good glass-former, which is not evident from TTT and CT diagrams constructed using typical values for the nucleation barrier of 50-60 kT at  $\Delta T/T_E=0.2$ . Thus if Eqn. (V-13) is to be used, particularly for oxide materials, smaller values of  $\sigma_M/\Delta H_{fM}$  than those obtained using Eqn. (V-12) must be employed if consistent results are to be obtained.

The differences between the simplified method and the complete method using TTT and CT diagrams are derived from two sources: the viscosity and the temperature at the nose of the TTT diagram. The difference due to the temperature at the nose is not significant. For example, the cooling rate calculated from the TTT diagram of lunar-composition 67975 is  $7 \times 10^{-2} \text{ }^\circ\text{K sec}^{-1}$ . If the viscosity is correct but the temperature is wrong, ( $T_{\text{nose}}=1184 \text{ }^\circ\text{K}$ ;  $T_{.77}=1142 \text{ }^\circ\text{K}$ ), the cooling rate is

Table V-4

Critical Cooling Rates for Glass Formation Calculated from TTT and CT curves and Using Simplified Method of Viscosity Approximation Assuming (1)  $\Delta G^* = 60 \text{ kT}$  and  $\Delta T/T_E = 0.2$ , or (2) Nucleation Barrier from Eq. (V-17)

Material	1			2		
	TTT	CT	Simplified Method	TTT	CT	Simplified Method
Apollo 15 Green Glass	$5.5 \times 10^2$	$2.2 \times 10^2$	$1.4 \times 10^3$	$2.7 \times 10^2$	89	$6 \times 10^2$
Lunar comp. 15286	12	4	$5.3 \times 10^2$	5.5	2	$2.3 \times 10^2$
Lunar comp. 15498	14	5	44	6.4	1.8	19
Lunar comp. 60095	46	15	63	21	7.5	27
Lunar comp. 65016	90	30	20	43	16	8.4
Lunar comp. 70019	$3.3 \times 10^{-1}$	$10^{-1}$	4.2	$1.4 \times 10^{-1}$	$38 \times 10^{-1}$	1.8
Lunar comp. 79155	6.9	2.3	$2.3 \times 10^2$	2.9	$8 \times 10^{-1}$	$10^2$
Lunar comp. 67975	$6.9 \times 10^{-2}$	$1.3 \times 10^{-2}$	4.9	$2.6 \times 10^{-2}$	$6.7 \times 10^{-3}$	2.5
Anorthite	$10^3$	$4 \times 10^2$	81	44	14	2.3

$3.4 \times 10^{-2} \text{ } ^\circ\text{K sec}^{-1}$  which differs by only a factor of 2. However, if the approximation for the viscosity is not good, the critical cooling rate will not be well described by the simplified model. The largest discrepancy in viscosity occurs for lunar composition 15286 which is much more viscous than the viscosity approximation would indicate. Accordingly, the simplified method overestimates the difficulty of forming a glass.

The determination of a critical cooling rate for glass formation has been reduced to three measurable quantities: the glass transition temperature, the melting temperature and the molar heat of fusion. For ease of glass formation, the heat of fusion should be high, so that the nucleation frequency is low; the liquidus temperature or melting point should be low and the glass transition temperature should be high. The melting temperature may be high if the glass transition temperature is also high; but a high melting temperature and a low glass transition temperature indicate a poor glass-former (Apollo 15 green glass). This is in accord with the previous findings.

## VI. CRYSTALLIZATION STATISTICS

### A. The Model

Hopper et al. (25) have developed a theory of crystallization statistics by which the state of crystallinity of a material can be determined if the thermal history is known and the thermal history of a material can be determined if the state of crystallinity is known. The assumptions used in deriving the crystal distribution function  $\psi$  have been discussed in Chapter II. According to Hopper et al., a crystal nucleating at a time  $t_0 < t$  has a radius at time  $t$  of

$$R(\vec{r}, t, t_0) = \int_{t_0}^t u[T(\vec{r}, t')] dt' \quad R > 0 \quad (\text{VI-1})$$

and the change in crystallite size with nucleating time is

$$\frac{\partial R}{\partial t_0} = -u[T(\vec{r}, t_0)] \quad (\text{VI-2})$$

Eq. (VI-2) is very important when deriving the expression for the crystal distribution function

$$\psi(\vec{r}, t, R) = \frac{I_v\{T[r, t_0(\vec{r}, t, R)]\}}{u\{T[r, t_0(\vec{r}, t, R)]\}} \quad (\text{VI-3})$$

which is used in calculating the number density of crystals

$$D_N(\vec{r}, t) = \int_0^{R_{\max}} \psi(\vec{r}, t, R) dR \quad (\text{VI-4})$$

and the volume fraction crystallized

$$F_v(\vec{r}, t) = \int_0^{R_{\max}} \frac{4}{3} \pi R^3 \psi(\vec{r}, t, R) dR \quad (\text{VI-5})$$

where

$$R_{\max}(\vec{r}, t) = \int_0^t u [T(\vec{r}, t')] dt' \quad (\text{VI-6})$$

In the present analysis it was assumed that the sample is of uniform temperature so there is no  $\vec{r}$  dependence of either nucleation frequency or growth rate. Furthermore it is noted that the radius of a crystal is a function of its initial size as well as the growth rate, time, and temperature. That is

$$R(t, t_0) = \int_{t_0}^t u [T(t')] dt' + R^* [T(t_0)] \quad (\text{VI-7})$$

The radius of the critical nucleus,  $R^*$ , can be determined from classical nucleation theory:

$$R^* = \frac{2\sigma}{\Delta G_v} \quad (\text{VI-8})$$

where  $\sigma$  is the specific interfacial energy and  $\Delta G_v$  is the free energy difference between the crystal and liquid phases. In the present analysis, it was assumed that

$$\Delta G_v = \Delta H_v \frac{\Delta T}{T_E} \frac{T_0}{T_E} \quad (\text{VI-9})$$

where  $T_0 = T_0(t_0)$  and  $\Delta T = T_E - T_0(t_0)$

Using the results of Chapter V for non-metals

$$\frac{\sigma_M}{\Delta H_{fM}} \approx 0.25 \quad (\text{VI-10})$$

where  $\Delta H_{fM} = \Delta H_v V_m$  and  $\sigma_M = \sigma V_m^{2/3} N_o^{1/3}$ ;  $V_m$  is the molar volume and  $N_o$  is Avogadro's number. Therefore

$$R^* \approx \frac{0.5 V_M^{1/3} T_E^2}{N_o^{1/3} \Delta T T_o} \quad (\text{VI-11})$$

and hence  $R$ , the crystal size, is a function only of  $t$  and  $t_o$ .

It is assumed that if at any time and temperature the crystallite is smaller than the critical size corresponding to that temperature, it will melt completely and will not be included in any future calculations of crystal distribution; that is,

$$\psi(t, t_o) = 0 \quad (\text{VI-12})$$

when  $R(t', t_o) < R^*(t')$  for some  $t'$  on  $(t_o, t)$ . There will be a range of  $R(t, t_o)$  for which  $R(t', t_o) > R^*(t')$  and the number of crystallites in that range can be calculated.

The number of crystals nucleating during the time interval between  $t_1$  and  $t_2$  in the volume  $dv$  is

$$dN_{12} = dv \int_{t_1}^{t_2} I_v [T(t_o)] dt_o \quad (\text{VI-13})$$

From Eqn. (VI-7), one obtains

$$\frac{\partial R}{\partial t_o} = -u [T(t_o)] + \frac{\partial R^*}{\partial t_o} \quad (\text{VI-14})$$

Changing variables in Eqn. (VI-13),

$$dN_{12} = dv \int_{R_2 - R_2^*}^{R_1 - R_1^*} - \frac{I_v}{u} d(R - R^*) \quad (\text{VI-15 a})$$

or

$$dN_{12} = dv \int_{R_1}^{R_2} \frac{I_v}{u - \frac{dR^*(t_o)}{dt_o}} dR \quad (\text{VI-15 b})$$

where  $R_1 = R(t, t_1)$  and  $R_2 = R(t, t_2)$ . Therefore

$$\psi(r, R) = \frac{I_v \{T[t_o(t, R)]\}}{u\{T[t_o(t, R)]\} - \frac{dR^*}{dt_o(t, R)} [t_o(t, R)]} \quad (\text{VI-16})$$

As will be shown, the inclusion of  $R^*$  in the expression for crystallite size is significant when calculating the volume fraction crystallized. When the temperature is cycled below the glass transition, where the growth rate is essentially zero but  $dR^*/dt_o$  is not, as well as when a sample is cooled below and reheated above the glass transition, the modification of Eqs. (VI-7) to (VI-16) is necessary to obtain reliable results.

An alternative method of calculating the volume fraction crystallized in a material with a known thermal history is to integrate the number of nuclei and their volume over time

$$F_v(t) = \int_0^t \frac{4}{3} \pi R(t, t_o)^3 I_v [T(t_o)] dt_o \quad (\text{VI-17})$$

where the finite size of the critical nucleus must in general be considered.

In the work that follows, the volume fraction crystallized has been calculated for several materials with thermal histories that include quenching from the melt to a temperature below the glass transition temperature and subsequent reheating until crystallization takes place. This is a method used in many laboratory measurements of the glass-forming ability of materials. Using differential thermal analysis (DTA) or differential scanning calorimetry (DSC), the temperature at which a sample



crystallizes  $T_{cr}$  is determined.

Hruby (27) has formulated a parameter

$$K_{gl} = \frac{T_{cr} - T_g}{T_E - T_{cr}} \quad (\text{VI-18})$$

as a measure of glass-forming ability. Using Eqn. (VI-17), the variation of  $K_{gl}$  with cooling rate, heating water and assumed nucleation barrier can be determined.

To determine the crystallization temperature of several materials, Eqn. (VI-17) was integrated numerically. The growth rate and viscosity for each material were determined in the same way as in Chapter IV. The nucleation barrier was varied in the range suggested by the results of Chapter V and by previous workers.

$$I_v = N_v^0 \exp \left[ \frac{-0.02048B T_E^5}{(\Delta T)^2 T^3} \right] \quad (\text{VI-19})$$

where  $B = 40-85$  which corresponds to a nucleation barrier of  $BkT$  at a relative undercooling of 0.2. At every step in the integration, the crystallite sizes were compared with the critical nucleus size for that temperature and any that were smaller than the critical sizes were no longer included in calculations of the volume fraction crystallized.

When materials show significant crystallization over a range of temperature, it is necessary to take into account the effects of excluded volume. Therefore, when the degree of crystallinity exceeded 10%, the volume fraction crystallized was taken as:

$$F_v(t) = 1 - \exp \left\{ - \int_0^t \frac{4}{3} \pi R(t, t_0)^3 I_v[T(t_0)] dt_0 \right\} \quad (\text{VI-20})$$

The temperature range during which the greatest amount of crystallization took place was taken as the crystallization temperature. An alternative approach is to take the temperature at which significant crystallization first occurs as the crystallization temperature. In comparing the calculations with actual DTA and DSC runs, both approaches depend on the sensitivity and response time of the equipment. The latter method also depends on the definition of "significant crystallization". If the latent heat of fusion is known, it is possible to construct the entire crystallization curve directly from the results of the calculations. In the results that follow, only comparisons of the temperatures at the beginning and end of crystallization and the temperature of maximum crystallization rate are made.

Several DTA and DSC runs were made on a variety of materials to compare the results of calculations with experimental data. Several lunar materials, oxide glass formers and two simple organic glass formers were studied. The ceramic samples were from the same melts as the samples used in the crystal growth, viscosity and nucleation studies discussed in Chapter IV and V. These samples had been quenched by being poured onto an aluminum plate. Although this is often an effective test of glass-forming ability, the actual cooling rate is not known. As will be shown, the cooling rate can have a significant effect on the crystallization temperature. These samples were heated at rates of 10 and 20 C min<sup>-1</sup>. Less than 10 mg of sample were required for each run.

The organic materials, salol and o-terphenyl, were tested in a DSC which had been cooled to about -30C before inserting the sample.

This made it possible to melt the samples under controlled conditions so their melting points could be checked to ensure that extensive degradation had not taken place during storage. The melting temperatures were the same as the published values. The samples were then held at a temperature about 15C above the melting temperature to reduce the effect of heterogeneous nucleation. They were then cooled at a rate greater than 20 C min to about 15C below their glass transition temperature and reheated at rates of 0.625 to 20 C min<sup>-1</sup>. These samples could be remelted and used again.

## B. Results

The calculated values of  $K_{gl}$  for SiO<sub>2</sub>, GeO<sub>2</sub> and salol are shown in Fig. VI-1 for heating rate of 10<sup>-7</sup> to 10<sup>-2</sup> °sec<sup>-1</sup>. Most of this range of heating rates is not experimentally practical, so the calculated values of  $K_{gl}$  cannot be tested. As would be expected, SiO<sub>2</sub> would crystallize only at very low heating rates and GeO<sub>2</sub> would crystallize at somewhat higher heating rates. If a material is heated at a rate which is too high, the temperature of the material would reach the liquidus before appreciable crystallinity could develop. Salol was melted well above its liquidus, quenched in a liquid nitrogen cooled DSC and reheated at a rate of 0.01°/sec. It did not crystallize. If the actual nucleation barrier for salol is 60 kT and  $\Delta T/T_E = 0.2$ , it should crystallize at about 285 K ( $K_{gl} \sim 2.3$ ). That it did not indicate that the nucleation barrier is higher and it is a better glass-former than previously thought.

The crystallization temperature has been measured for three materials, o-terphenyl, lunar composition 65016 and anorthite. The measured and calculated crystallization temperatures for o-terphenyl are shown in

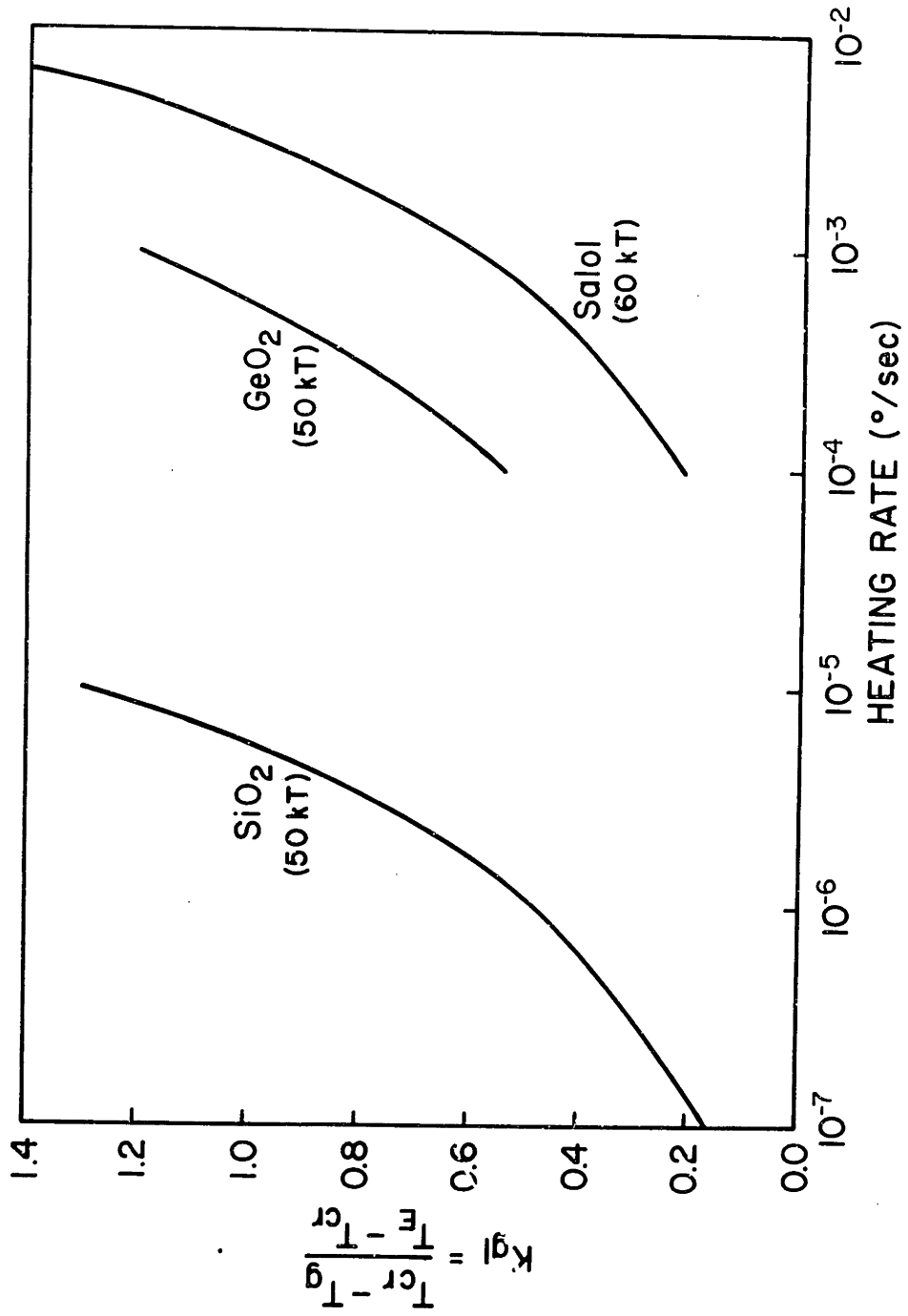


Figure VI-1 - Calculated  $K_{gl}$  values vs. heating rate for  $SiO_2$ ,  $GeO_2$  and salol.

Fig. VI-2 for heating rates of 0.625 to 20°/min (0.01 to 0.33°/sec). The agreement is very good. For o-terphenyl, a nucleation barrier of 50 kT at a relative undercooling of 0.2 was assumed. For 65016 and anorthite the DTA results could be matched by the calculations if the assumed nucleation barriers were 73 and 85 kT respectively.  $K_{g1}$  for 65016 and anorthite are shown in Fig. VI-3. The calculated and measured values for o-terphenyl are shown in the same figure for comparison. Although o-terphenyl has a much lower nucleation barrier than 65016 and anorthite, its  $K_{g1}$  value is much greater than that of 65016 and anorthite at any given heating rate. It is also more easily formed as a glass.

Lunar compositions 70019 and 79155 were also crystallized by DTA. They were much poorer glass formers than predicted by crystallization statistics; that is, they crystallized at much lower temperatures. The viscosity-temperature relation at low temperatures is not well known for these materials. When calculating TTT and CT curves, the only relevant portion of the temperature range is that between the melting point and the nose. However when reheating from below  $T_g$ , the nucleation frequency and growth rate below the nose, both of which depend on the viscosity, can have a significant effect on the crystallization temperature. If the cooling rate is not fast enough, the volume fraction of crystallites at  $T_g$  can affect the measured crystallization temperature. The effect of cooling rate on  $K_{g1}$  calculated for 70019 is shown in Fig. VI-4. It was found that in general, the volume fractions crystallized less than  $10^{-9}$  -  $10^{-10}$  have no effect on crystallization temperature, but larger volume fractions crystallized decrease the crystallization temperature.

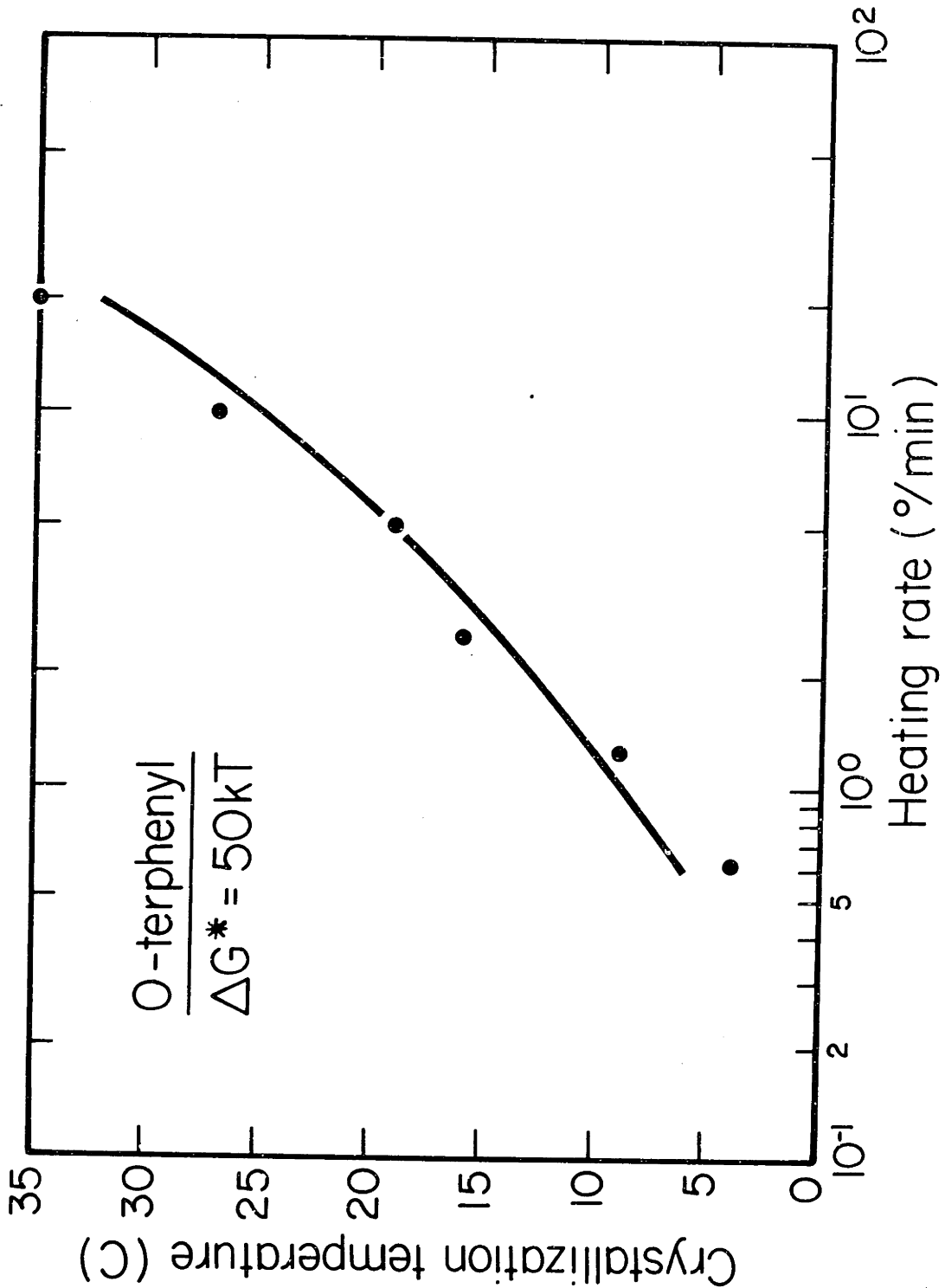


Figure VI-2 - Measured and calculated crystallization temperature vs. heating rate relation of o-terphenyl.

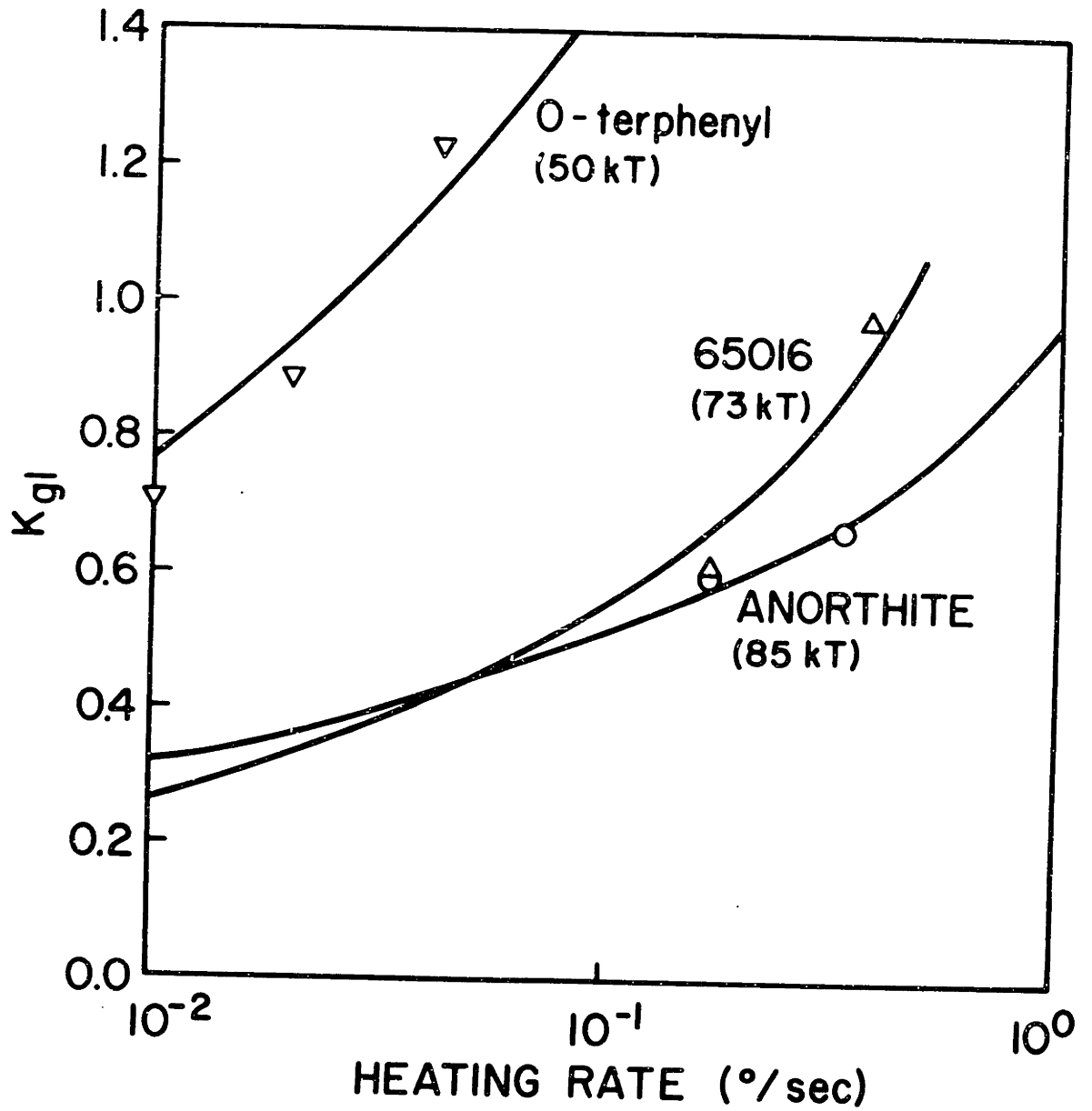


Figure VI-3 - Measured and calculated  $K_{g1}$  vs. heating rate relation of o-terphenyl, anorthite, and lunar compositions 65016.

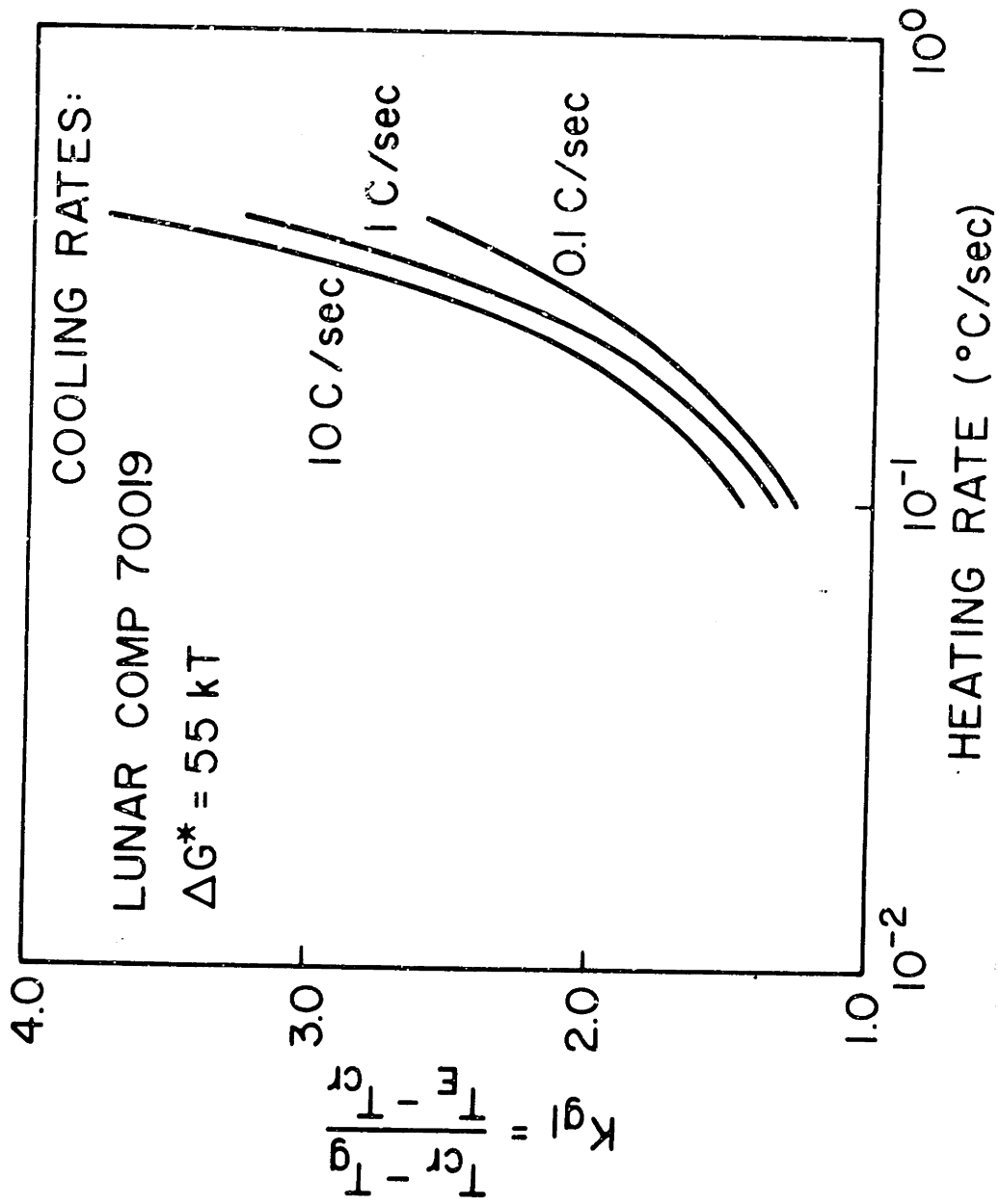


Figure VI-4 - Effect of cooling rate on calculated  $K_{g1}$  vs. heating rate relation for lunar composition 70019.



### C. Discussion and Conclusions

$K_{gl}$  is one parameter which can be easily measured and which gives an indication of the glass-forming behavior of a material. However its value does not provide an absolute measure of glass forming ability. Rather, the relative values of  $K_{gl}$  for a variety of materials gives an indication of their relative glass-forming ability.

When using crystallization statistics to calculate  $K_{gl}$  for a material, a variable that has a pronounced effect on the crystallization temperature is the nucleation barrier. The effect of changing the estimated nucleation barrier on  $K_{gl}$  for anorthite is shown in Fig. VI-5. An early estimate (8) of the nucleation barrier was 50 kT at a relative undercooling of 0.2. The excellent agreement of the experimental data for anorthite with that assuming a nucleation barrier of 85 kT emphasize the importance of being able to predict accurately the nucleation barrier in materials. According to the analysis of the previous chapter, for anorthite a nucleation barrier of 85 kT corresponds to a molar entropy of fusion of 6.7 R; according to the constant cooling curve derived from the TTT curves for homogeneous nucleation of Chapter IV, the critical cooling rate is 0.33°/sec. For lunar composition 65016, a 73 kT nucleation barrier indicates a molar entropy of fusion of 5.75 R and a critical cooling rate of 0.25°/sec.

Hruby suggested that  $K_{gl}$  be used as an indication of the glass-forming ability of a material. This is based on the assumption that the thermal stability of a glass is directly proportional to the ease of its formation. Hruby also assumed that at  $T_g$  all glasses are in comparable

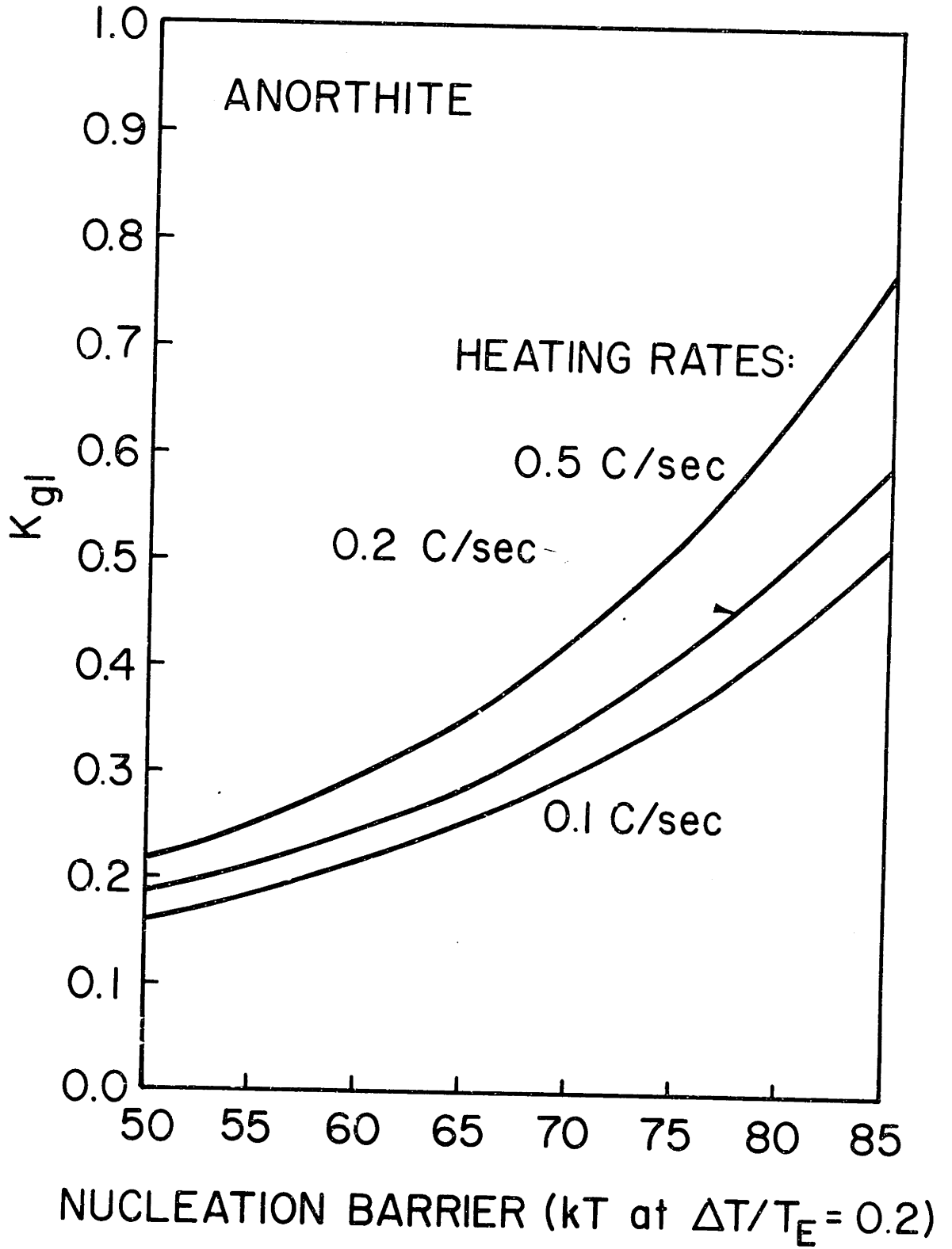


Figure VI-5 - Calculated  $K_{gl}$  values for anorthite as a function of assumed nucleation barrier.

states. From Fig. VI-4, it can be seen that this is not in general true and that  $K_{gl}$  depends on the cooling rate as well as the heating rate.

CT curves and the critical cooling rate can be calculated from crystallization statistics as well as from isotherm TTT curves. A comparison of the resultant curves is shown in Fig. VI-7 for lunar composition 67975. The approximation suggested by Grange and Kiefer overestimates the degree of crystallinity at the nose of the CT curve at a given cooling rate. They ignore any crystallization which may take place below the nose of the CT diagram, when actually, according to crystallization statistics some crystallization takes place to temperatures well below the nose. The temperature of the nose as calculated from the CT curve derive from the TTT diagram agrees with that calculated from crystallization statistics, the latter being defined as the temperature interval in which the change in volume fraction crystallized is a maximum. However it is necessary to cool to a lower temperature than the nose to avoid a given volume fraction crystallized. The ratio of the volume fraction crystallized at the nose to that at the glass transition temperature is constant (about 0.62 for 67975) and does not depend on the cooling rate.

In toto, crystallization statistics is a powerful tool in determining the glass-forming ability of a material. Combined with the experimental determination of the crystallization temperature it can be used to estimate closely the nucleation barrier of a material. It can also be used to check the reliability of other models in predicting critical cooling rates. However, care must be taken to avoid the effects of insufficient quenching and heterogeneous nucleation. Crystallization

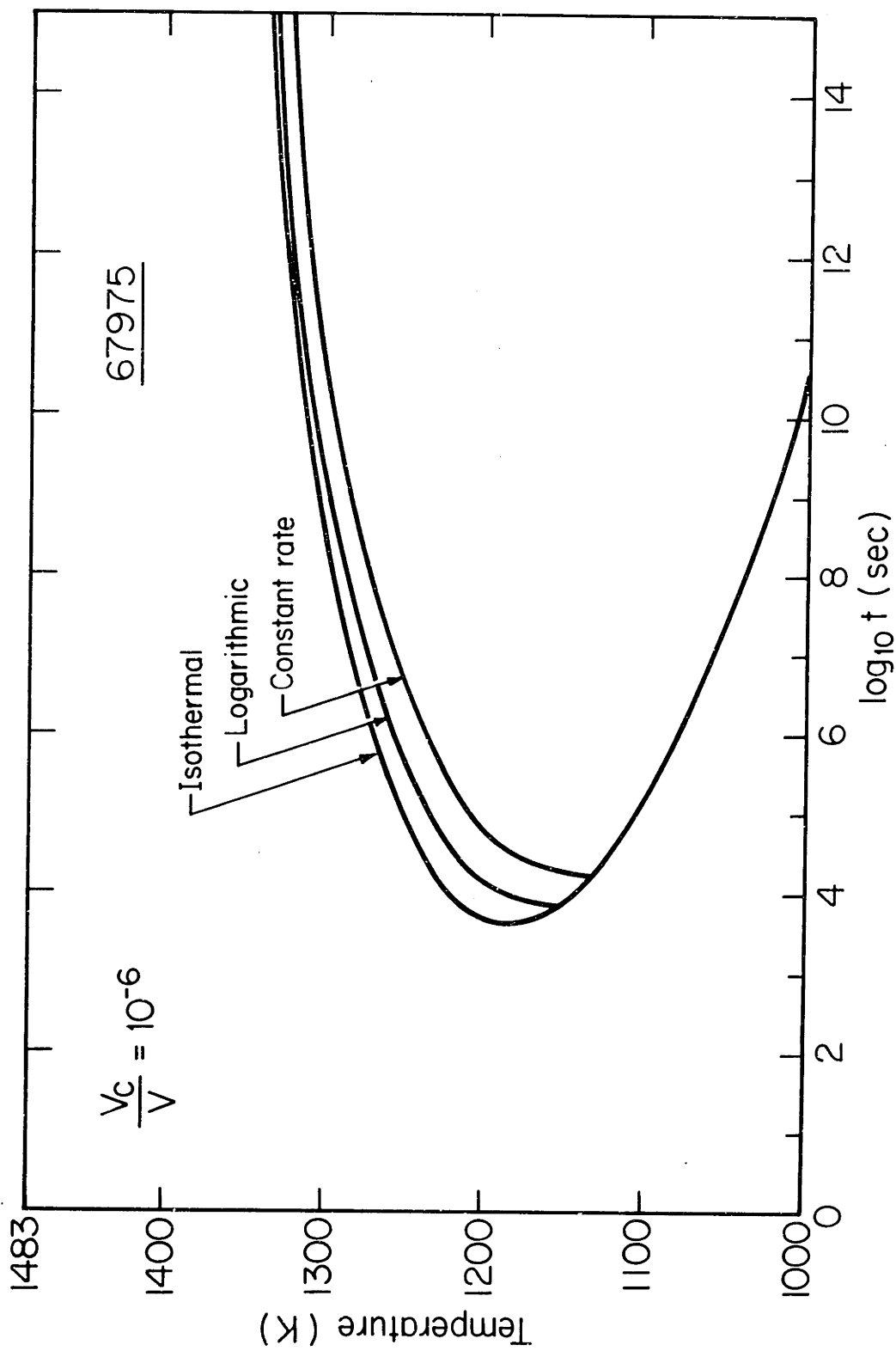


Figure VI-6 - Constant cooling (CT) diagram for lunar composition 67975 corresponding to volume fraction crystallized of  $10^{-6}$ , constructed from TTT diagram by technique described in Chapter IV.

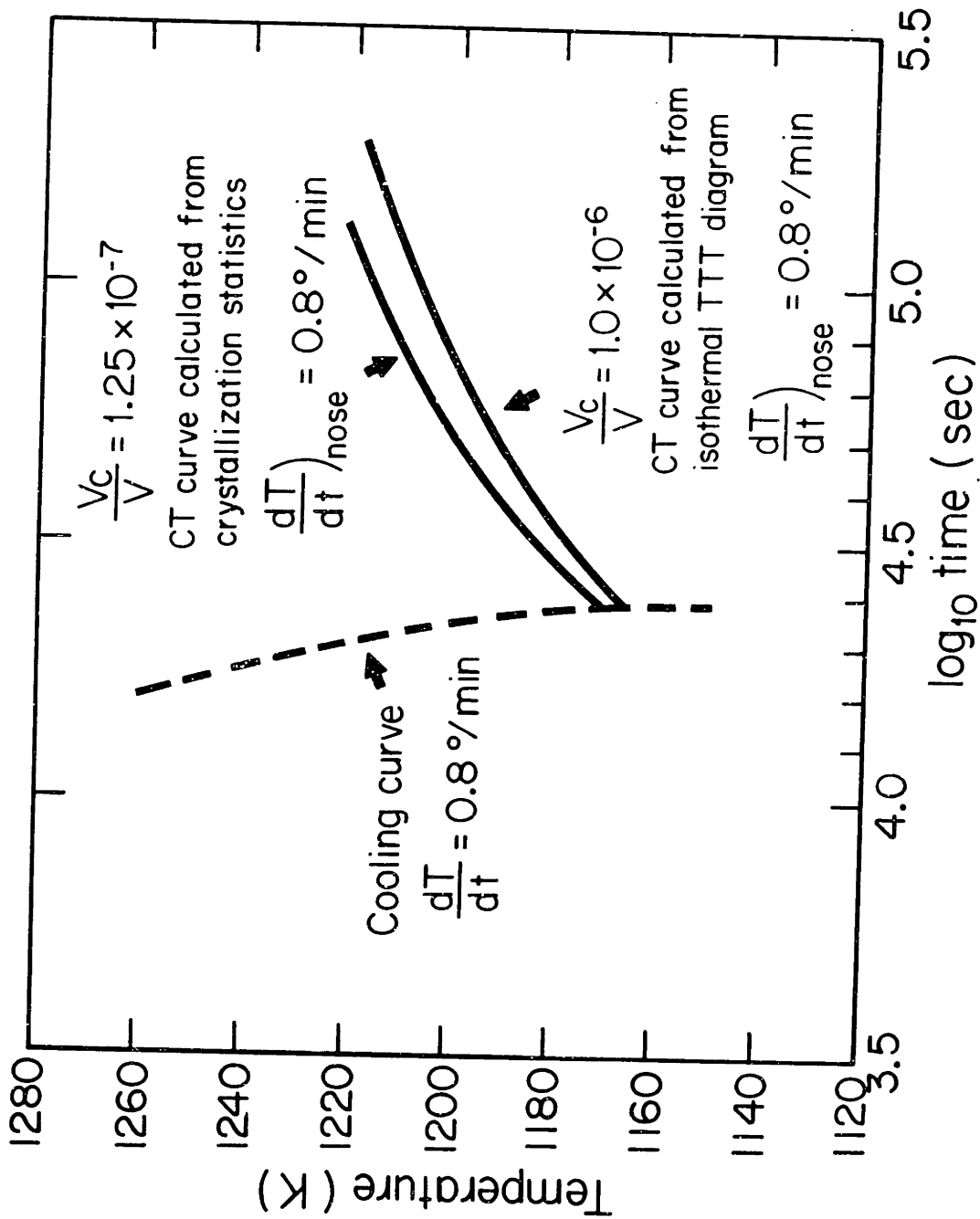


Figure VI-7 - Nose of CT curve for lunar composition 67975 constructed from TTT diagram and from crystallization statistics.

below the nose of CT curves must be taken into account if a given volume fraction crystallized is to be avoided.

Hruby's parameter  $K_{g1}$  does not result in direct comparison of the relative glass-forming ability of several materials. The method presented in Chapter II which uses three experimental parameters (melting temperature, glass transition temperature and heat of fusion) provides a more reliable ranking of the glass-forming ability of materials. Therefore while Hruby's approach could be used as a check of the applicability of other models, it is necessary to calculate the critical cooling rate for glass formation by more rigorous techniques.

## VII. THE THERMAL HISTORY OF IMPACT MELTS

This chapter reports the results of calculations which quantify the model proposed by Simonds (30) to describe the thermal history of impact melts. In particular it is applied to two impact sites, one lunar--The Apollo 17 Station 6 Boulder--and one terrestrial--The Manicouagan Structure in Quebec. The thermal history is divided into two stages: (1) heat transfer between a superheated silicate liquid and enclosed clasts; and (2) heat transfer from the melt sheet to the surroundings. The two stages are modeled separately because the dimensions of the heat flow problem differ by a factor of over 100 and the relevant geometry of initially hot and cold regions is different. Calculations of this form have broad applicability to the cooling of other melts in which cold material is picked by a hot liquid. It is implicit in the calculations that the hot and cold materials are mixed very rapidly. While sizable thermal gradients must exist in the melt immediately after its formation, velocities of several  $\text{km sec}^{-1}$  are expected for the melt (86) which presumably mix the liquid very well. The extreme chemical homogeneity of the Station 6 Boulder (30) and Manicouagan (87) as well as other impact melts (88-90) support the assumption of thorough mixing of the liquid in times shorter than are required for thermal equilibration and crystallization.

### A. The Model

The lateral dimensions of the melt sheet are assumed to be large compared with its thickness, so the heat flow problem can be reduced to

the one-dimensional heat flow equation:

$$\rho C_p(T) \frac{\partial T}{\partial t} = k_{TH} \frac{\partial^2 T}{\partial X^2} \quad (\text{VII-1})$$

Here  $\rho$  is the density;  $C_p$  is the heat capacity, assumed a function of temperature,  $T$ ;  $t$  is the time;  $k_{TH}$  is the thermal conductivity.

Equation (VII-1) has been solved by replacing the differential equation by its backward difference analog:

$$\rho C_p(T) \frac{T_{i,n+1} - T_{i,n}}{\Delta t} = k_{TH} \frac{T_{i+1,n+1} - 2T_{i,n+1} + T_{i-1,n+1}}{(\Delta X)^2} \quad (\text{VII-2})$$

where  $n$  indicates a point in time where the solution is known and  $i$  indicates a point in space. The appropriate boundary conditions were applied and the solution found by the Thomas Tridiagonal method (91).

In this problem, the heat capacity--and sometimes the boundary conditions--are functions of temperature, which makes the equation nonlinear. The correct solution was approached by using the temperature at time  $n$  to predict the coefficients at time  $n+1$ . The procedure was iterated using the predicted values for time  $n+1$  to calculate the solution at that time again. This was repeated as many times as required; only 1 to 3 iterations were needed for the short-time (first-stage) problem, while as many as 5 were sometimes used for the long-time (second-stage) problem. The solution converged quickly, particularly when the change in temperature or time interval was small. At very long times, the results sometimes became unstable, resulting in severe oscillations about the correct solution, particularly at the surface where the temperature was changing quickly. This problem was corrected by averaging the results



of previous iterations in calculating future iterations.

The latent heat of fusion was taken into consideration using the assumption of Jaeger (39) that the latent heat ( $L$ ) is liberated uniformly over the temperature range between the liquidus ( $T_L$ ) and the solidus ( $T_S$ ), so the heat capacity in that range can be replaced by:

$$C'_p = C_p + \frac{L}{T_L - T_S} \quad (\text{VII-3})$$

The latent heat of fusion and heat capacity of the melt have been approximated by those of diopside  $103 \text{ cal g}^{-1}$  and  $.251 + .265 \times 10^{-4}T - .69 \times 10^{-4}T^{-2} \text{ cal g}^{-1}\text{K}^{-1}$  respectively (92).

The thermal conductivity was taken as  $4 \times 10^{-3} \text{ cal cm}^{-1} \text{ sec}^{-1}\text{K}^{-1}$ , a value typical for glass-forming silicate liquids at modest temperatures. At high temperatures, radiative transport can make a significant contribution to the heat flow in transparent materials. For iron-rich materials, such as the boulder composition, their large optical absorption coefficients make the radiative contribution to  $k_{TH}$  quite small, at least up to temperatures of  $1500^\circ\text{K}$ . For this reason, a constant value of the thermal conductivity was employed in all calculations reported here.

The effects of a temperature dependent  $k_{TH}$  have previously been explored in the heat flow calculations of Hopper et al. (26) concerned with other lunar melts.

#### 1. Short-time (first-stage) problem

The short-time problem has been represented by a small region of thickness  $X$ , consisting of a mixture of melt and randomly distributed

clasts. It was assumed that there is no convection nor any heat flow into or out of this small region, that is

$$\frac{\partial T}{\partial X} = 0 \text{ at } X = 0, X_1 \quad (\text{VII-4})$$

where  $X_1 = 1 \text{ cm}$  for the Station 6 boulder and  $X_1 = 10 \text{ cm}$  for Manicouagan. The initial temperature distribution is assumed to be bimodal, with cold clasts all at one temperature and hot melt all at another temperature. In the lunar sample, the lack of lamellae or textures suggestive of recrystallized feldspar glass suggests that the clasts still visible were not exposed to shock pressures greater than 150 kbar. Such low shock pressures are compatible with shock heating of clasts to temperatures of no more than 200C (93). In the calculations for lunar and terrestrial impact melts, all clasts were assumed to start at 100C. The initial temperatures of impact melts are not known and the calculations treat a broad range, from the liquidus to 2500C. Studies of Ries glasses (94, 95) suggest several hundred degrees of superheat, and numerical calculations (86) also support the suggestion that the melt is substantially superheated.

For the calculations of short-time cooling in the Station 6 boulder, the 1 cm representative region was divided into 1000 ten micron units. The clasts still visible in thin sections of the boulder range in size down to about 50  $\mu\text{m}$ , beyond which recognition becomes difficult. As will be discussed below, there are reasons to believe that preferential digestion of small clasts may have taken place. Most of the clasts visible in thin sections range in size from 50 to 500  $\mu\text{m}$ . The clasts

were assumed to have a log-normal size distribution with a median of 100  $\mu\text{m}$  and a standard deviation of a factor of 4. This was done by using computer-generated random numbers, which determined if a clast would exist at a point. If so, the particle size was chosen using a method which relies on the central limit theorem (96) and generates numbers in a normal distribution. The particle size was rounded to the nearest 10  $\mu\text{m}$  and the requisite number of clast units were initialized at the starting clast temperature of 100C. The clasts could melt when the temperature at a point exceeded the liquidus of the melt, 1310C and such a point was then considered part of the melt.

This approximation of uniform clast melting underestimates the fraction of clasts digested, since in the natural situation some clasts would melt at temperatures below the liquidus. The melting of clasts in a melt is not a process of complete chemical equilibrium since substantial time is required for the material digested to diffuse into the melt, and as will be seen below, the process of clast-melt thermal equilibrium is extremely rapid. In effect, many clasts are surrounded by melts of essentially their own composition, greatly increasing the effective melting point above the equilibrium temperature for the composition of the melt.

In treating the first stage cooling of Manicouagan, it was assumed that the melt sheet was a random mixture of clasts with a log-normal size distribution and a median size of 1.0mm with a standard deviation of a factor of 3. The 10 cm representative section was divided into 100  $\mu\text{m}$  units; the smallest clast taken as 100  $\mu\text{m}$  and the largest as 1 cm.

Four types of clasts have been included in these calculations. Each type was assigned a different liquidus and solidus. The clasts were assumed to have the same density, heat capacity, thermal conductivity and mineralogy as the melt sheet, for which the sequence of crystallization is the following: Type 1, plagioclase (first 25%, melting range = 1131-1175 C); Type 2, plagioclase and pyroxene (heat 28%, melting range = 1082 - 1131C); Type 3, alkali feldspar and opaques (36%; melting range = 1019-1082C); and type 4, alkali feldspar plus quartz (last 11%, melting range = 1000-1019C).

Calculations have also been carried out for systems with large volume fractions of either high-melting or low-melting clasts; and the results of these calculations are compared with those for the standard distributions.

The melting properties as well as the clast size assigned to a clast have been determined by independent random processes. There was taken to be no correlation between clast size and clast type, although such a correlation might be useful in some applications. In some calculations, the random number sequence was initialized by the programmer only once when the clast and melt distributions were being determined. In other sets of calculations, the sequence was initialized at the same point for successive calculations in order to explore the effect of various initial temperatures on particular distributions of clast type and clast size.

Because of the random nature of the process used to identify the size and type of clast (if any) at a given point, as well as the modest

population sampled, the detailed distributions of clast sizes and types in a given calculation could differ significantly from the observed distributions. To obtain a distribution of clast types which corresponds closely to the observed volume fraction of clasts of different types and has the desired total volume fraction of clasts, it was necessary to try many sequences of random numbers. For example, the distribution of clasts with total initial volume fraction of 0.235 was chosen from 200 calculated clast distributions having a nominal volume fraction of 0.20. These distributions ranged in clast content from 0.05 to 0.35. The sample chosen was the one which fit most closely the desired volume fraction of clasts and the distribution of clast types.

It has been assumed that crystallization and melting take place in a linear distribution between the overall liquidus (1175C) and the solidus (1000C) of the melt. This is similar to the assumption used by Simonds et al. (35). The liquidus ( $T_{LC}$ ) and solidus ( $T_{SC}$ ) of each type of clast are determined such that

$$V_{fc} = \frac{T_{LC} - T_{SC}}{T_L - T_S} \quad (\text{VII-5})$$

where  $V_{fc}$  is the volume fraction of each type of clast assumed above. The liquidus of one type of clast is taken as equal to the solidus of the next most refractory type of clast.

Two criteria for the melting or partial melting of a clast were used: (1) similar to the calculations for the Apollo 17 Station 6 Boulder, a clast or part of a clast could melt when its temperature was greater than its liquidus (not necessarily the same as the liquidus of the melt)

and (2) similar to the simplified calculations of Simonds, a clast could partially melt when its temperature is above its solidus but below its liquidus. The temperatures to be considered when determining the extent of clast digestion at a point are the highest temperatures attained at that point at any time during the approach to equilibrium. They are not necessarily the same as the final equilibrium temperature. The extent of partial clast melting due to raising the temperature above the solidus is added to that due to complete melting due to raising the temperature above the liquidus. This approach could slightly overestimate the extent of clast digestion depending on the kinetics of melting of a particular type of clast. On the other hand, Simonds model would underestimate the degree of clast digestion because it ignores any melting which may take place during the approach to equilibrium. A quantitative comparison of the effect on fractional clast digestion of several approaches to this problem will be made.

The calculations were used to provide information about the rate of cooling due to the included clasts, the maximum temperature to which a clast is raised and the fraction of clasts which remain when the uniform temperature is reached--all as a function of the superheat and the initial volume fraction of clasts in the melt.

## 2. Long-time (second-stage) problem

The setting of the melt sheet from which the Apollo 17 Station 6 boulder was derived is poorly known and the calculations of heat flow from the melt sheet to the surroundings are largely intended to show the effect of varying the boundary conditions rather than precisely

determining the cooling history of this boulder.

The melt sheet was assumed to be 10 m thick and the initial temperature was taken as 1500 K, a representative value for the uniform temperature at the end of first-stage cooling that is below the liquidus temperature to account for the preservation of observed clasts in the melt.

The country rock beneath the melt sheet was taken as cold (initially 273°K) material with the same thermal properties as the melt sheet. In all cases, the lower boundary condition was the same: at 30 m below the lower edge of the melt, the temperature was taken as constant at 273°K for all times. For the range of times covered by the calculations, the use of this condition with a cold region 30 m in thickness is equivalent to an infinite body below the cooling melt sheet.

The melt sheet from which the boulder is derived is now covered with more than a kilometer of debris. It is not known, however, how much of this material covered the sheet at the time of emplacement. Three different types of boundary conditions above the melt sheet were therefore considered in the calculations:

(1) The melt sheet is covered with a cold blanket identical to the insulating layer (30 m thick) beneath it. Since the melt sheet and surroundings are symmetrical about the center of the sheet for this case, the heat flow problem was solved for only one half of its thickness. If  $Y$  is the thickness of the slab (10m) and  $X = 0$  is the center of the melt sheet, the boundary conditions are:

$$\frac{\partial T(0,t)}{\partial X} = 0; \text{ i.e., no heat flow across the center of the sheet} \quad (\text{VII-6a})$$

$$T(3.5Y,t) = 273^\circ\text{K} \quad (\text{VII-6b})$$

For the time scale covered by the calculations, this boundary condition is equivalent to a very thick layer of debris on top of the melt sheet.

(2) The melt sheet represents a surface flow with no insulating layer above it. The melt then cools by conduction into the cold region below and by radiation into space on top. If  $X = 0$  is the top surface of the melt, the boundary conditions for this case are:

$$T(4Y,t) = 273^\circ\text{K} \quad (\text{VII-7a})$$

$$k_{TH} \frac{\partial T(0,t)}{\partial X} = \sigma \epsilon T^4(0,t) \quad (\text{VII-7b})$$

Here  $\epsilon$  is the emissivity of the melt (assumed to be 0.85) and  $\sigma$  is the Stephan-Boltzman constant.

(3) There is a thin, cold (initially  $273^\circ\text{K}$ ) insulating layer on top of the melt sheet, such as would be expected if debris from the impact event immediately fell on top of the melt sheet. If  $X = 0$  is the top surface of the insulating layer above the melt sheet,  $Y$  is the thickness of the melt sheet, and  $Z$  is thickness of the upper insulating layer, the boundary conditions for this case are:

$$T(Z + 4Y,t) = 273^\circ\text{K} \quad (\text{VII-8a})$$

$$k_{TH} \frac{\partial T(0,t)}{\partial X} = \sigma \epsilon T^4(0,t) \quad (\text{VII-8b})$$

Upper insulating blankets of 1 and 5 m were used to explore this boundary condition. These are thin enough that conduction through them



and radiation from the top surface into space is appreciable.

For Manicouagan, only one type of boundary condition was considered. The melt sheet was assumed to be 200 m thick with a 600 m insulating layer initially at 273 K below it and an identical cold blanket above it. It was assumed that at 600 m from the edge of the melt the temperature is constant. This is the same as for the first type of boundary condition considered for the lunar example. The boundary conditions were eqn. (VII-6) with  $Y = 200$  m. The initial melt temperature was taken as 1500 K, which is above the liquidus of the melt. Besides a uniform temperature in the melt, an initial gradient from 1400 K at the melt sheet-basement interface to 1600 K at the melt sheet-cold blanket interface was considered. In other calculations, the effect of a "warm" (400 C) blanket was also investigated. In both cases, the results were not significantly different from those presented here.

Boundary conditions which included radiation at the surface, either with or without an insulating blanket, were applied; but this resulted in instabilities in the solution to the heat flow equation. (The large time intervals in the solution of the difference equation required to cool the bulk were not compatible with the high cooling rate at the surface due to radiation.)

The calculations for second-stage cooling were used to provide information about the cooling rates at different temperatures and various locations in the melt sheet, as well as the time required for various parts of the sheet to cool to selected temperatures of interest.

## B. Results

### 1. First-stage cooling

Over much of the temperature range covered by first-stage cooling, the average temperature of the melt-clast mixture is found to vary approximately logarithmically with time. An example of this behavior for Manicouagan with  $V_{\text{initial}} = 0.41$  and  $T_{\text{initial}} = 1600\text{C}$  is shown in Fig. VII-1. The average temperature of the melt decreases by more than 400 C in ten seconds. Thereafter, the cooling rate decreases substantially. After about 500 seconds, the average temperature of the melt has essentially reached its final value. The melt-clast mixture is, however, far from equilibrium, with the temperature in the mixture ranging over some 100 C. Final thermal equilibrium for the first-stage cooling of Manicouagan is reached only after 6000 to 10,000 seconds.

The initial cooling in the Station 6 Boulder is much faster due to the presence of very small clasts. In a typical case, the change in average melt temperature reaches 90% of its final value within about 1 sec, which marks the end of logarithmic cooling. Thereafter, the cooling rate decreases considerably; and final thermal equilibrium occurs after about 100 sec.

The rapid, approximately logarithmic, initial decrease in temperature is associated with heat flow to local sinks (the clasts), and the time scale is determined by the sizes of the clasts and the distances between them, and hence by the spatial distribution of clasts in the melt. The time for final thermal equilibrium is independent of the initial volume fraction of clasts and of the initial temperature of

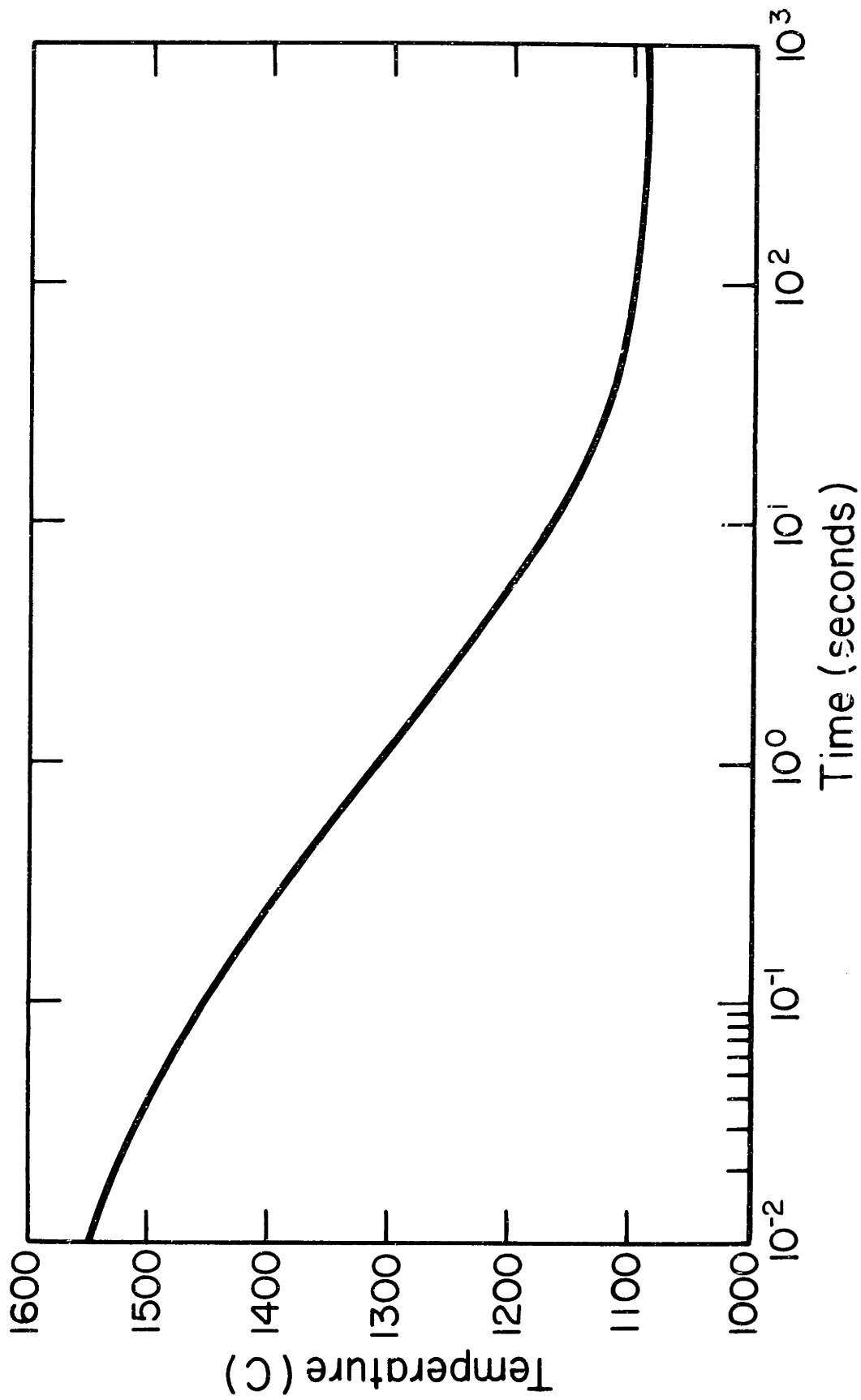


Figure VII-1 - Mean temperature of melt. Initial temperature of melt = 1600 C. Initial volume fraction of clasts = 0.41.

the melt, but does depend upon the spatial distribution of clasts in the melt. The time for final equilibration should increase as the square of the scale of the thermal inhomogeneity.

As shown in Fig. VII-2 in more detail, increasing the volume fraction of clasts initially present decreases the mean temperature of the melt at any time. It does not, however, change the time necessary for the melt to reach its final mean temperature. At a given volume fraction of clasts, decreasing the average clast size will decrease the average melt temperature at short times, and will decrease the time to reach the final mean temperature. Not only does the mean temperature of the melt decrease more rapidly with the presence of many small clasts, but also the temperature range in the melt-clast mixture is also reduced more rapidly. As would be expected, the smaller clasts melt much sooner than large clasts.

The final volume fraction of clasts in the melt (after the first-stage cooling of the Station 6 Boulder is complete) varies with the initial melt temperature and initial fraction of clasts as shown in Fig. VII-3. In this case it was assumed that all clasts are of the same type and they melt only when the liquidus of the melt is reached. The final clast content is a function of three parameters: the initial melt temperature, the initial volume fraction of clasts, and the distribution of clast sizes. As shown in the figure, regions can be defined where various final clast contents are expected.

The detailed locations of these regions depend on the average size and distribution of sizes of the clasts initially present in the melt.

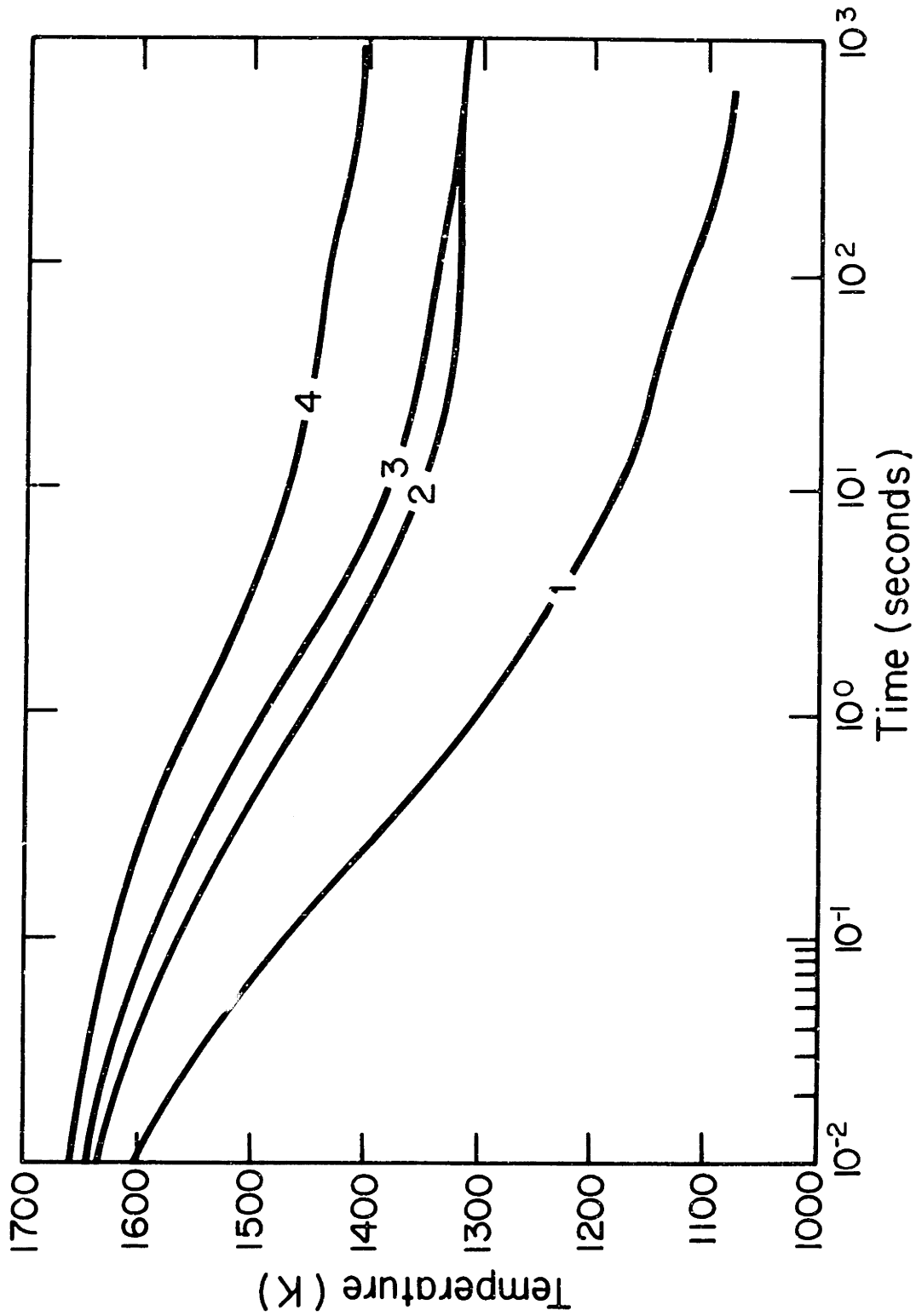


Figure VII-2 - Mean temperature of melt. Initial temperature of melt = 1427 C. Initial volume fraction of clasts: (1) 0.61 (mean size = 1.94 mm); (2) 0.41 (mean size = 1.54 mm); (3) 0.40 (mean size = 1.97 mm); (4) 0.23 (mean size = 1.80 mm).

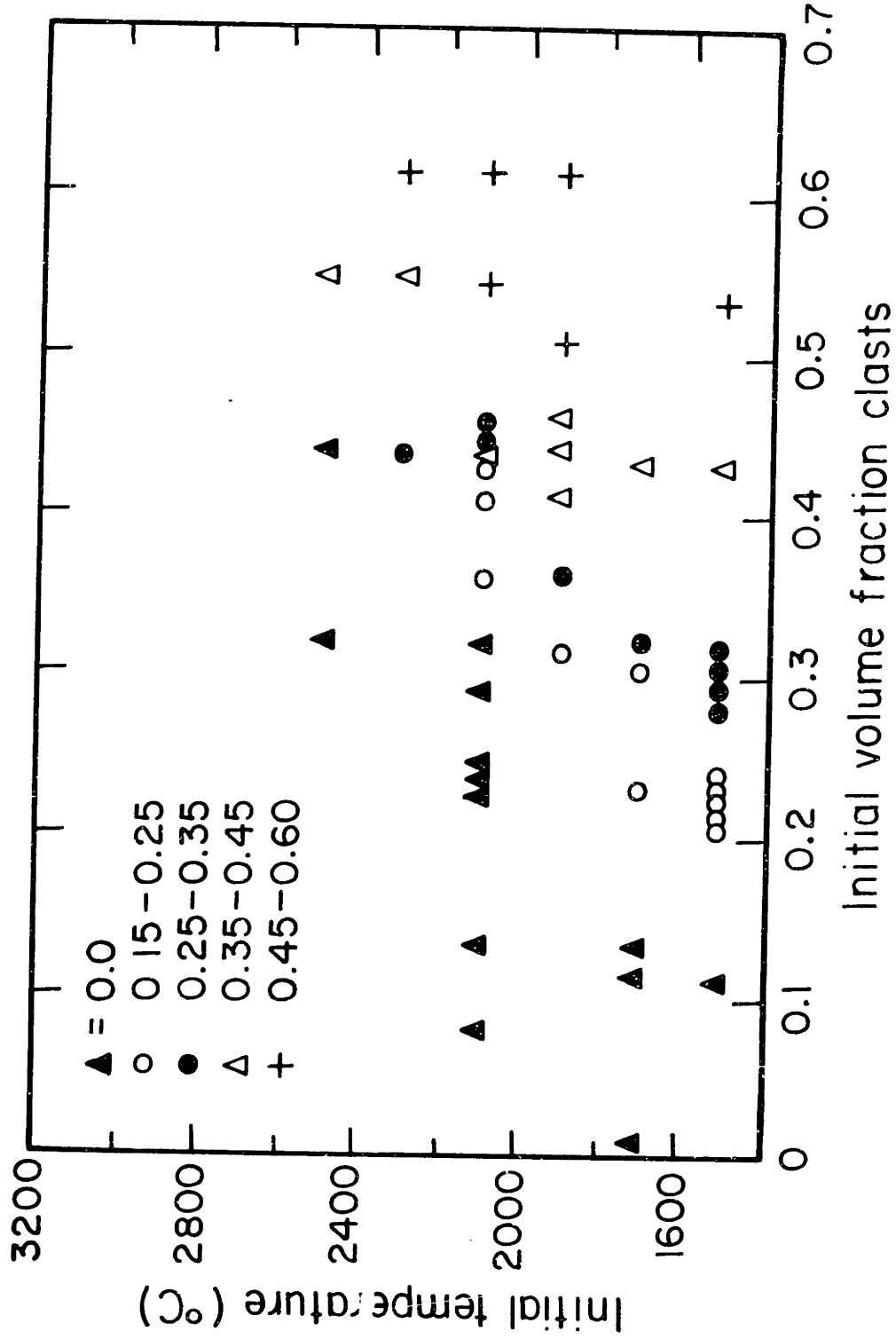


Figure VII-3 - Final volume fraction of clasts after first-stage cooling as a function of initial temperature and initial volume fraction of clasts.

For example, if the melt is initially superheated by as little as 200°C, small isolated clasts will melt (see Fig. VII-4). If, however, a small clast is located near a large clast, it will not melt unless the superheat of the melt is sufficient that the large clast also starts to melt. Some isolated clasts, even if they do not melt, are often raised to quite high temperatures. During first-stage cooling, the average clast size generally increases. Although the clasts do not grow, the small ones disappear completely while the larger ones become only slightly smaller by partial melting.

An examination of the extent of clast digestion predicted for Manicouagan yields similar results. Many clasts are partially melted at the end of first-stage cooling because their edges are raised to temperatures above the liquidus. Small isolated clasts, even of the most refractory type, tend to be digested. Those located near large clasts are preserved as long as the large clasts are not raised to a temperature such that the small clasts can melt. This preferential melting of small clasts again results in an increase in the average clast size. Considering only clasts that have melted completely due to being raised to a temperature greater than their liquidus, this effect may be illustrated by the following results.

For a melt with an initial temperature of 1400C, a mixture containing 41% clasts with a mean initial size of 154  $\mu\text{m}$  becomes after equilibration a mixture of 30% clasts with a mean size of 180  $\mu\text{m}$ . At the higher initial temperature there is more digestion of large clasts than at the lower temperature, and hence the increase in mean clast size is smaller.

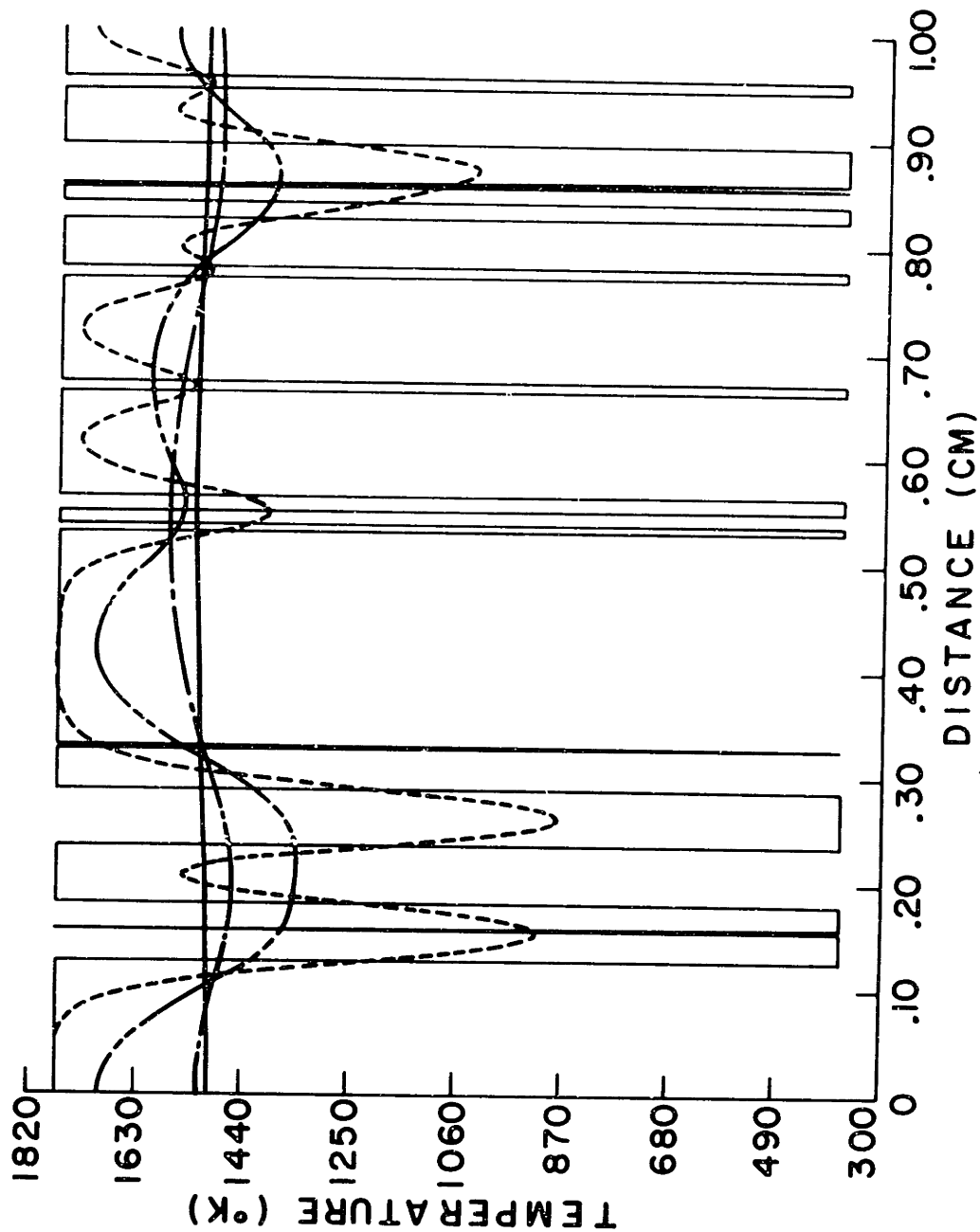


Figure VII-4 - Temperature vs. distance in a representative 1 cm section in melt-clast system. Initial volume fraction of clasts = 0.21. Final volume of clasts = 0.19. Initial temperature = 1773 K. Equilibrium temperature = 1518 K. Times: \_\_\_\_\_ 0.0 sec; ---- 0.07 sec; --- 0.6 sec; — - 5.0 sec; ——— 30 sec.



Table VII-1 shows for Manicouagan, the extent of clast digestion due to (A) only heating above the liquidus of the clast; and (B) heating above the liquidus of the clasts plus partial melting due to heating above the solidus. The initial melt temperature was taken as 1300C. The calculations for an initial volume fraction of clasts of 0.235 shown in Table VII-1 assumed a distribution of clast types as follows: type 1 - 17%; type 2 - 30%; type 3 - 40%; and type 4 - 13%. Further calculations with an initial melt temperature of 1300C and an initial clast content of 0.243 were carried out with a high proportion of refractory clasts (type 1 - 49%; type 2 - 42.8%; type 3 - 3.7%; and type 4 - 4.5%) with the same melting ranges as assumed previously. In this case, the equilibration temperature is 1102 C or 14C higher than in the case with a more even distribution of clast types. The volume fraction of clasts remaining after melting due to clasts being raised above their liquidus is 0.217 or 3 times that shown in Table VII-1. After melting due to clasts being raised to a temperature between their liquidus and solidus, the volume fraction remaining was 0.154 or more than twice that in Table VII-1.

If the proportions of clast types are inverted (type 1 - 4.5%; type 2 - 3.7%; type 3 - 42.8%; and type 4 - 49%) to consider a high proportion of low melting clasts, the equilibration temperature is reduced to 1072 C and the volume fractions of clasts remaining after the two types of melting are 0.03 and 0.01. Thus a high proportion of low-melting clasts results in more melting of clasts, thereby absorbing more heat from the melt and lowering the equilibration temperature.

Table VII-1Clast Digestion in Manicouagan

<u>V<sub>Initial</sub></u>	<u>A</u>	<u>V<sub>final</sub></u> <u>B</u>	<u>T<sub>initial</sub></u> <u>(°C)</u>	<u>T<sub>final</sub></u> <u>(°C)</u>
0.235	0.074	0.072	1300	1088
	0.074	0.038	1400	1110
	0.0	0.0	1500	1171
	0.0	0.0	1600	1217
0.409	0.328	0.296	1300	1023
	0.30	0.257	1400	1040
	0.185	0.15	1600	1083
	0.126	0.085	1800	1105
0.608	0.599	0.57	1400	826
	0.55	0.54	1600	903
	0.543	0.529	1700	952
	0.54	0.49	1800	1009
	0.369	0.222	2000	1074

## 2. Second Stage Cooling:

Table VII-2 shows the effect of different boundary conditions on the cooling of a 10 m thick slab from an initial temperature of 1500K. The cooling rate is seen to be a complicated function of time, location, and boundary conditions. For example, Fig. VII-5 shows the temperature as a function of time for various locations in the melt for the case when the melt sheet is covered by a 1m cold blanket. Fig. VII-6 shows the temperature as a function of position in the melt sheet for the three boundary conditions treated.

There is significant heating of the insulating layer beneath the melt sheet, but the assumption that the insulating layer is 3 times the thickness of the melt sheet or 30 m thick is reasonable: the characteristic distance for heat flow in  $10^8$  sec is approximately

$$\chi \approx (D_{TH} t)^{1/2} = 6.3\text{m} \quad (\text{VII-5})$$

Therefore a 30m insulating layer has the same effect as an infinitely thick insulating layer.

The temperature of 1300°K was chosen for particular attention, since it approximates the temperature at the end of crystallization. At lower temperatures, grain growth and solid state phase changes can still contribute to changes in morphology. Considering as a group all three sets of boundary conditions on the 10 m melt sheet, crystallization should be complete throughout the sheet in 0.6-1.1 yr. The top surface of the melt sheet crystallizes in 1.9-2.6 days, save in the case of radiation directly from the top of the sheet, where the surface crystallizes in only 24 min. The presence of only 1m of insulating material

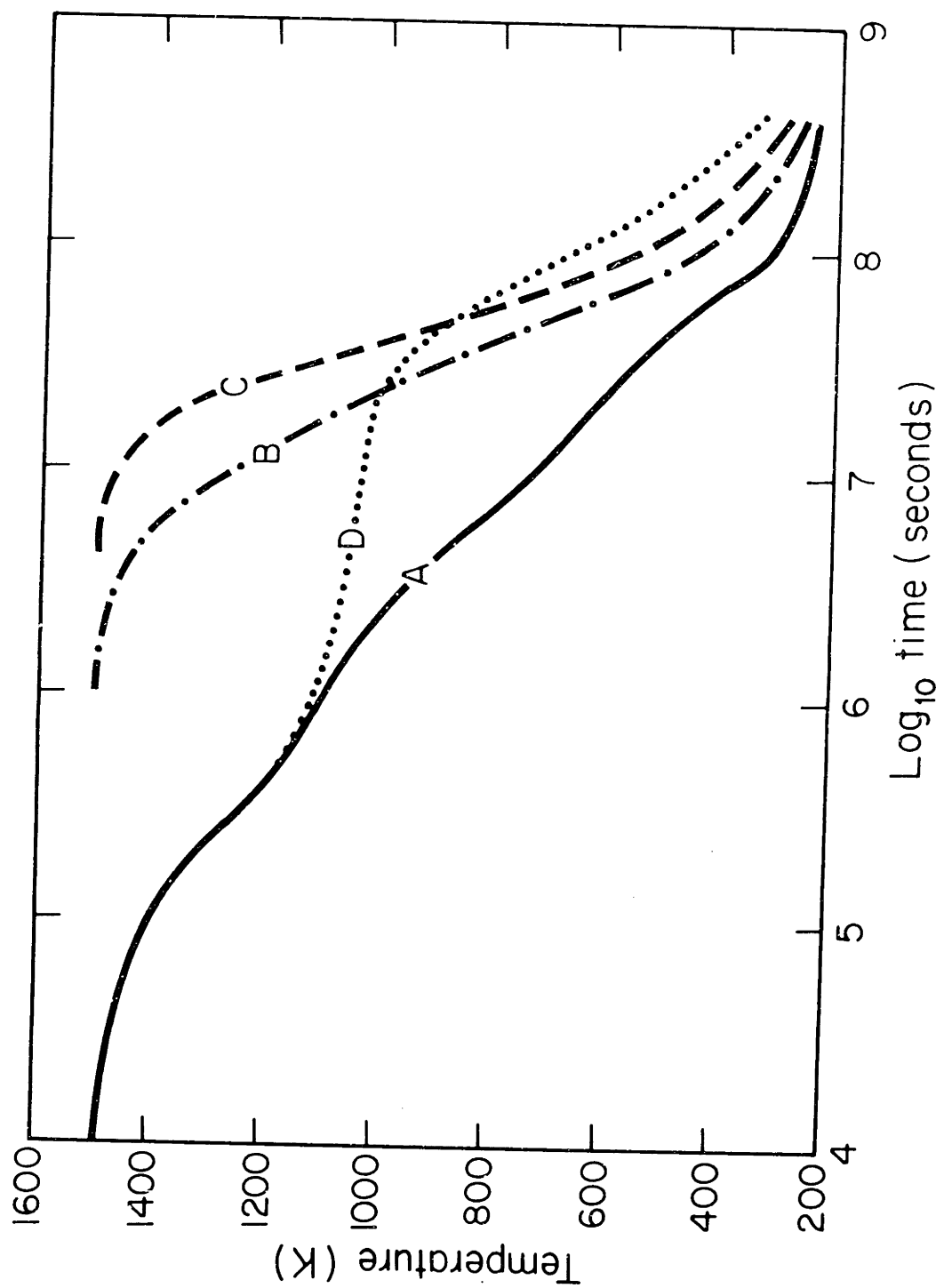


Figure VII-5 - Variation of temperature with time for various locations in a 10 m melt sheet covered by 1 m cold blanket on top. Distances measured from the boundary between melt sheet and cold blanket on top. A = at boundary; B = 2.5 m from boundary; C = 5 m from boundary; D = 10 m from boundary.

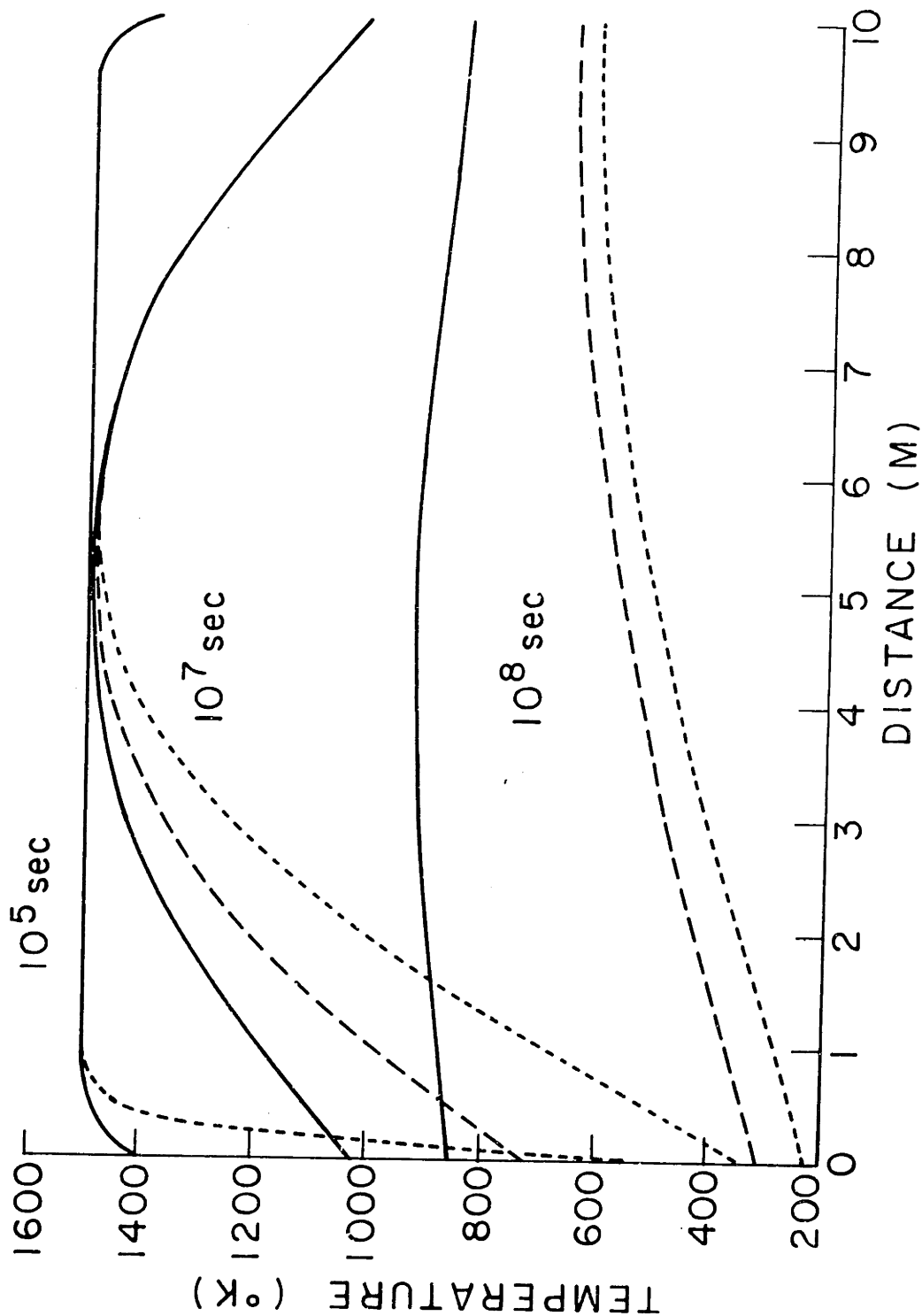


Figure VII-6 - Temperature profiles through a 10 m melt sheet for 3 sets of boundary conditions at times of  $10^5$ ,  $10^7$ , and  $10^8$  sec. In all cases, a 30 m cold basement is taken below the melt;  $\cdots$  = 30 m cold blanket above sheet;  $\text{—}$  = 1 m cold blanket above sheet and radiation from top surface of blanket;  $\text{---}$  = radiation directly from top surface of melt.

Table VII-2

Cooling of 10 m Sheet from 1500°K

Temperature	Location	Instantaneous cooling rate	Time to cool to temperature
(a) Insulated on both sides			
1300°K	Center	1.0°K day <sup>-1</sup>	1.1 year
	Edge	78.5°K day <sup>-1</sup>	2.0 days
1200°K	Center	0.73°K day <sup>-1</sup>	1.4 year
	Edge	33.8°K day <sup>-1</sup>	4.2 days
1100°K	Center	0.57°K day <sup>-1</sup>	1.9 year
	Edge	6.0°K day <sup>-1</sup>	10.6 days
1000°K	Center	0.38°K day <sup>-1</sup>	2.5 year
	Edge	0.18°K day <sup>-1</sup>	0.95 year
900°K	Center	0.13°K day <sup>-1</sup>	3.5 year
	Edge	0.19°K day <sup>-1</sup>	2.4 year
(b) Radiation from top of melt			
1300°K	Top	0.14°K sec <sup>-1</sup>	24 min.
	Center	1.57°K day <sup>-1</sup>	0.63 year
1200°K	Top	0.13°K sec <sup>-1</sup>	38 min.
	Center	1.8°K day <sup>-1</sup>	0.76 year
1100°K	Top	0.09°K sec <sup>-1</sup>	53 min.
	Center	1.8°K day <sup>-1</sup>	0.92 year
1000°K	Top	0.07°K sec <sup>-1</sup>	72 min.
	Center	1.3°K day <sup>-1</sup>	1.1 year
900°K	Top	0.04°K sec <sup>-1</sup>	105 min.
	Center	0.96°K day <sup>-1</sup>	1.4 year

Table VII-2 (Cont'd)

Temperature	Location	Instantaneous cooling rate	Time to cool to temperature
(c) 1 m cold blanket on top, radiation from its surface			
1300°K	Top	67.1°K day <sup>-1</sup>	2.4 days
	Center	1.8°K day <sup>-1</sup>	0.70 year
1200°K	Top	40.0°K day <sup>-1</sup>	4.5 days
	Center	1.8°K day <sup>-1</sup>	0.86 year
1100°K	Top	9.8°K day <sup>-1</sup>	11 days
	Center	1.3°K day <sup>-1</sup>	1.0 year
1000°K	Top	5.3°K day <sup>-1</sup>	27 days
	Center	1.3°K day <sup>-1</sup>	1.3 year
900°K	Top	3.6°K day <sup>-1</sup>	49 days
	Center	1.0°K day <sup>-1</sup>	1.5 year
(d) 5 m cold blanket on top, radiation from its surface			
1300°K	Top	67.0°K day <sup>-1</sup>	2.9 days
	Center	1.0°K day <sup>-1</sup>	0.92 year
1200°K	Top	26.7°K day <sup>-1</sup>	4.7 days
	Center	1.1°K day <sup>-1</sup>	1.1 year
1100°K	Top	2.9°K day <sup>-1</sup>	17 days
	Center	0.83°K day <sup>-1</sup>	1.5 year
1000°K	Top	0.31°K day <sup>-1</sup>	0.51 year
	Center	0.67°K day <sup>-1</sup>	1.8 year
900°K	Top	0.50°K day <sup>-1</sup>	1.2 year
	Center	0.30°K day <sup>-1</sup>	2.3 year

on top of the melt sheet is enough to slow the cooling rates to a range similar to those expected for a thick insulating blanket on top. For all three sets of boundary conditions, the cooling rates near the bottom of the melt sheet are closely similar.

Table VII-3 shows the time required for various positions in a 200m. thick melt sheet such as Manicouagan to cool from 1500 K to several lower temperatures. There is significant heating of the insulating layer surrounding the melt sheet; the characteristic distance for heat flow in 3200 years is approximately 200 m. Crystallization should be complete throughout the sheet in about 1600 years. The outer 3.5 m. should crystallize in about 6.6 years.

### C. Discussion

#### 1. First-Stage Cooling:

A model has been proposed to describe the thermal history of impact melts such as the Apollo 17 Station 6 Boulder and Manicouagan. The sheets are described as a complex silicate melts mixed with cold clasts. The clasts very quickly absorb heat from the melt. The short times required for the melt-clast mixture to reach a uniform temperature suggest that division of the cooling process into two separate stages, with quite different characteristic times, is highly realistic.

According to the results of Carslaw and Jaeger (36) the time for thermal equilibration of a melt-particle system increases somewhat as the volume fraction of particles decreases. In contrast, the present results indicate an equilibration time which varies only slightly if at



Table VII-3

Time Required to Cool to Various Temperatures  
for 200 M Melt Sheet

T (°C)	$\rho C_p (T)$	Jaeger	
		$K = 0.004 \text{ cm}^2 \text{ sec}^{-1}$	$K = 0.004 \text{ cm}^2 \text{ sec}^{-1}$
		$\rho C_p = 1 \text{ cal cm}^{-3} \text{ } ^\circ\text{K}^{-1}$	$\rho C_p = 1 \text{ cal cm}^{-3} \text{ } ^\circ\text{K}^{-1}$
<u>A. at 10.5 m. from boundary</u>			
1027	35 years	17 years	18 years
927	86 years	32 years	34 years
827	350 years	85 years	70 years
727	2200 years	320 years	320 years
627	3900 years	1800 years	1600 years
<u>B. at center of melt sheet</u>			
1027	1600 years	950 years	82 years
927	2100 years	1400 years	1200 years
827	2750 years	1900 years	1650 years
727	3800 years	2700 years	2300 years
627	5300 years	3900 years	3300 years

all with volume fraction of clasts. The difference between the two results is associated with the random distribution of clasts of various sizes used here vs. a single particle in a melt of various heat capacities (in various amounts of melt).

For a given volume fraction of melt, Carslaw and Jaeger (36) found the time for thermal equilibration increases as the square of the particle diameter. A similar result was found in the present work, when mean particle sizes are compared (for similar distributions of sizes). The times required for the melt temperature to reach 90% of its final value are shorter by a factor of 3-10 for the Carslaw and Jaeger treatment than for the present results. This difference is likely associated in large part with the assumption of an infinite thermal conductivity used previously vs. the finite value used here, and also with the use of spherical geometry in the previous calculations vs. the one-dimensional model used here.

Essential to the present results is the assumption that the 1 cm region of the melt containing small clasts can be taken as representative of the melt-clast mixture as a whole. This assumption should be valid provided the cooling behavior is not dominated by a few large clasts which fall beyond the distribution used in the calculations--and even in that case, the effects of the large clasts should be most pronounced in the final portion of first-stage cooling (as the uniform temperature is approached), and should be rather minimal in the initial portion of most rapid temperature drop (logarithmic cooling).

Comparing the results presented here with those of the simplified model suggested by Simonds et al. (35) indicate several notable differences (Fig. VII-7). The previous work assumed a linear relation between the equilibrium temperature and the fraction of clasts melted, and also assumed that all clast digestion takes place after equilibration. At an equilibrium temperature which is at a given fraction of the difference between the liquidus and the solidus of the melt, the model which includes only melting due to clasts being raised above the liquidus of the melt indicates a lesser degree of clast digestion than Simonds' model; that model, in turn, indicates less clast digestion than the model which includes four types of clasts with discrete melting points. When the equilibrium temperature is below the solidus of the melt, Simonds' model indicates no clast digestion but the other models indicate that some clast digestion is possible. If partial melting due to temperatures above the solidus is taken into account, the difference between the Manicouagan model presented here and the other two models is even greater. This difference results from clasts, particularly isolated clasts, reaching temperatures considerably above the equilibrium temperature and melting. Chemical equilibrium may not be achieved in the short equilibrium times, but at least partial melting and perhaps zoning should be evident.

A weak tendency for clast size to increase with decreasing volume fraction of clasts and increased fraction of refractory plagioclase is observed in Manicouagan by Simonds et al. (97), in accord with the predictions of these calculations.

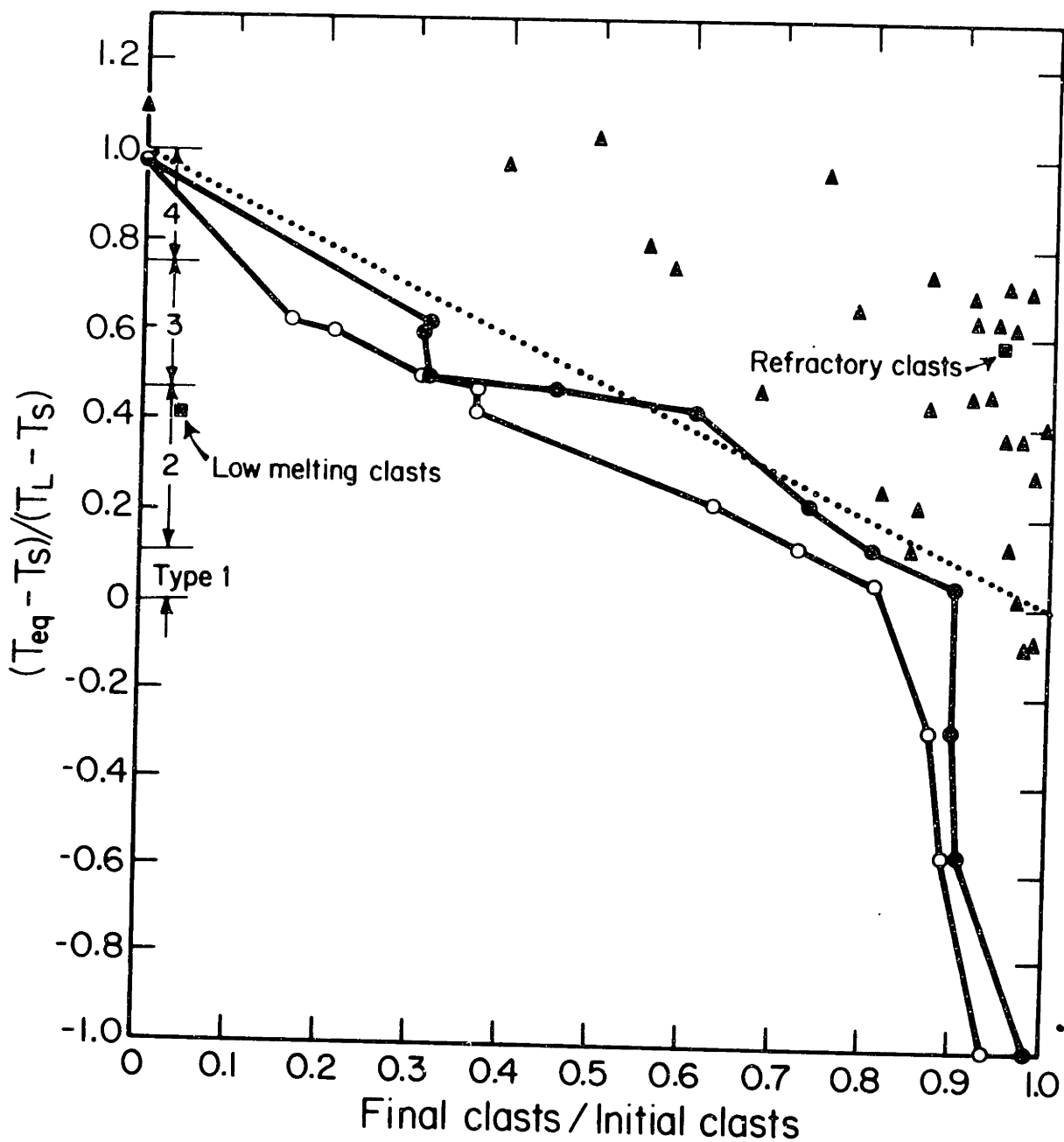


Figure VII-7 - Equilibrium temperature as a function of fractional clast digestion. Dotted line - Simonds (35); triangles - assuming clasts melt only at liquidus of melt; solid circles - assuming 4 types of clasts melting at 4 distinct liquidus temperatures only; open circles - assuming 4 types of clasts, melting at 4 liquidus temperatures plus partial melting above solidus temperatures.

The equilibrium temperature determined by Simonds' (35) method of energy balance between clasts and melt is similar to that determined by the method presented here for Manicouagan, although the calculations of Simonds showed overestimate temperatures by about 10C because of the underestimate of melting.

The model presented here for the Station 6 Boulder underestimates the extent of clast digestion, which should be much more reliably represented by the model for Manicouagan. If anything, the latter results will overestimate the extent of clast digestion in systems where the process of digestion is limited by mass transport rather than by heat flow. In most systems of interest, however, the long times required for final temperature equilibration suggest that the Manicouagan model should provide useful estimates of clast digestion even in kinetically-sluggish systems. In systems with small clasts, such as the Station 6 Boulder, the time to reach thermal equilibrium will be smaller, but then the melting of small clasts would not have the kinetic problems associated with the melting of large clasts.

## 2. Second State Cooling

According to Jaeger (39), near the boundaries between the melt and the insulating layers, the distance of an isotherm from the boundary is proportional to  $t^{1/2}$ . Hence the mean cooling rate at a given temperature, defined as the temperature range through which a point cools divided by the time it takes to cool through this range, is proportional to  $Y^{-2}$ , where  $Y$  is the distance from the boundary. The solutions determined in this paper for the doubly insulated melt sheet show this dependence only

over a limited range of temperature and distances from the boundary. At 1023C, for example, departures from the  $Y^{-2}$  dependence are seen for distances from the p boundary greater than about 2.5 m for the 10 m melt sheet and 50 m for the 200 m melt sheet (Fig. VII-8).

Such departures from the  $Y^{-2}$  dependence are expected whenever the finite extent of the cooling body becomes significant (the  $Y^{-2}$  dependence is strictly valid only for a body which is large relative to the scale of thermal diffusion). In the present case, the temperature of the center of the melt sheet departs from the initial temperature only when the 1027C isotherm is about 2.5 m from the boundary of a 10 m slab and 50 m from the boundary of a 200 m slab. At greater distances from the boundary, the time required to cool to 1027C is smaller than predicted by the  $Y^2$  dependence. As shown in Fig. VII-8 the location of the 927C and 827C isotherms also follows the  $Y^2$  dependence to some distance from the boundary. In a 200 m thick melt sheet the 927C isotherm follows the  $Y^2$  dependence to about 35 m from the edge and the 827 C isotherm follows the  $Y^2$  dependence to about 15 m from the edge. The 727 C and 627 C isotherms do not follow this dependence even for short times.

The instantaneous cooling rate at 1027 K, i.e., the rate at which a particular location in the melt cools through a given temperature--is found to be proportional to  $Y^{-2}$ , at least for the region in which the finite extent of the melt sheet is not important. Jaeger (39) did not consider this cooling rate. In the region where the finite extent of the melt sheet is important, the instantaneous cooling rate in our calculations remained approximately constant through the range of 1027C. As

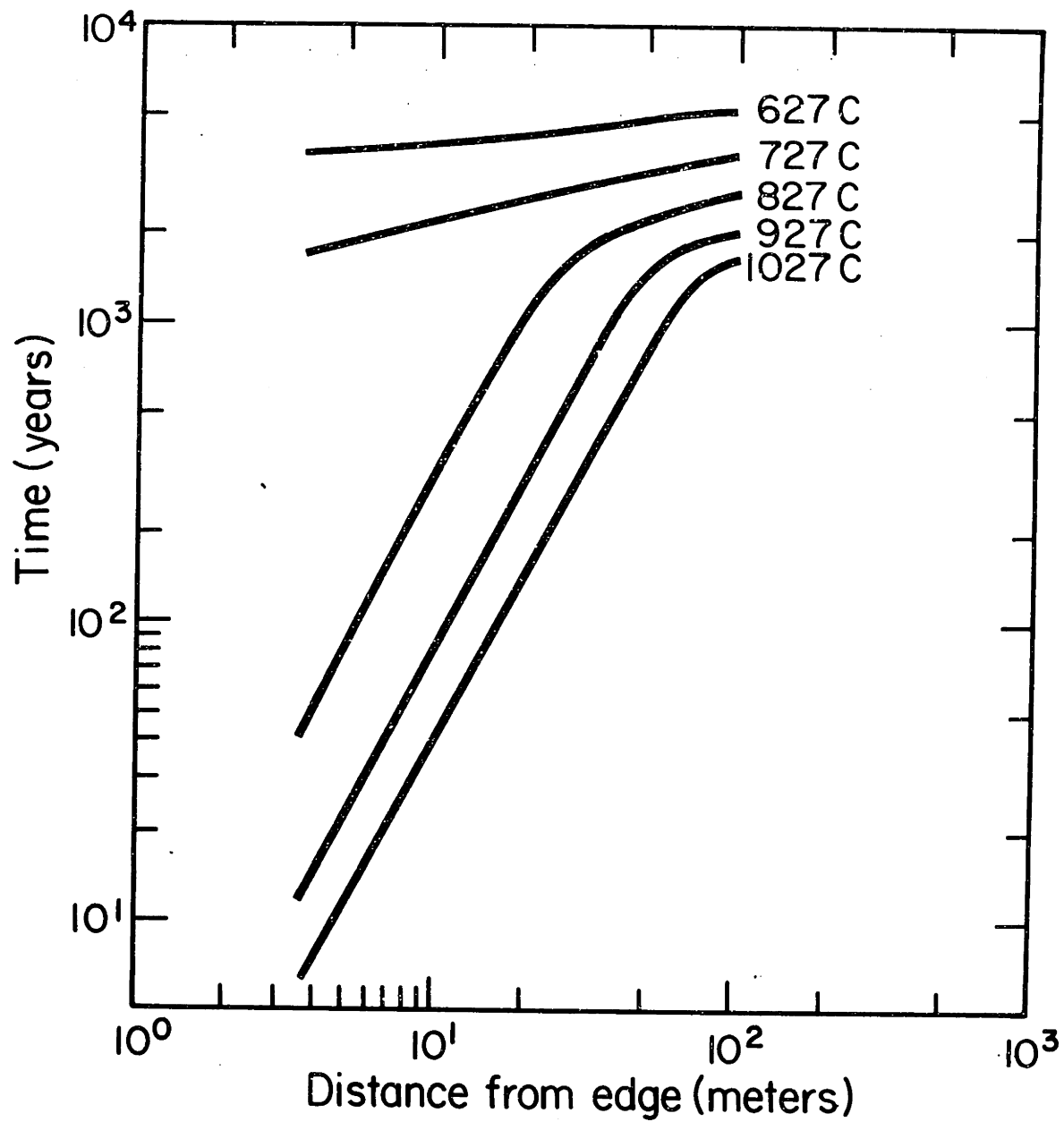


Figure VII-8 - Time required for penetration of isotherms into 200 m melt sheet as a function of distance from edge.

cooling proceeds, the differences in cooling rate at different locations decrease until at 627 C the instantaneous cooling rate varies by only a factor of about 2 over the entire melt sheet. For example, in a 200 cm thick melt sheet at 1027C the instantaneous cooling rate 3.5 m from the edge is  $0.45^\circ/\text{sec}$  while that at locations greater than 60 m from the edge is about  $3 \times 10^{-3}^\circ\text{C}/\text{sec}$ . At 627C, the instantaneous cooling rate 3.5 m from the edge is  $3.4 \times 10^{-4}^\circ\text{C}/\text{sec}$  while that at distances greater than 45 m from the edge is about  $7.5 \times 10^{-4}^\circ\text{C}/\text{sec}$ . Since the melt sheet has been divided into finite increments in order to solve the heat flow equation, the solution at 3.5 m from the edge is the closest possible to that at the interface.

To evaluate the effects of latent heat and to compare different methods of analysis, the heat flow calculations for the second stage cooling of Manicouagan were done both with and without consideration of the temperature dependence of the heat capacity and latent heat. In Table VII-3, these results are compared with the analytical treatment of Jaeger (39) assuming a constant heat capacity such that  $\rho C_p = 1 \text{ cal cm}^{-3} \text{ K}^{-1}$ . At short times, when latent heat is ignored the present numerical calculations agree very well with the analytical solution of Jaeger. The temperature at the interface drops immediately to  $(T_0 + T_\infty)/2$  or 613 C and remains there for about 32 years, when the center of the melt starts to cool. The temperature of the surroundings never goes above this temperature. When latent heat is included, however, the country rock at 3.5 m from the edge of the melt sheet is raised to a maximum temperature of 700 C in about 1360 years. Including the latent heat in an effective



heat capacity in the melting range reduces the thermal diffusivity from about 0.0048 to about 0.0018 cm<sup>2</sup>sec<sup>-1</sup> ( $C_p \approx 0.19$  cal gm<sup>-1</sup>K<sup>-1</sup>). This results in an increase in the time required to cool to a given temperature compared to that required when latent heat is not included. When the center of the melt sheet starts to cool the analytical results of Jaeger do not agree well with the present numerical results obtained using a constant heat capacity. This difference is associated with the finite nature of the melt sheet considered in the present work relative to the infinite sheet described in Jaeger's analytical work.

The calculations of heat flow in Manicouagan were done with only one set of boundary conditions. However, the results for the lunar case show the importance of the boundary conditions on the time required to cool to a given temperature (Table VII-2). A melt sheet which is allowed to cool by radiation cools much faster than a well-insulated melt sheet, particularly at the upper surface.

Provost and Bottinga (40) derived an expression for the velocity at which the upper crust (near the radiating boundary) grows:

$$\frac{Y}{t} \propto Y^{-0.89} \quad \text{or} \quad Y \propto t^{0.53} \quad (\text{VII-9})$$

where Y is the thickness of the upper crust (the distance from the upper boundary). This expression is in close agreement with the present results for cooling through the range of 1023 C for the case of radiation from the top surface of the melt. In the present work, it was found that  $Y \propto t^{0.52}$  for the top 4 m of the melt sheet.

Correspondingly, the time required for cooling to 1023C for locations within the top 4 m varies as  $Y^{1.92}$ . These numerical results for cooling with a radiation boundary condition are close to the  $t^{1/2}$  and  $Y^2$  dependences expected for the doubly-insulated case when the finite extent of the melt is not significant. In the present case, with radiation from the top surface, the finite extent of the melt is apparent when the 1023 C isotherm is about 2 m from the top surface; yet the  $t^{0.52}$  and  $Y^{1.92}$  dependences continue to be followed to a distance from the surface of 4 m. At distances greater than 4 m from the surface, the time to cool to 1023 C increases less rapidly than predicted by the  $Y^2$  dependence. The point which takes the largest time to reach 1023 C (0.63 year) is located about 6 m from the surface. With greater distances from the surface, the time to cool to 1023 C decreases and approaches values similar to those obtained for the doubly-insulated case as the lower boundary (with the basement layer) is approached.

For the case of radiation from the top surface of the melt, the instantaneous cooling rate at 1023 C is very high near that surface (see Table VII-1), and decreases rapidly with distance into the melt until at the center it is nearly 4 orders of magnitude lower than at the top surface. The cooling rate continues to decrease with distance from the top surface until a minimum of  $1^\circ\text{C day}^{-1}$  reached at 7.5 m from the surface. Then it increases again to rates similar to those calculated for the doubly-insulated case [case (1)] due to cooling to the basement.

At 623 C, by which temperature most transformations have ceased, cooling continues very much in the same manner as at 1023 C. The surface

cools quite quickly ( $0.04^{\circ}\text{K sec}^{-1}$  at  $623\text{C}$ ) compared with the center of the melt (where it is about  $0.96^{\circ}\text{K day}^{-1}$  at  $623\text{C}$ ). The  $Y^{-2}$  dependence of instantaneous cooling rate on distance from the surface holds to 2.5 m from the surface. Then it is approximately constant at about  $1^{\circ}\text{C day}^{-1}$  to about 6 m from the surface, beyond which it decreases further to about  $0.48^{\circ}\text{K day}^{-1}$  at the lower boundary.

The time required to cool to  $900^{\circ}\text{K}$  varies with distance from the surfaces in the same way (following the  $Y^2$  dependence) as the time required to reach  $1023\text{C}$ . At  $623\text{C}$ , this relation holds to about 3 m from the surface. Thereafter, as before, the cooling times are smaller than predicted by the  $Y^2$  relation. This type of cooling causes the temperature maximum to shift toward the lower boundary with longer times and lower temperatures. A maximum of  $623\text{C}$  occurs at about 7.5 m from the upper surface in about 1.5 years. The cooling behavior with a radiation boundary condition on the top surface of the melt is thus quite different from that for the doubly-insulated case. In the latter case, the cooling rate at  $623\text{C}$  and the total time required to reach  $623\text{C}$  are not strongly dependent on position in the melt sheet; whereas for the radiation boundary condition, significant variations in cooling rate and time to cool are still observed at  $623\text{C}$ .

As shown in Fig. VII-6, when there is a 1 m thick insulating layer on top of the melt sheet, the temperature distribution at short times ( $10^5$  sec) coincides with that for a melt sheet with thick insulation on both sides. At intermediate times ( $10^7$  sec), the temperature distribution near the top surface is intermediate between the former case and that

with no insulating layer on top. At depths greater than half the thickness of the melt sheet below the upper boundary, all three cases have the same temperature profile. At long times ( $10^8$  sec), the case with a thin insulating layer is similar to that with no insulating layer and the temperature maximum has shifted to the lower boundary.

#### D. Conclusions

The following conclusions may be drawn from the calculations of the present study:

(1) The cooling behavior of a clast-laden melt can usefully be modeled in terms of two distinct stages, the first involving heat flow from hot melt to cold clasts and the second involving heat flow from the melt to its surroundings.

(2) The thermal equilibration of a hot melt-cold clast system takes place quite rapidly, with equilibration times in the range of 100 sec being typical for clasts having the size distribution typical of a lunar soil (median size of 0.1 mm).

(3) During the initial portion of first-stage cooling, the average temperature of the melt-clast system decreases approximately logarithmically with time. At the end of this period of logarithmic cooling, the temperature has decreased by some 90% of the difference between the initial temperature and the final temperature, in a time which is short relative to the final equilibrium time.

(4) The time of equilibration of the melt-clast system increases as the square of the spacial heterogeneities.

(5) During equilibration of the melt-clast system, there is a preferential digestion of small clasts in the melt. This results in an increase in the mean clast size.

(6) During first-stage cooling, the heat flow process is determined not only by the volume fraction of clasts, but also by their spatial distribution. Small clasts located near large clasts are protected from digestion in the melt, save when the large clasts also start to melt.

(7) Second-stage cooling, which involves heat flow from the melt to the surroundings, takes place on a time scale which is typically larger by orders of magnitude than the time of thermal equilibration in first-stage cooling. This provides support for the division of the thermal problem into two separate problems.

(8) At short times of cooling the cooling behavior for 10 m sheets with a 1 or 5 m insulating layer above the melt sheet is similar to that for a sheet with an infinite insulating layer, while at long times the behavior with a thin insulating layer is similar to that with radiation directly from the top surface of the melt.

(9) For bodies in the size range of 10 m and initial temperature of 1500°K, the boundary condition of radiation from the top of the melt results in faster cooling than the condition of conduction to another body.

(10) For the case with radiation from the top surface of the melt, the time to cool to a given temperature increases approximately as the square of the distance from the top surface, even beyond the point where the finite extent of the melt sheet has become significant.

(11) For models with thick insulation both above and below the melt sheet, the time to cool to a given temperature increases as the square of the distance from the boundaries of the melt sheet--but only for a sufficiently limited range of temperature and distance from the boundary that the finite extent of the melt sheet is not significant.

(12) When greater ranges of temperature and time are considered, the time to cool to a given temperature increases less rapidly with distance from the boundary than the distance predicted for an infinite body.

## VIII. COOLING RATES OF ROCKS

Knowledge of the cooling rates of rocks can have both geologic and selenologic significance. Estimated cooling rates can be used to estimate the size of the parent body of a lunar rock or meteorite and the mechanism of its formation, whether it was a lava flow, impact melt, or common igneous rock. Differences in the texture, morphology and chemistry of rocks with similar bulk compositions can be attributed to differences in thermal history. In some cases, the cooling history of a rock can be simulated in the laboratory to compare the crystallization sequence and chemistry of slowly cooled and rapidly cooled rocks (41, 98, 99). When the cooling rate is very slow and simulation experiments are not feasible, there may not be any morphological differences which can be used to determine the relative and absolute cooling rates of rocks. Yet other differences do exist among rocks of varying cooling rates. The significance of these differences must be evaluated and techniques must be found to determine quantitatively the effect of thermal history on properties. Two such techniques will be presented here.

### A. The Non-Isothermal Partitioning of a Solute in a Finite Couple

The partitioning of a solute between two phases or grains in a rock is a useful indicator of the thermal history of that rock. The calculation of diffusion profiles in a finite couple is necessary to correlate measured concentration profiles and estimated cooling rates. The infinite nonisothermal problem (100) and the finite isothermal problem (101) have been solved, but in geological systems, the situation which most closely describes the temperature dependent partitioning between two phases in a

polycrystalline body is the nonisothermal finite problem.

### 1. The Model

Taylor et al. (102) have shown that partitioning is a function of temperature only, and is relatively constant for a given lunar sample. This is to be expected when (1) the activity coefficients are constant over the composition range encountered; (2) the concentration of solute in each phase is less than the solubility limit; and (3) the phase relations are not significantly affected by the solute over the composition ranges. The partition coefficient for Zr in ilmenite ( $\text{FeTiO}_3$ ) and ulvospinel ( $\text{Fe}_2\text{TiO}_4$ ) is

$$K(T) = \frac{C_1}{C_2} = 23.9 \exp \left( - \frac{3100}{T} \right) \quad (\text{VIII-1})$$

where 1 and 2 are the phases.

In the present work, it was assumed that this relation holds at the interface ( $X = 0$ ) at all times. It was also assumed that the cooling rate is constant, although any dependence of temperature on time could be used. In this case

$$T = T_0 - at \quad (\text{VIII-2})$$

Several cooling rates,  $a$ , were used and the resultant values of  $C_1/C_2$  determined.

This involves the solution of two simultaneous differential equations. The equation to be solved is the one-dimensional diffusion equation in each phase, with the diffusion coefficient a function of temperature and therefore time. That is:



$$\frac{\partial C_1(x,t)}{\partial t} = D_1[T(t)] \frac{\partial^2 C_1(x,t)}{\partial x^2} \quad (\text{VIII-3})$$

$$\frac{\partial C_2(x,t)}{\partial t} = D_2[T(t)] \frac{\partial^2 C_2(x,t)}{\partial x^2} \quad (\text{VIII-4})$$

It was assumed that the diffusion coefficient is not a function of solute concentration. These equations cannot be solved analytically because of the concentration dependence of the boundary condition at  $x = 0$ . The diffusion coefficient of Zr in coexisting ilmenite and ulvospinel has been estimated to be (44)

$$D(T) = 1.6 \times 10^{-5} \exp\left(-\frac{2.1 \times 10^4}{T}\right) \quad (\text{VIII-5})$$

It is difficult to separate the diffusivities in the two phases because the reaction will be controlled by the smaller diffusivity (103). Since the diffusion data for zirconium in each of the phases is not known, the effect of different diffusivities was investigated by assuming that either (1) the unknown diffusivity is factor of 10 greater than this experimental value, or (2) it is the same.

The effect of the solute distribution at high temperatures on the value of  $C_1/C_2$  after cooling was also explored. At one extreme, it was assumed that initially there is a uniform distribution of solute at a high temperature, such as the solidus.

$$C_1(x,0) = C_2(x,0) \quad (\text{VIII-6})$$

At the other extreme, it was assumed that at high temperatures the solute concentration is at equilibrium throughout both phases

$$C_1(x,0) = K[T(0)] C_2(x,0) \quad (\text{VIII-7})$$

In both cases, it was assumed that as the temperature was lowered the solute concentrations at the boundary are able to adjust so that the equilibrium ratio is maintained at the interface.

$$C_1(0,t) = K[T(t)] C_2(0,t) \quad (\text{VIII-8})$$

Since the zirconium flux must be the same on either side of the interface, the boundary condition at the boundary is

$$-D_1[T(t)] \frac{\partial C_1(0,t)}{\partial x} = D_2[T(t)] \frac{\partial C_2(0,t)}{\partial x} \quad (\text{VIII-9})$$

It was assumed that there is no solute flux across the center of a grain

$$\frac{\partial C_1(-R_1,t)}{\partial x} = 0 \quad (\text{VIII-10})$$

$$\frac{\partial C_2(R_2,t)}{\partial x} = 0 \quad (\text{VIII-11})$$

where  $R_1$  and  $R_2$  are the radii of the grains. In the calculations presented here, the grain sizes were taken as  $R_1=R_2=7.5 \mu\text{m}$  (15  $\mu\text{m}$  grains).

To solve this problem numerically, Eqns. VIII-3, 4, 9, 10, and 11 are replaced by their backward difference analogs with the substitution  $y = -x$  for  $0 \leq x \leq R_2$ . Eqs. VIII-3 and 4 were replaced by a difference equation of the form

$$D[T(t)] C_{i-1,n+1} - C_{i,n+1} \left( 2D[T(t)] + \frac{(\Delta x)^2}{\Delta t} + D[T(t)] \right) C_{i-1,n+1} = - C_{i,n} \frac{(\Delta x)^2}{\Delta t} \quad (\text{VIII-12})$$

where  $n+1$  is an unknown level in time and  $i$  is a point in space. The

boundary conditions at  $x = -R_1$  and  $y = -R_2$  (Eqns. VIII-10, 11) are replaced by:

$$C_1(-R_1 + \Delta x, t) - C_1(-R_1, t) = 0 \quad (\text{VIII-13})$$

$$C_2(-R_2 + \Delta y, t) - C_2(-R_2, t) = 0 \quad (\text{VIII-14})$$

If  $R_1$  and  $R_2$  are divided into  $R$  units such that  $R\Delta x = R_1$  and  $R\Delta y = R_2$ , these equations form two matrices which are tridiagonal. These sets of simultaneous equations can be solved separately, and preliminary values for the distribution of solute in each grain determined up to the  $R-1$  step in space. (See Appendix B for this method.)

To include the boundary condition at the interface which couples the two differential equations, Eq. (VIII-9) was replaced by its finite difference analog

$$D_1 \frac{[C_1(0, t) - C_1(-\Delta x, t)]}{\Delta x} = - D_2 \frac{[C_2(0, t) - C_2(-\Delta y, t)]}{\Delta y} \quad (\text{VIII-15})$$

From the Thomas Tridiagonal method (91)

$$C_1(-\Delta x, t) = \gamma_{(1)R-1} - \eta_{(1)R-1} C_1(0, t) \quad (\text{VIII-16})$$

$$C_2(-\Delta y, t) = \gamma_{(2)R-1} - \eta_{(2)R-1} C_2(0, t) \quad (\text{VIII-17})$$

where  $\gamma$  and  $\eta$  are shown in Appendix B

These equations were then substituted into Eqn. (VIII-8) with the result:

$$C_2(0, t) = \frac{\frac{D_1 [T(t)] \gamma_{(1)R-1}}{\Delta x} + \frac{D_2 [T(t)] \gamma_{(2)R-1}}{\Delta y}}{\frac{D_1 [T(t)] K [T(t)]}{\Delta x} [1 + \eta_{(1)R-1}] + \frac{D_2 [T(t)]}{\Delta y} [1 + \eta_{(2)R-1}]} \quad (\text{VIII-18})$$

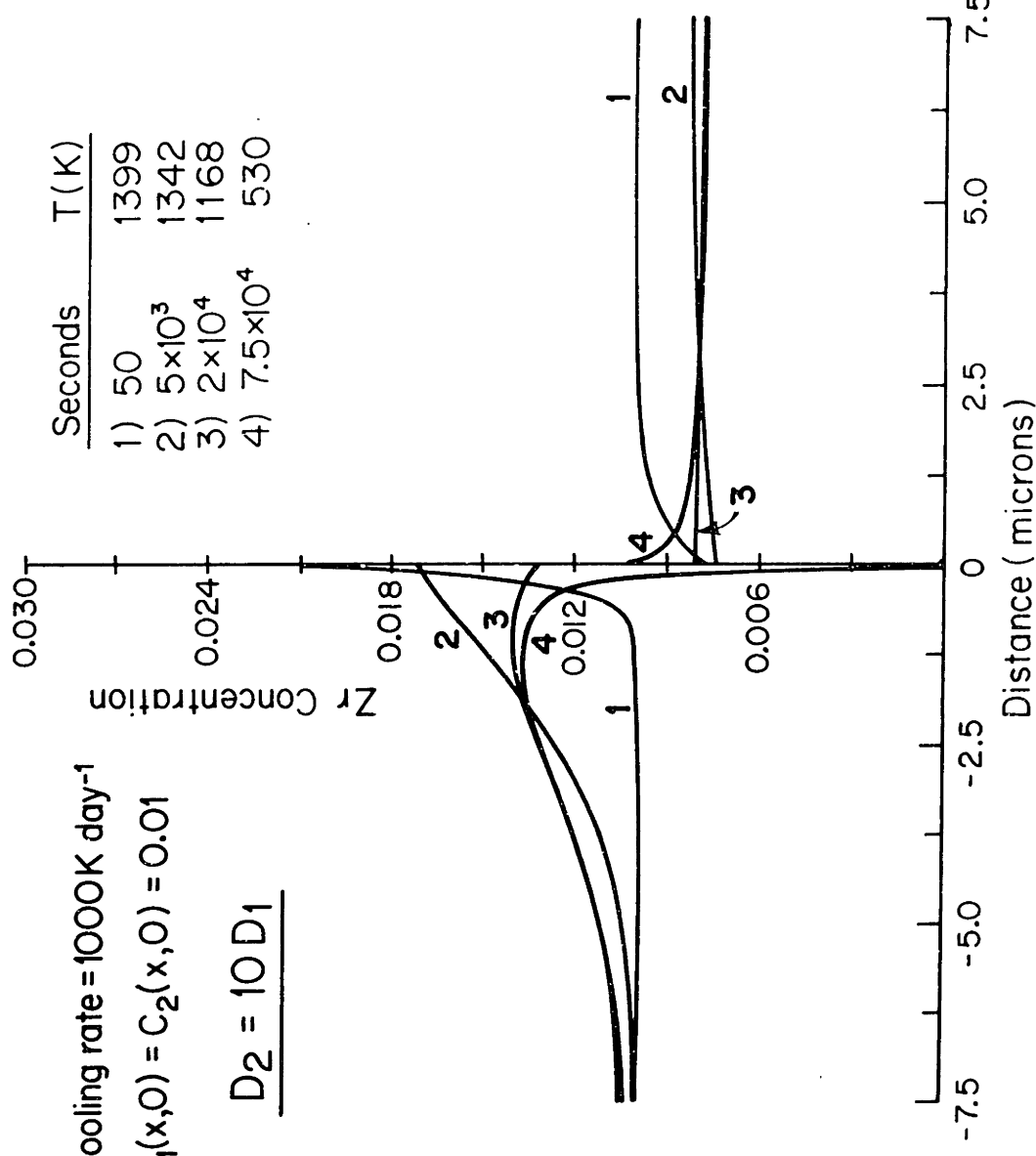
From Eqns. (VIII-8) and (VIII-18), the values of  $C_1(x,t)$  and  $C_2(x,t)$  can be calculated by the Thomas method. This procedure is repeated at every step in time.

The concentration profiles of Zr in coexisting ilmenite and ulvospinel were calculated for cooling rates over the range of 0.3 to 1000 K day<sup>-1</sup>. It was found that for slow cooling rates and high temperatures (large diffusivities), the results were inaccurate if the steps in time were too large. At high temperatures, the characteristic diffusion distance,  $\sqrt{Dt}$ , is comparable to the particle radius and the difference equation is no longer a good approximation to the differential equation. Therefore at high temperatures the time increment is small and as the temperature is decreased, the time increment is increased by one or more orders of magnitude.

The initial temperature of the diffusion couple is taken as 1400 K and the concentration of the solute is taken as 1%. This is probably somewhat high and a more realistic value would be 0.5% (44).

## 2. Results

If the diffusion coefficient in Phase 2 is 10 times that in Phase 1 and the initial solute concentration is uniform, at high cooling rates, the solute cannot equilibrate within one phase even at high temperatures. Concentration profiles of this type due to a cooling rate of 1000 C day<sup>-1</sup> are shown in Fig. VIII-1. There is a maximum concentration profile of Phase 1. At temperatures greater than 977 K, the equilibrium solute concentration at the boundary in Phase 1 is greater than that in Phase 2. Below 977 K the reverse is true. This results in an effective change in



Cooling rate =  $1000 \text{ K day}^{-1}$

$C_1(x,0) = C_2(x,0) = 0.01$

$$D_2 = 10 D_1$$

Figure VIII-1 - Solute concentration profiles for several times during cooling at  $1000 \text{ K day}^{-1}$  from  $1400 \text{ K}$ .  $D_2(T) = 10 D_1(T)$ . Uniform initial solute distribution.

the direction of diffusion, which is most evident during rapid cooling when equilibrium is not attained within the grains.

If the cooling rate is decreased to  $3 \text{ day}^{-1}$  (Fig. VII-2) and all other conditions are taken to be the same as in Fig. VIII-1, after an initial transient, equilibrium is maintained as the sample is cooled to about 1123 K. Below this temperature sufficient diffusion cannot take place and concentration gradients within the grains develop. After cooling is complete, significant gradients remain within  $3 \mu\text{m}$  of the grain boundary in Phase 1 and within about  $2 \mu\text{m}$  of the grain boundary in Phase 2. Solute concentration in the two phases is assumed to be at the equilibrium ratio at 1400 K (Fig. VIII-3), the initial transient as shown in Fig. VIII-2 is not present but the concentration profiles at all lower temperatures are identical to those shown in Fig. VIII-2. Again the concentration gradients are larger in Phase 1 than in Phase 2. If the diffusion coefficient is the same in both phases (Fig. VIII-4), the final concentration gradient at the interface in each phase differs from that calculated when  $D_2=10 D_1$ . In Phase 1, the gradient is smaller when  $D_2=D_1$  than when  $D_2=10 D_1$  in Phase 2, the gradient is larger when  $D_2=D_1$  than when  $D_2=10 D_1$ . As would be expected from Eqn. (VIII-9), when  $D_1=D_2$  the gradient in Phase 1 is equal to the opposite of the gradient in Phase 2.

The relation between cooling rate and the final ratio of concentrations is shown in Fig. VII-5. In calculating curves A, B, and C, it is assumed that the solute concentrations in each of the phases was at equilibrium at high temperatures. Curve A indicates the relation between

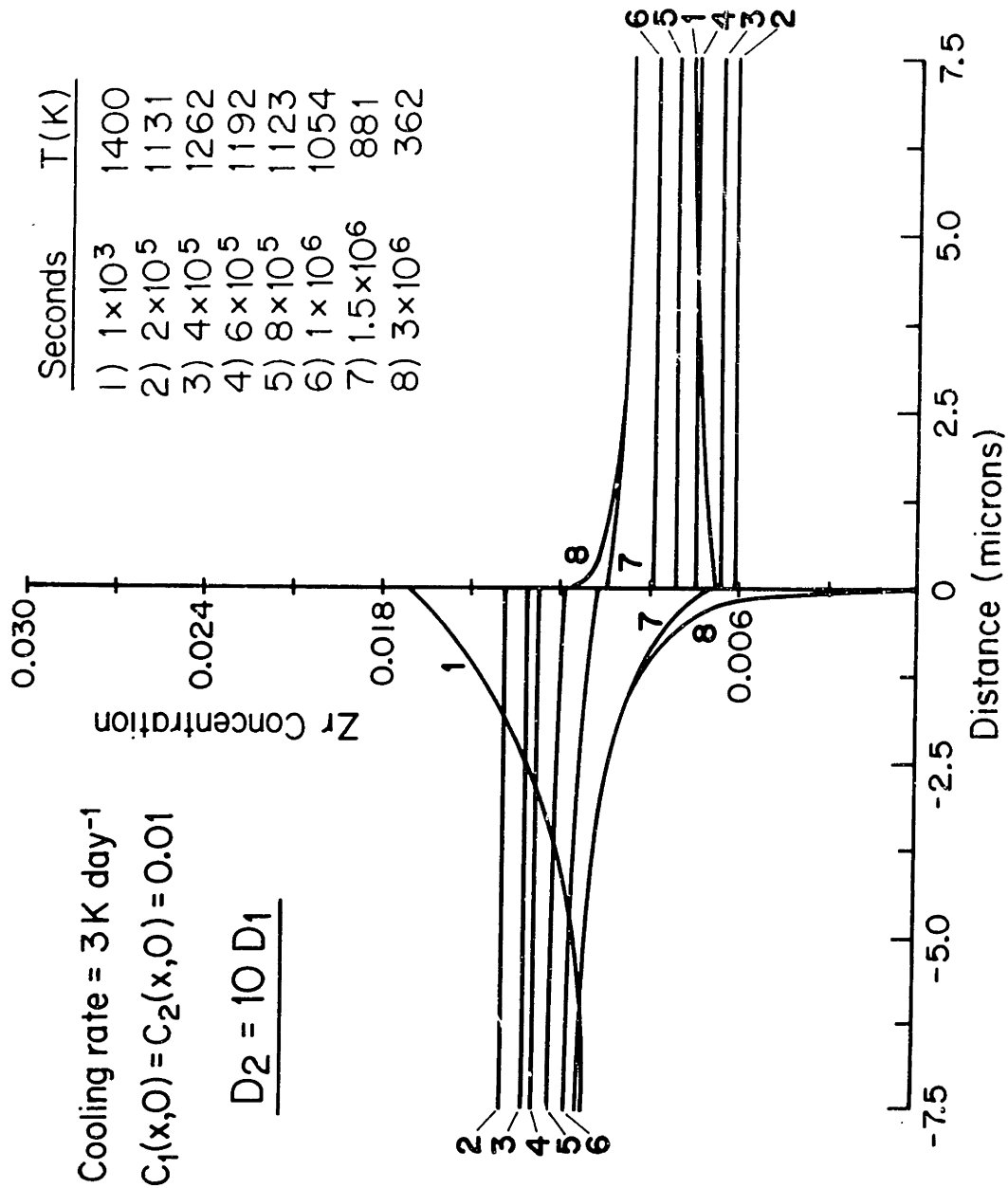


Figure VIII-2 - Solute concentration profiles for several times during cooling at  $3 \text{ K day}^{-1}$  from 1400 K.  $D_2(T) = 10D_1(T)$ . Uniform initial solute distribution.

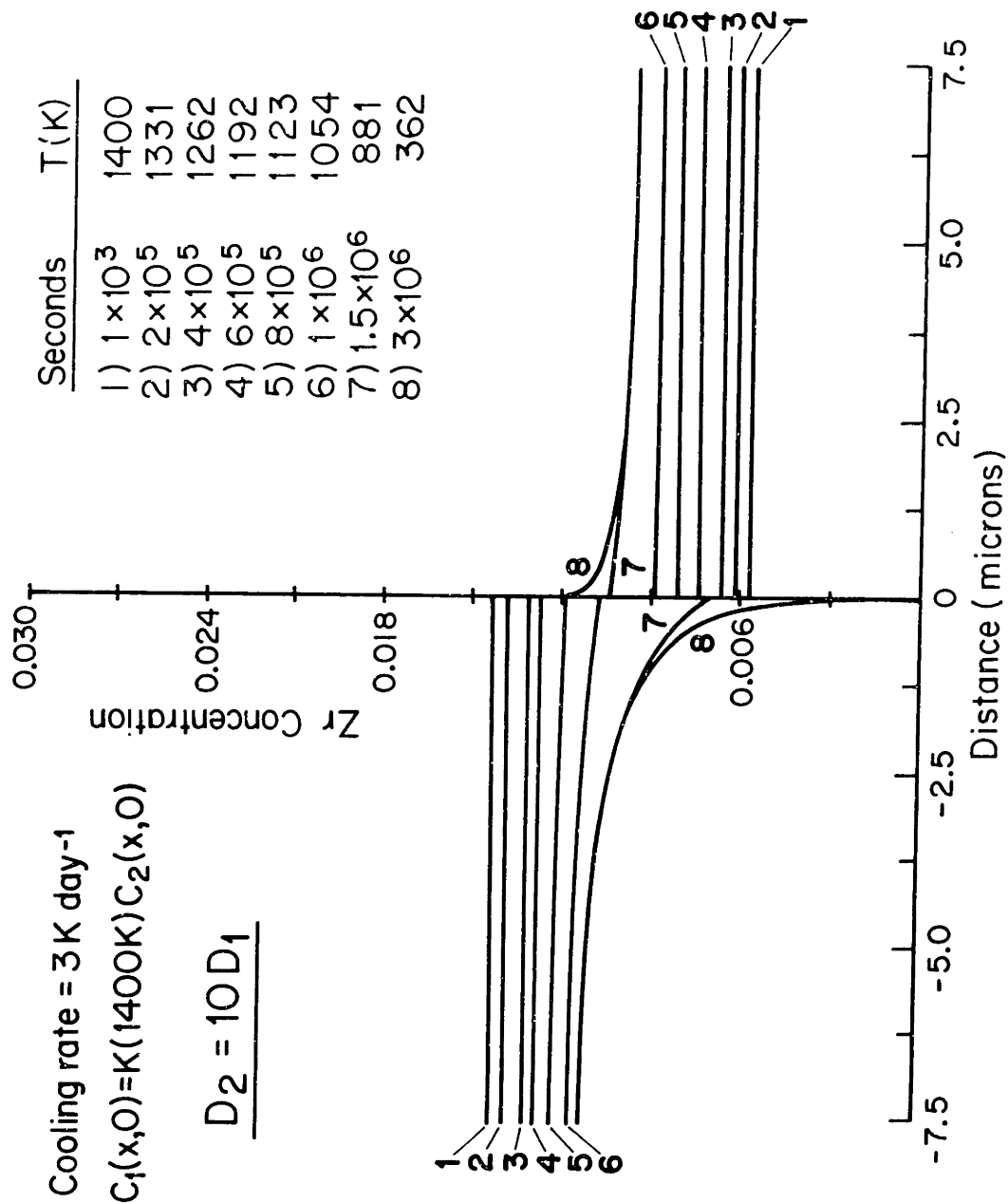


Figure VIII-3 - Solute concentration profiles for several times during cooling at 3 K day<sup>-1</sup> from 1400 K.  $D_2(T) = 10D_1(T)$ . Equilibrium initial solute distribution.



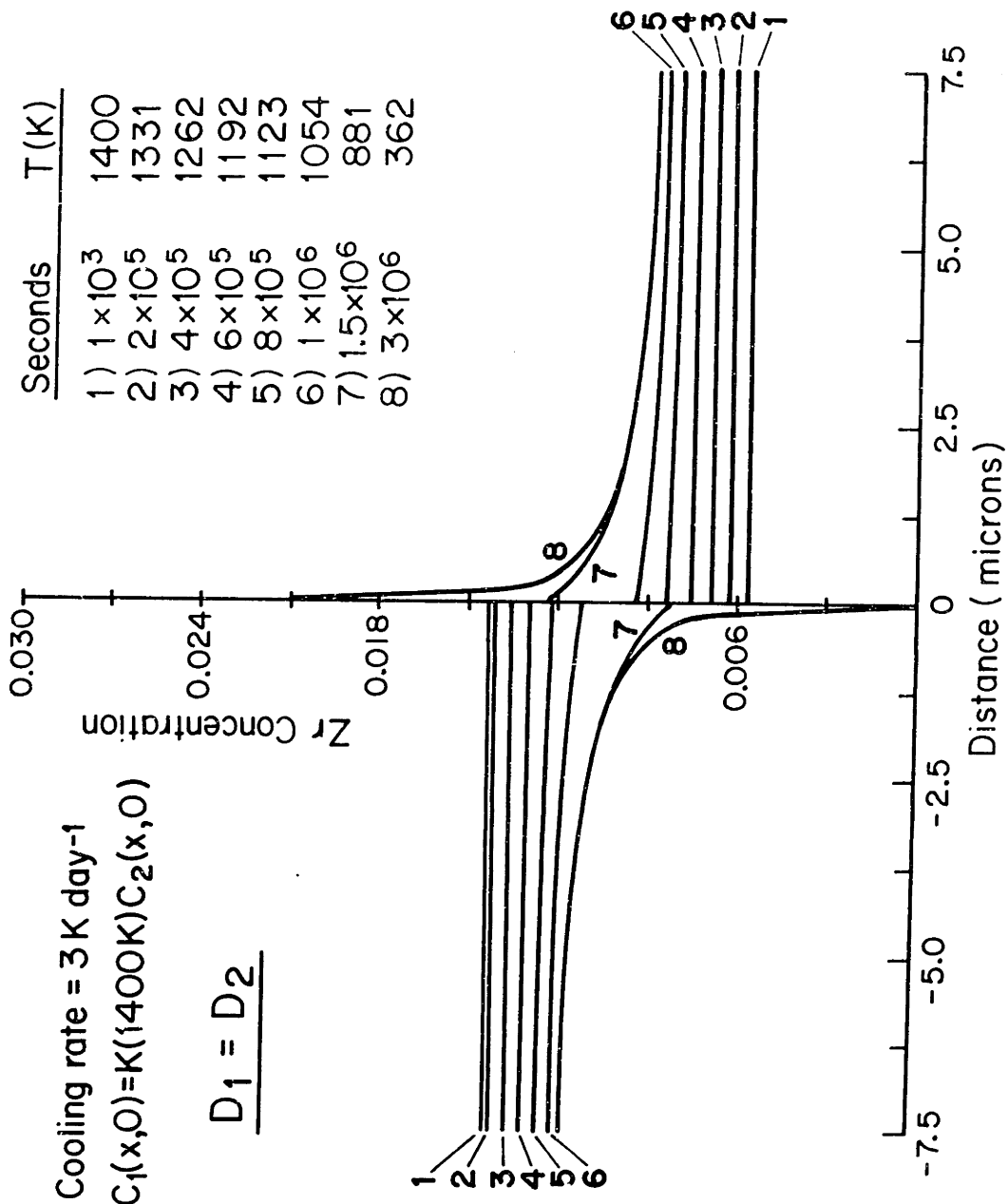


Figure VIII-4 - Solute concentration profiles for several times during cooling at 3 K day<sup>-1</sup> from 1400 K.  $D_2(T) = D_1(T)$ . Equilibrium initial solute distribution.

the ratio of the average solute concentration in each phase and the cooling rate, assuming  $D_2=10 D_1$ . In calculating Curve B it was again assumed that  $D_2=10 D_1$ , but the compositions at the center of the grains was used to compute the ratio. This curve more closely approximates the experimental situation because there are large gradients near the boundary which would change the average compositions but could not be measured using an electron microprobe. Curve C is determined assuming  $D_1=D_2$  and the concentrations to be compared are those at the center of the grains.

For a given solute concentration ratio, Curve A indicates a higher cooling rate than that indicated by Curve B, which in turn indicates a higher cooling rate than Curve C. These differences are significant: The predicted cooling rate can vary by more than a factor of 10 depending on how the solute concentration ratio is determined. Also shown are points representing the final solute concentration ratios calculated from the average and the center concentrations of the grains when the phase cannot equilibrate at high temperatures as in Fig. VIII-1. At lower cooling rates, the phases are able to equilibrate and the calculated solute concentration ratios coincide with those calculated assuming equilibrium initial conditions (Eq. VIII-7).

### 3. Discussion

The above results show that the nonisothermal partitioning of a solute between two phases can be used to determine the cooling rate of a rock. There is a significant variation in the ratio of solute concentration of two adjacent grains with cooling rate. However, there is a

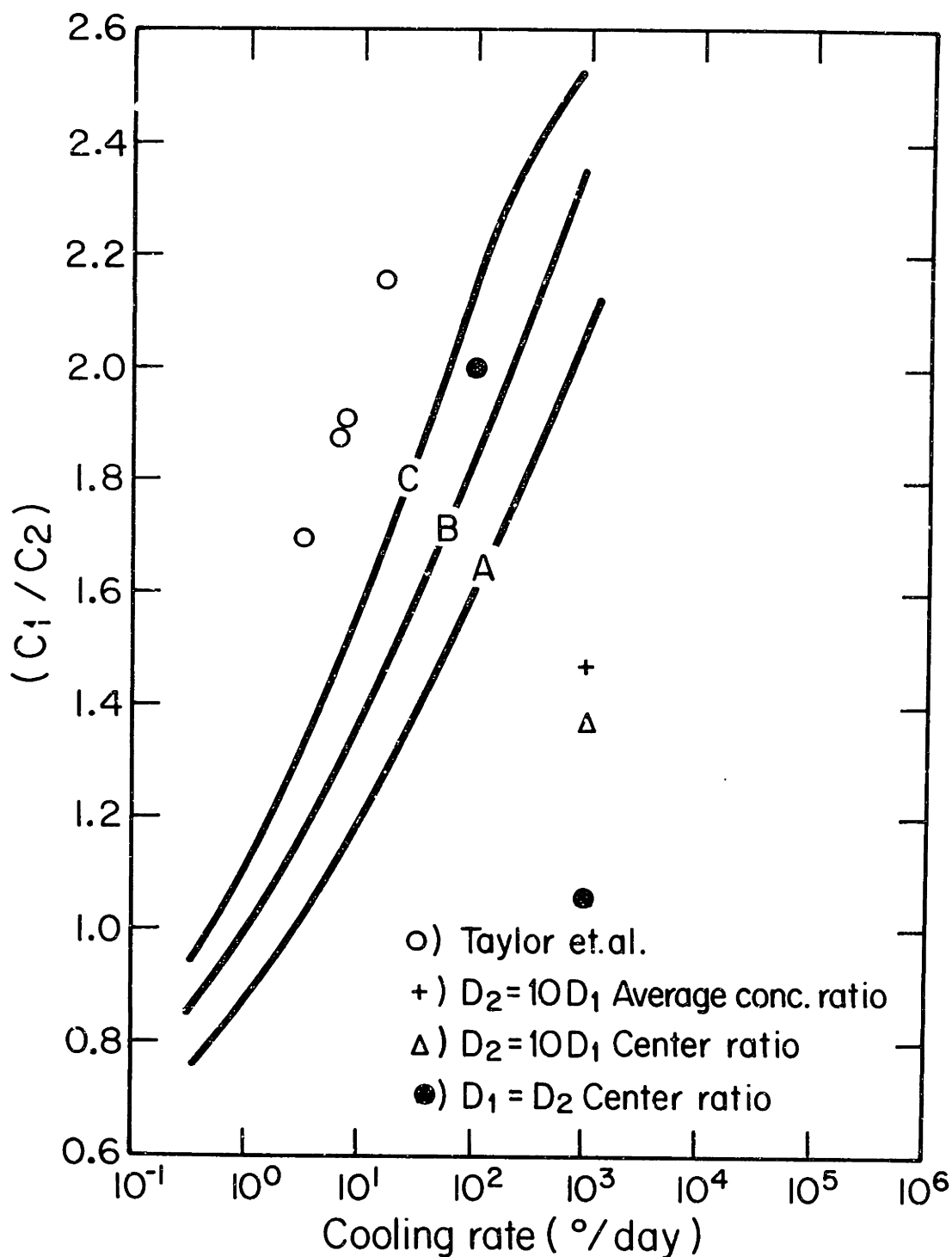


Figure VIII-5 - Solute concentration ratio as a function of cooling rate. A = average solute concentration ratio,  $D_2(T) = 10D_1(T)$ ; B = center solute concentration ratio,  $D_2(T) = 10D_1(T)$ ; C = center solute concentration ratio,  $D_2(T) = D_1(T)$ ; +,  $\Delta$ , o - Uniform initial solute distribution; A, B, C - Equilibrium initial solute distribution.

strong dependence of estimated cooling rate on the technique of measuring the ratio of solute concentrations. According to the results presented here, there are large gradients within 2 to 3 microns of the interface. These gradients cannot be measured by conventional electron microprobe techniques. Therefore a more realistic model to compare with experimental values of the solute concentration ratio is one that considers only the solute concentrations at the center of the grains. By comparing Curves A and B of Fig. VIII-5, the effect of changing the method of calculating the solute concentration ratio on the estimated cooling rate can be seen. Use of the average concentrations in the grains predicts a cooling rate that is faster by a factor of about three than using the concentrations at the center of the grains. This is constant for all heating rates.

Changes in the initial conditions can also have an important effect on the final solute concentration ratio. At high cooling rates, a sample with an initial uniform solute distribution exhibits much less solute partitioning than one with an initial equilibrium solute distribution. The same center concentration ratio of  $C_1/C_2 = 1.37$  could be obtained if a sample had a uniform solute distribution and was cooled at  $1000 \text{ D day}^{-1}$  or it had an equilibrium solute distribution and was cooled at  $10 \text{ K day}^{-1}$ . However, the concentration profiles within the grains would be quite different. There would be no danger in choosing the wrong cooling rate because there would be other morphological differences between rocks cooled at these drastically different rates.

The solute concentration ratio is also dependent on the diffusivity of the solute in both grains, and not just the slower one. During

cooling, there is first a temperature at which the slower phase cannot equilibrate. This causes both the average and center ratios to deviate from the equilibrium concentration ratio. Assuming however that equilibrium holds at the boundary, continued diffusion will take place in the faster phase, resulting in continued change of the center and average solute concentration ratios.

If the diffusivity is the same in both phases, the final center concentration ratio corresponds to a higher temperature at which partitioning effectively stops. How this effects the concentration ratio depends on the temperature dependence of the partition coefficient. In this case, a given center concentration ratio indicates a cooling rate that is slower by a factor of about 2-4 when the diffusivities are the same compared with that estimated when  $D_2(T) = 10 D_1(T)$ . This difference is a factor of only 2 when the average concentration ratios are compared. Therefore it is important to know the diffusion coefficient of the solute in both phases. In Fig. VIII-5, the open circles correspond to the results of Taylor et al. (44). The results presented here indicate a cooling rate that is higher by a factor of about 6 for a given solute concentration ratio. The model proposed by Taylor et al. is a very rough method of cooling rate approximation. Taking the square root of the integrated time dependent diffusion coefficient as equal to the radius of the grain ignores the finite grain size as well as any Zr partitioning below a characteristic temperature  $T_0$ .

When the results which assume  $D_1=D_2$  are applied to the determination of the cooling rates of the Apollo 15 Elbow Crater gabbros 15065, 15075,

15076, 15085, it is estimated that they cooled at rates of 18, 18, 25, and  $39 \text{ C day}^{-1}$ , respectively. This was done by using the measured Zr partition of Taylor et al. (44). The measured Zr ratio is accurate to about  $\pm 10\%$ . This results in an accuracy within a factor of 2 in the cooling rate estimated here. This is in good agreement with the results of Lofgren (99) that these lunar samples cooled at rates of less than  $24 \text{ C day}^{-1}$ . In that experiment the cooling rate was estimated by crystallizing a melts of the appropriate composition at known cooling rates and reproducing the texture and mineralogy of the lunar samples. The accuracy of this technique was estimated to be within a factor of 2 or 3. Of the conditions explored in the present work, the best agreement with the results of previous work was obtained by assuming that  $D_1(T) = D_2(T)$  and that the solute concentration measured is that at the center of the grains. This suggests that the diffusivity of Zr is the same in ilmenite and ulvospinel. More importantly, these results stress the importance of accurately measuring the diffusion coefficient in both phases of interest. This technique can be applied to any system which meets the criteria stated earlier and is useful in determining the absolute cooling rates of lunar and terrestrial rocks.

#### 4. Conclusions

The partitioning of Zr between existing ilmenite and ulvospinel can be used to estimate the cooling rate of lunar and terrestrial rocks, providing that the concentration of Zr can be measured accurately.

The estimated cooling rate for a given solute concentration ratio depends on the diffusivities in both phases and not just on the lower

diffusivity. For high cooling rates ( $100-1000 \text{ K day}^{-1}$ ) the ratio depends on the initial conditions to lower cooling rates, the grains ( $7.5 \mu\text{m}$  radius) can reach equilibrium at high temperatures and the initial conditions are not important. The final center and average solute concentration ratio in larger grains would be affected by the initial conditions for cooling rates lower than  $100 \text{ K day}^{-1}$ . For high cooling rates or larger grains, the initial temperature of the calculations is important; for small grains or low cooling rates, equilibrium can be reached over a range of temperatures as the rock cools and the initial temperature does not change the final center and average concentration ratios.

Rather than measuring a solute concentration at a given distance from the grain boundary, actual concentration gradients should be measured to determine the extent of solute partitioning and diffusion. This method of absolute cooling rate determination in rocks can be applied to any system in which (1) the diffusion and partition coefficients can be determined as a function of temperature, (2) the activity coefficients are constant over the composition range of interest, (3) there is no precipitation of a third phase, and (4) the major phase relations are not affected by the presence of the solute.

## B. Diffusion in Olivine

Of the major igneous rock-forming minerals (e.g., pyroxene, plagioclase, olivine), the complications of the phase equilibria and kinetics within the pyroxene and plagioclase systems are well known. However, the relatively simpler chemistry of olivines should lend itself to geothermometry.

The present study was directed at the olivine system, in particular, the diffusion of  $\text{Fe}^{++}$  and  $\text{Mg}^{++}$  within compositionally zoned olivines, forsterite ( $\text{Mg}_2\text{SiO}_4$ ) and fayalite ( $\text{Fe}_2\text{SiO}_4$ ). Partitioning of Fe and Mg between olivine and orthopyroxene has been shown (104) not to be significantly temperature dependent over the temperature range 900-1300 °C. Hence, diffusion across olivine-pyroxene grain boundaries can be assumed to be minimal, and the reequilibration of compositionally zoned olivines is largely one of response to prolonged cooling. Thus, a given compositional gradient within an olivine grain will tend to decrease with time at slow cooling rates until the olivine is chemically homogeneous.

### 1. The Model

The minimum cooling rate necessary for the preservation of compositional zoning in an olivine grain has been determined. At equilibrium, there are no concentration gradients in the forsterite-fayalite system. The extent to which a grain approaches equilibrium during cooling depends upon the concentration profile at the solidus, as well as upon the thermal history (cooling rate). Lacking information about the as-solidified concentration profile, it has been assumed that at the solidus, there was a step-function in the forsterite concentration within the grain. That



is, initially there are no compositional gradients within the grain other than the infinite gradient at the boundary between the Fo-rich core and a Fa-rich rim.

This assumption directs attention to the minimum cooling rates associated with the preservation of a given gradient since a system with an initial gradient would equilibrate more rapidly than one with a step-function profile. Likewise, the largest compositional gradients found in the olivine crystals of a particular sample were used for this analysis. It has also been assumed that there is no flux either across the center of the grain or across the grain boundary. The initial Fe concentrations in the core,  $C_1$ , and the rim,  $C_2$ , were varied slightly. In order to determine the relative initial sizes of the core and the rim,  $x_1$  and  $x_2$ , it was assumed that the grain was effectively a closed system and that mass balance was maintained.

Attention was specifically directed to a finite system, rather than an infinite system as described by Lasaga and Richardson (100). Concentration profiles were calculated for both one-dimensional and spherical geometries. The one-dimensional case is described by the same equations as the solute partitioning model presented earlier in this chapter with the exception of Eqn. (VIII-8) and the inclusion of the concentration dependence of the diffusivity. The results do not vary significantly from those calculated for the spherical geometry in which the shape of a grain is approximated by a spherical Fo-rich core and a thin spherical Fa-rich shell.

The equation which describes diffusion within a spherical grain is

$$\frac{\partial^2 C}{\partial t^2} = \frac{1}{r^2} \frac{\partial}{\partial t} \{ r^2 \tilde{D}_a [C(r), T(t)] \frac{\partial C}{\partial r} \} \quad (\text{VIII-18})$$

where  $C$  is the mole fraction of fayalite Fe and  $\tilde{D}_a$  is the interdiffusion coefficient in the  $a$  crystallographic direction. The initial conditions are:

$$\begin{array}{ll} \text{for } 0 < r < r_1 & \text{for } r_1 < r < r_1 + r_2 \\ C(r, 0) = C_1 & C(r, 0) = C_2 \end{array} \quad (\text{VIII-19a})$$

where  $r_1$  is the radius of the core and  $r_2$  is the thickness of the rim. These conditions can be changed to include segregation during solidification if the distribution coefficient is known as a function of temperature. Such modified conditions can readily be handled by the program used to solve the diffusion problem.

The boundary conditions are

$$\frac{\partial C(0, t)}{\partial r} = \frac{\partial C(r_1 + r_2, t)}{\partial r} = 0 \quad (\text{VIII-19b})$$

Expanding Eq (VIII-18) results in the following expression

$$\frac{\partial^2 C}{\partial t^2} = \tilde{D}_a \frac{\partial^2 C}{\partial r^2} + \left( -\frac{2\tilde{D}_a}{r} + \frac{\partial \tilde{D}_a}{\partial r} \right) \frac{\partial C}{\partial r} \quad (\text{VIII-20})$$

Two experimental determinations of the interdiffusion coefficient have been made (42, 43). To determine which of these data would be used, isothermal diffusion experiments were conducted (44), the procedure and results are presented in Appendix C. The results of Buening and Buseck are used in the present work.

Buening and Buseck (43) showed that the interdiffusion of Fe and Mg<sup>++</sup> in olivine is a function of (1) temperature, (2) composition, (3)  $f_{O_2}$ , and (4) crystallographic direction. In the forsterite-fayalite system at an  $f_{O_2}$  of  $10^{-12}$  and in the  $c$  direction, the interdiffusion coefficient,  $\tilde{D}_c$ , is

$$\tilde{D}_c = \exp(-.0501 X_{Fe_2SiO_4} - 14.03) \exp\left\{-\frac{(1.373\text{ev} - .0095 X_{Fe_2SiO_4})}{kT}\right\} \quad (\text{VIII-21})$$

for  $T$  1125°C. The diffusion coefficient varies with oxygen partial pressure as

$$\tilde{D} = K \cdot p_{O_2}^{(.172)} \quad (\text{VIII-22})$$

with an accuracy in the exponent of  $\pm 0.022$ . This is consistent with a simple vacancy process which exhibits a pressure dependence of  $p_{O_2}^{1/6}$ . This was used to determine the diffusion coefficient over a range of temperatures and partial pressures of oxygen.

$$\tilde{D}_c = 10^2 p_{O_2}^{1/6} \exp(-.0501 X_{Fe_2SiO_4} - 14.03) \exp\left\{-\frac{(1.373\text{ev} - .0095 X_{Fe_2SiO_4})}{kT}\right\} \quad (\text{VIII-23})$$

The oxygen partial pressure which corresponds to lunar conditions is about 0.5 log atm. below the iron-wustite buffer curve (105). The temperature dependence of the log of the oxygen partial pressure is approximately linear.

$$\log_{10} p_{O_2} = .015T(^{\circ}K) - 34.6 \quad (\text{VIII-24})$$

Buening and Buseck show a significant anisotropy in the diffusion coefficient. No analytical expression was given for this difference, but the tabulated data indicate that  $\tilde{D}_c$  is greater than  $\tilde{D}_a$  by a factor of about 4 at 1050°C. As an approximation, it will be assumed that

$$\tilde{D}_a = \frac{\tilde{D}_c}{4} \quad (\text{VIII-25})$$

for all temperatures. The anisotropy increases as the temperature decreases; so the approximation overestimates the extent of diffusion below 1050°C and to a lesser degree underestimates it above 1050°C. Combining Eqns. (VIII-22, 23, and 25) results in the following expression for the fayalite concentration as a function of time and temperature only

$$\begin{aligned} &.04 \exp(-.00576T + 13.28) \exp(.0501C + 1403) \exp \frac{(1.373\text{ev} - .0095C)}{kT} \frac{\partial C}{\partial t} \\ &= \frac{\partial^2 C}{\partial r^2} + \left[ \frac{2}{r} + (-.0501 + \frac{.0095}{kT}) \frac{\partial C}{\partial r} \right] \frac{\partial C}{\partial r} \end{aligned} \quad (\text{VIII-26})$$

Equation (VIII-26) has been solved by replacing it with its finite difference analog, applying the boundary conditions, and solving the resultant set of simultaneous equations by the Thomas tridiagonal method (Appendix B). Due to the non-linearity of the equation, it was necessary to iterate the procedure to approach the correct solution.

Concentration profiles were calculated for several cooling rates and sets of initial conditions. The values of  $r_1$ ,  $r_2$ ,  $C_1$  and  $C_2$  indicate possible solidus conditions in the lunar samples investigated. These parameters could not be changed independently because mass balance and the size of the grain had to be maintained.

For cooling rates larger than about  $5^\circ\text{C day}^{-1}$ , there was little change in the forsterite profile at temperatures below about  $750^\circ\text{C}$ . Cooling rates smaller than about  $1^\circ\text{C day}^{-1}$  allowed diffusion to be effective at lower temperatures. Since the diffusion coefficient depends on concentration, each case (i.e., olivine grain) must be considered

separately. The absolute concentration, as well as the concentration gradient, are important parameters for specifying the minimum cooling rates.

## 2. Results

Two lunar samples were chosen (i.e., 12002 and 15555) for which cooling rates have been experimentally estimated based on dynamic crystallization studies (41, 106, 107). Therefore, these samples provide a means of comparison between our theoretical approach and the empirical studies. Since the two lunar specimens are compositionally and texturally different, different cooling rate estimates should be obtained from compositional gradients in their olivines.

To estimate the initial conditions the planar geometry was assumed and the measured Mg concentrations integrated over the grain. Assuming a constant Mg content and initial core and rim compositions, it was then possible to estimate the relative initial sizes of the core and the rim. Due to the large grain size this assumption of planar geometry is sufficient for the determination of the relative core and rim sizes. Sample 12002 olivine originally had a core radius of 234  $\mu\text{m}$  and a rim thickness of 60  $\mu\text{m}$ . According to the best fit of calculated forsterite distribution, the core initially contained 73.5% Fo and the rim, 58.5% Fo. In similar manner, 15555 had a core radius of 188  $\mu\text{m}$  and a rim of 106  $\mu\text{m}$  thick. The core contained 62% Fo and the rim, about 5% Fo.

Figures VIII-6 and VIII-7 show the compositional profiles as a function of temperature for samples 12002 and 15555 starting with the initial step-function assumption. The cooling rates for the two samples,

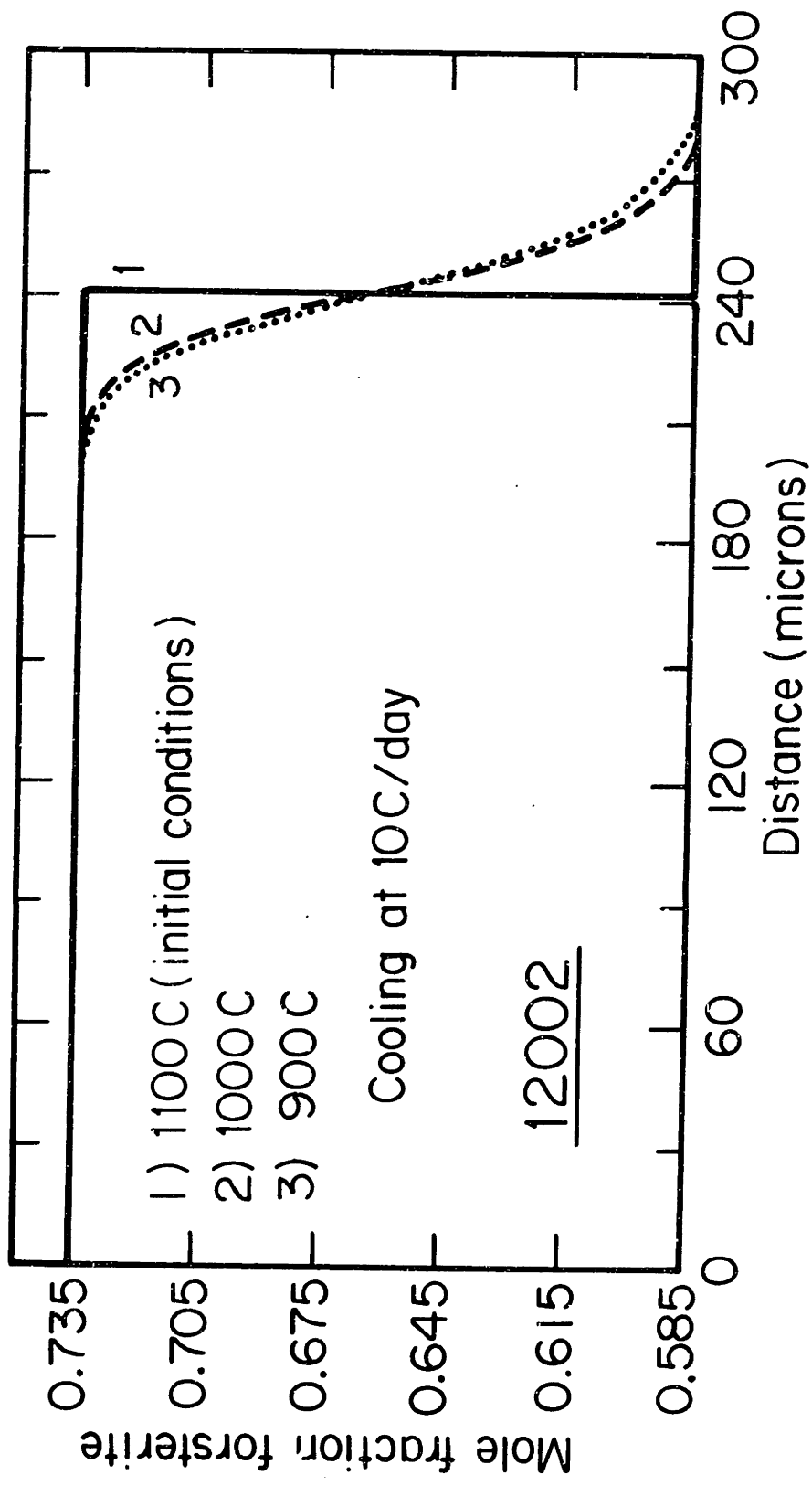


Figure VIII-6 - Calculated composition profiles in grain of lunar composition 12002 at several temperatures during cooling at 10 C day<sup>-1</sup> from 1100 C.

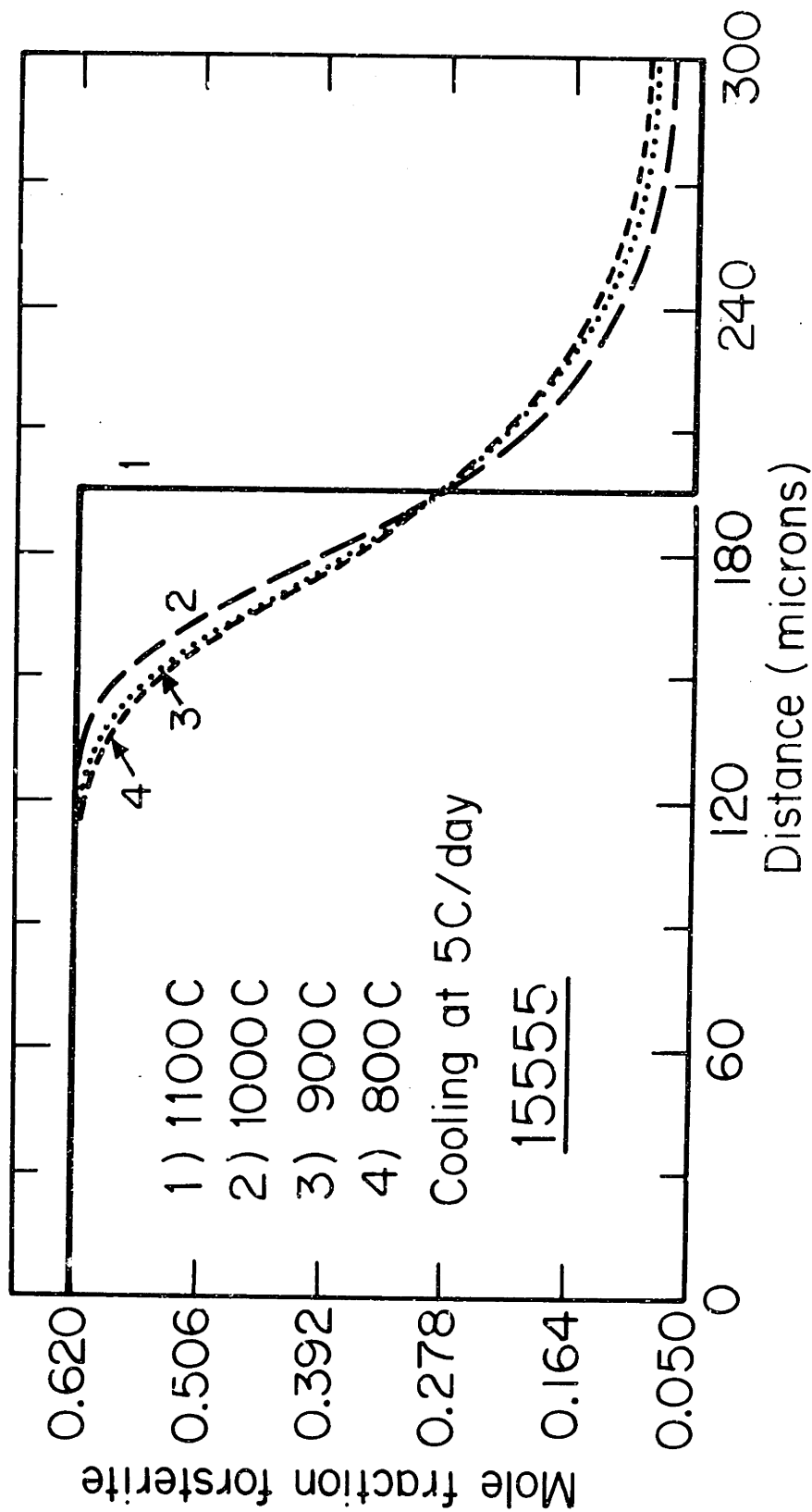


Figure VIII-7 - Calculated composition profiles in grain of lunar composition 15555 at several temperatures during cooling at 5 C day<sup>-1</sup> from 1100 C.

assumed for illustration, are  $10^\circ$  and  $5^\circ\text{C day}$ , respectively. The calculated curves labelled 2-4 were generated by cooling from  $1100^\circ\text{C}$  to  $1000^\circ$ ,  $900^\circ$ , or  $800^\circ\text{C}$ , followed by quenching. As to be expected, the temperature to which effective diffusion is still operative is lower for the slower cooling rate. Below  $900^\circ\text{C}$  in the case of 12002 at  $10^\circ\text{C day}$  (Fig. VIII-6) and  $800^\circ\text{C}$  for 15555 at  $5^\circ\text{C day}$  (Fig. VIII-7), there is little change in the profiles--i.e., they converge.

Figures VIII-8 and VIII-9 show the calculated diffusion profiles for lunar compositions 12002 and 15555 as a function of cooling rate. The calculated profiles are compared with the profiles measured in these samples by Taylor (Appendix C). Grains exhibiting the steepest concentration gradient between the core and the rim were used for the cooling rate estimates. The agreement between the calculated and observed profiles is good for  $10\text{ C day}^{-1}$  and  $5\text{ C day}^{-1}$  for 12002 and 15555 respectively.

### 3. Discussion

The cooling rates presented above compare favorably with those obtained from controlled crystallization studies by Walker et al. (41, 107) and Bianco and Taylor (106). These investigators estimated rates of  $10\text{-}20^\circ\text{C day}^{-1}$  for both of these rocks. The results from the present study are lower by a factor of 2-3. However, it should be emphasized that the olivine-based cooling rate estimates presented here are minima, since an initial step function rather than an "as-solidified" profile was used. Walker et al (107) have recently compared the cooling rates estimated according to Zr partitioning, and olivine homogenization



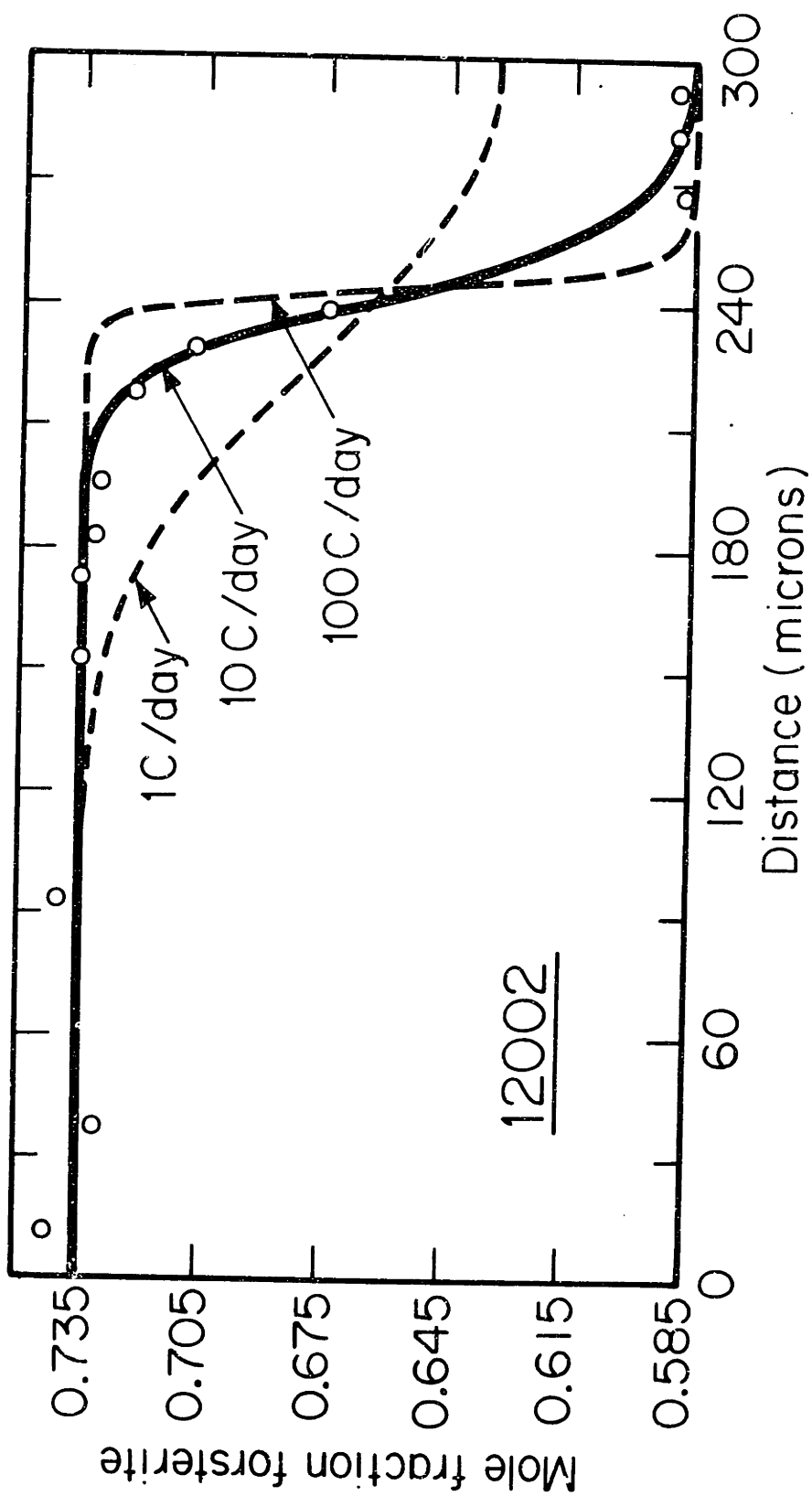


Figure VIII-8 - Measured composition profiles and final composition profiles calculated for cooling rates of 1, 10 and 100 C day<sup>-1</sup> in lunar composition 12002.

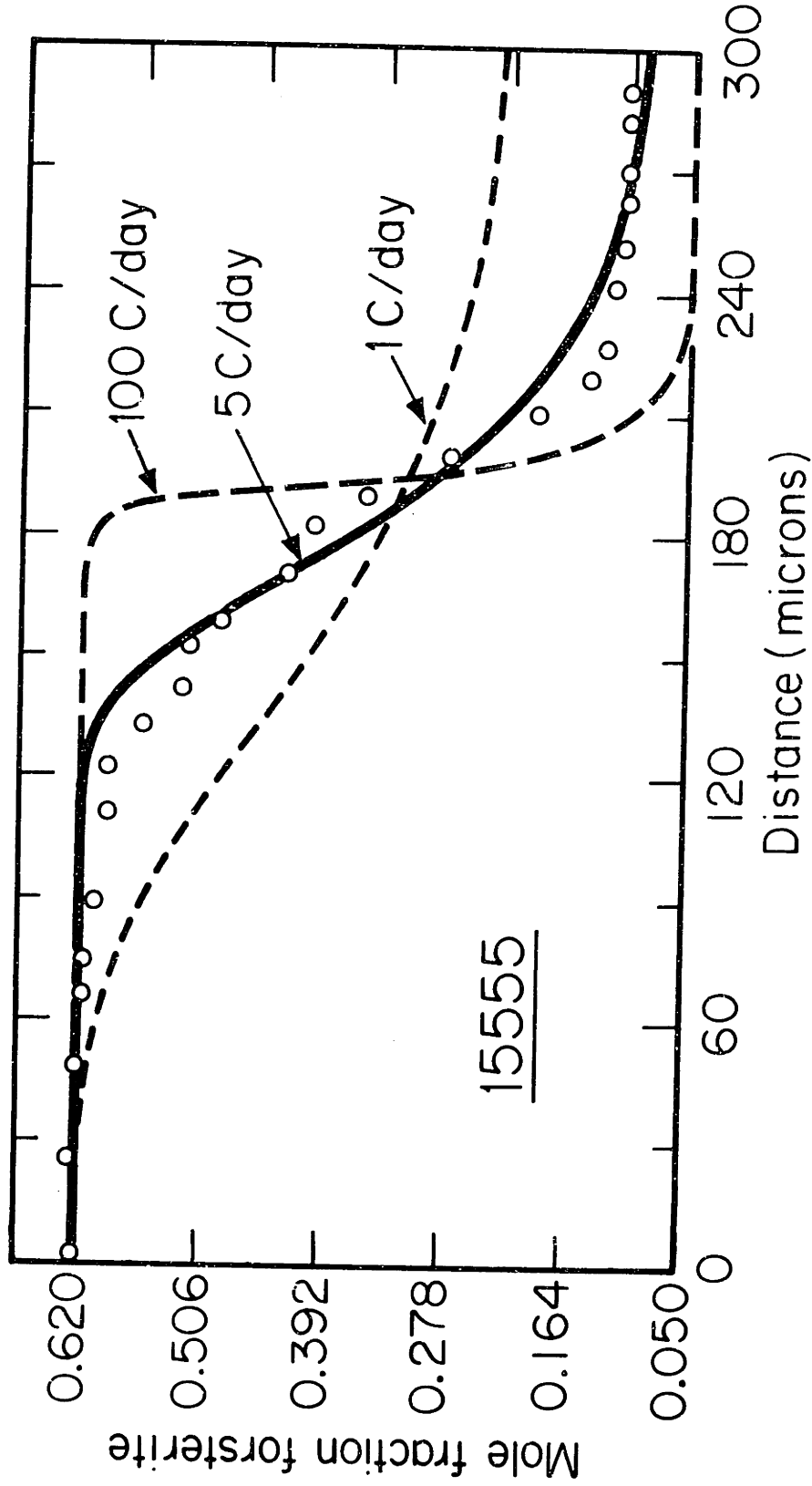


Figure VIII-9 - Measured composition profiles and final composition profiles calculated for cooling rates of 1, 5, and 100 C day<sup>-1</sup> in lunar composition 15555.

following to the model of Taylor (44) with an olivine homogenization model which solves the diffusion equation exactly. To do this it is necessary to ignore the compositional dependence of the diffusion coefficient. A closed system and an initial concentration indicate characteristic of that in zoned phenocrysts which have not homogenized were assumed. A cooling rate higher by a factor of three than that calculated according to Taylor (44) model was found. It was also assumed that the diffusion distance is equal to the grain size although it can be seen from microprobe analysis that the characteristic diffusion distance can be much smaller. This smaller diffusion distance results on higher cooling rates. It was suggested that the solution to the diffusion equation is more dependent on the diffusion distance and the diffusion coefficient than on the initial concentration profiles and grain geometry. We found that solving the diffusion equation for the one-dimensional case (two parallel plates rather than a sphere) resulted in virtually identical concentration profiles. The diffusion coefficient is a function of concentration so in order to compare calculated profiles with actual profiles, this must be taken into account. The agreement between calculated and measure profiles shown in Fig. VIII-8 emphasizes this point.

The use of the spherical geometry is important when the effect of finite size of the grain is important. In the lunar samples considered here, large regions in the core of the grains exhibited flat concentration profiles, indicating that the effective diffusion distance was less than the radius of the grain. However, the concentration gradient in the rim is affected by the finite nature of the rim. Therefore it is necessary

to use a finite geometry in this case. However, it is not necessary to use a spherical geometry. If the grains were smaller or the cooling rate lower so that the finite size of the core is significant, it would be necessary to use the spherical geometry. In Fig. VIII-9, the agreement between measured and calculated profiles is not as good as in Fig. VIII-8. This could be the result of a different initial profile or a higher initial temperature.

The cooling rates estimated here are minimum rates because if there were any initial finite gradients within the olivine grain, it would tend to equilibrate more rapidly and a higher cooling rate would be necessary to preserve the observed gradient. With more refined knowledge of the starting profile, a more detailed statement of the absolute cooling rate is possible.

#### 4. Conclusion

The compositional zonation in olivines can be used to estimate cooling rates. The  $\text{Fe}^{+2}$  and  $\text{Mg}^{+2}$  diffusion in olivine is a function of (1) temperature, (2) composition, (3)  $f\text{O}_2$ , and (4) crystallographic orientation. Differences in cooling rates between otherwise similar rocks can be discerned. A model was developed to describe the nonisothermal diffusion within an olivine grain. An initial step function in the concentration is assumed, the position of this step is based on mass balance considerations of the measured compositional profile. This results in a minimum cooling associated with the preservation of a given gradient. The cooling rates of lunar rocks 12000 and 15555 were estimated as  $10^\circ\text{C day}^{-1}$  and  $5^\circ\text{C day}^{-1}$  respectively.

## IX. THE EFFECT OF MOTION ON THE FINING OF GLASS MELTS

This chapter is concerned with establishing the ranges of bubble size and fluid motion where fining will be significantly affected by motion. The model presented below takes into account the effects both of the moving boundary and of the bubble rising through the melt. To avoid undue complexity, the description is concerned with bubble growth and dissolution associated with the diffusion of a single gas (oxygen); and complications due to the presence of another gaseous species have been neglected.

### A. The Model

Equation (IX-1) is the expression which governs the diffusion of a gas in the region of a bubble of radius  $a$ , which is moving through a melt and shrinking:

$$\frac{\partial C}{\partial t} = - \frac{a^2}{r^2} \frac{da}{dt} \frac{\partial C}{\partial r} - v_r \frac{\partial C}{\partial r} - \frac{v_\theta}{r} \frac{\partial C}{\partial \theta} + D \nabla^2 C \quad (\text{IX-1})$$

Here  $C$  is the concentration of the gas;  $t$  is time;  $r$  is the radial distance from the center of the bubble;  $v_r$  and  $v_\theta$  are, respectively, the radial and tangential components of the velocity; and  $D$  is the diffusion coefficient.

On the right side of the equation, the first term represents the contribution due to the moving boundary as the bubble shrinks. The second and third terms represent the convective flux due to the radial and tangential velocities of the melt. The components of the velocity are those relative to a sphere with a fluid boundary. At the surface of the bubble, the radial component of velocity is zero but the tangential

component is not. Due to the fluidity of the boundary, the gas bubble rises through the melt at a rate  $V_o$  which is 1.5 times faster than the velocity calculated according to Stokes' Law. This rate may be expressed:

$$V_o = \rho g a^2 / 3\eta \quad (\text{IX-2})$$

Here  $\rho$  is the density of the melt,  $g$  is the gravitational constant and  $\eta$  is the viscosity of the melt.

It has been assumed in the calculations that the diffusion coefficient is independent of concentration. In some calculations, it was assumed that Henry's law applies at the bubble-melt interface; in others, a constant concentration at the interface was applied. Far from the interface, the concentration is taken as a constant,  $C_\infty$ . The boundary conditions are:

$$C(R,t) = C_\infty \quad (\text{IX-3a})$$

$$C(a,t) = C_o \quad (\text{IX-3b})$$

where  $C_o = C_s$  when the concentration at the interface is constant, and  $C_o = C_s (1 + 2\sigma/p_a a)$  when Henry's law applies at the interface;  $C_s$  is the concentration of the gas at saturation (the solubility);  $\sigma$  is the surface tension of the bubble-melt interface; and  $p_a$  is the ambient pressure; and  $R$  is the distance from the center of the bubble to the outer edge of the diffusional boundary layer surrounding the bubble.

The distance  $R$  was determined from the expression by Levich (78) for the form of the diffusion field around a bubble moving with the velocity  $V_o$ :

$$R = a + \sqrt{\frac{\pi}{3}} \left(\frac{aD}{V_o}\right)^{1/2} \sqrt{\frac{2+\cos\theta}{(1+\cos\theta)^2}} \quad (\text{IX-4})$$

This relation has the form one would expect for the diffusion layer surrounding a rising bubble, and is depicted in Fig. IX-1.

In order to solve Eqn. (1), the coordinates were transformed using the substitution

$$\rho(\theta, t) = (r - a(t))/(R(\theta, t) - a(t)) \quad (\text{IX-5})$$

Transforming the coordinates in this way simplifies the boundary conditions, as they become:

$$C(0, t) = C_0 \quad (\text{IX-6a})$$

$$C(1, t) = C_\infty \quad (\text{IX-6b})$$

In this way the diffusion layer can be divided into units which are constant as a function of angle in  $\rho$ - $\theta$  space. This makes the numerical solution of the differential equation and the application of the boundary conditions straightforward. It complicates the diffusion equation, however, so that the physical significance of each term is no longer clear. Specifically, the diffusion equation becomes:

$$\begin{aligned} \frac{\partial C}{\partial t} = & \frac{1}{R-a} \left\{ -\dot{a} + \rho S - V_r + \frac{1}{(R-a)+a} (V_\theta \rho U + 2D \right. \\ & + \frac{1}{(R-a)+a} (-a^2 \dot{a} - D \cot \theta \rho U - D \rho (W - \frac{2u^2}{R-a}))) \left. \frac{\partial C}{\partial \rho} \right. \\ & \left. - \frac{D \rho U}{(\rho(R-a)+a)^2} \frac{\partial^2 C}{\partial \theta \partial \rho} + \frac{D}{R-a} \frac{\partial^2 C}{\partial \rho^2} \right\} \quad (\text{IX-7}) \end{aligned}$$

or

$$\frac{\partial C}{\partial t} = A_1 \frac{\partial C}{\partial \rho} + A_2 \frac{\partial^2 C}{\partial \rho^2} + A_3 \frac{\partial^2 C}{\partial \theta \partial \rho} \quad (\text{IX-8})$$

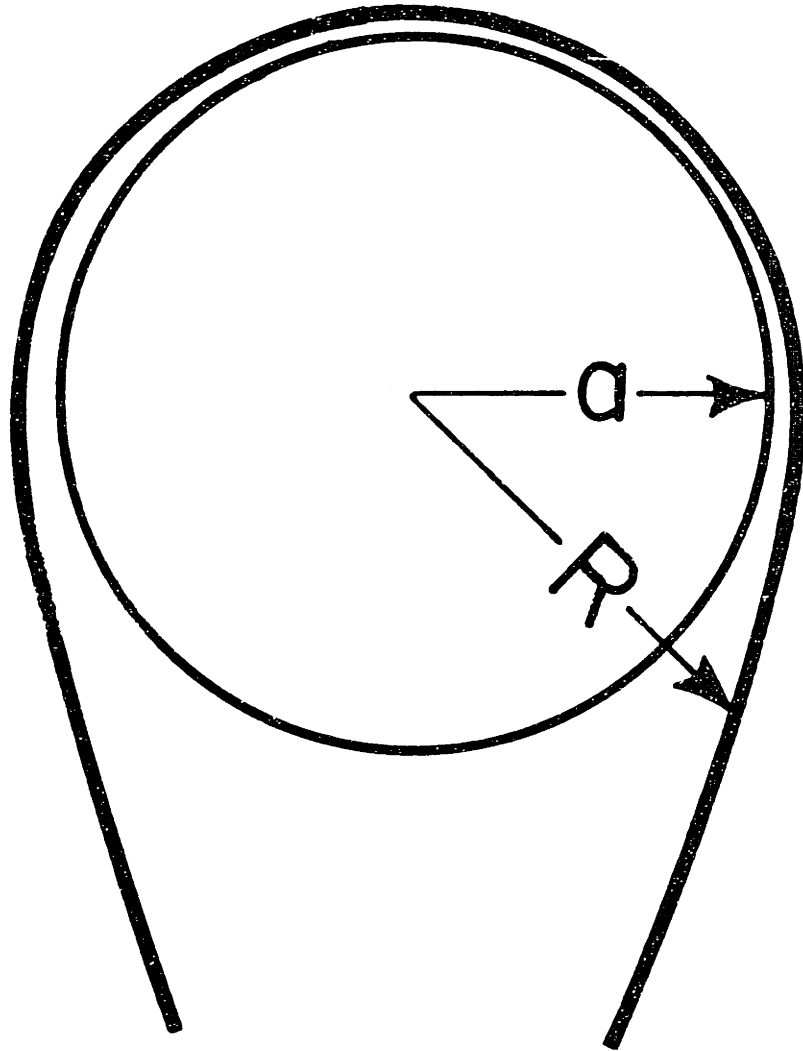


Figure IX-1 - Diffusion field for moving bubble according to Levich (78).



Here  $S$  is the time derivative of the boundary layer thickness; and  $U$  and  $W$  are, respectively, the first and second derivatives of the boundary layer thickness with respect to angle. These values can be calculated directly from the expression for  $R$ .

The initial conditions were such that the concentration of dissolved gas decreases exponentially from  $C_0$  at the interface to  $C_\infty$  at  $\rho(\theta, 0) = 1.0$ .

To determine the dissolution rate, the expression derived by Cable (56) was employed:

$$\frac{da}{dt} = \frac{3RTDa}{M(3ap_a + 4\sigma)} \left. \frac{\partial C}{\partial r} \right|_{r=a} \quad (\text{IX-9})$$

where  $R$  is the gas constant;  $T$  is the temperature; and  $M$  is the molecular weight of the gas. The gradient at the interface was multiplied by a weighting factor which is a function of  $\theta$ , and the flux was averaged over the surface of the bubble to determine the rate of shrinkage.

The concentration gradient at the interface, which is critical in determining the dissolution rate or growth rate, was evaluated from:

$$\left. \frac{\partial C}{\partial r} \right|_{r=a} = \frac{C(\Delta\rho, t) - C(0, t)}{(R-a)\Delta\rho} \quad (\text{IX-10})$$

A very steep concentration gradient was found near the interface. In the case of small bubbles ( $a \approx 0.05$  cm), it was therefore necessary to divide the distance from  $\rho = 0$  to  $\rho = 1$  into greater than 200 increments in order to describe accurately the slope at the interface ( $\partial C / \partial r \big|_{r=a}$ ). Since this required an unduly large amount of time, an exponential distribution of points was used, according to the following algorithm:

$$\rho_I = 1.0, \rho_{I-1} = 0.5\rho_I, \dots, \rho_2 = .5\rho_3, \rho_1 = 0$$

$$\Delta_I = \rho_{I+1} - \rho_I \quad (\text{IX-11})$$

In this way, the increments near the interface can be arbitrarily small. In the present work,  $I = 13$  was employed. For this,  $\Delta\rho_I = 2^{-11}$ , which gave the same results as constant increments of 0.002. To use this approach, it was necessary to derive the difference equations from the Taylor series expansion at a point for non-uniform spatial increments in one coordinate.

The difference analog to Eqn. (IX-8) is:

$$\begin{aligned} & \frac{C_{i,j,n}}{\Delta t} + A_3 \frac{(C_{i,j-1,n+1} - C_{i+1,j-1,n+1})}{\Delta\rho_i \Delta\theta} \\ & C_{i+1,j,n+1} \left( -\frac{A_1}{\Delta\rho_i + \Delta\rho_{i-1}} - \frac{2A_2}{\Delta\rho_i (\Delta\rho_{i-1} + \Delta\rho_i)} - \frac{A_3}{\Delta\rho_i \Delta\theta} \right) \\ & + C_{i,j,n+1} \left( \frac{2A_2}{\Delta\rho_{i-1} \Delta\rho_i} + \frac{A_3}{\Delta\rho_i \Delta\theta} + \frac{1}{\Delta t} \right) \\ & + C_{i-1,j,n+1} \left( \frac{A_1}{\Delta\rho_i + \Delta\rho_{i-1}} - \frac{2A_2}{\Delta\rho_{i-1} (\Delta\rho_{i-1} + \Delta\rho_i)} \right) \end{aligned} \quad (\text{IX-12})$$

The boundary conditions were applied, and the resulting set of simultaneous equations were solved by standard numerical methods on an IBM370-168. Since Eqn. (IX-12) or its analogue, Eqn. (IX-13) is nonlinear, it was necessary to iterate the process to determine the solution to the diffusion equation.

The solubility of the gas in the glass was taken as that used by Cable (56)  $3 \times 10^{-4}$  wgt.pct. This is appropriate for the dissolution

of oxygen in a soda-lime-silicate glass, although little is known about the temperature dependence of  $C_s$ . Values for the diffusivity and viscosity as functions of temperature, also appropriate for oxygen and a soda-lime-silicate glass, were taken from Doremus (108).

### B. Analytical Models

Two analytical expressions may be derived to describe the dissolution of a gas bubble in a glass melt. Both models use the results of Levich (78) to describe the diffusional flux at the surface of the bubble, and ignore the flux due to the moving boundary as the bubble shrinks. Levich assumed that the thickness of the diffusional layer,  $\delta$ , is small compared with the size of the bubble,  $a$ , and derived the following expression for the flux:

$$j = D \left( \frac{\partial C}{\partial r} \right) = - \left( \frac{DV_o}{a} \right)^{1/2} \sqrt{\frac{3}{\pi}} \sqrt{\frac{(1+\cos\theta)^2}{2+\cos\theta}} (C_o - C_\infty) \quad (\text{IX-13a})$$

or

$$j = - \frac{D(C_o - C_\infty)}{\delta(a)\delta(\theta)} \quad (\text{IX-13b})$$

where

$$\delta(a) = \left( \frac{\pi Da}{3V_o} \right)^{1/2} = \left( \frac{\pi D \eta}{\rho_{gl} g a} \right)^{1/2} \quad (\text{IX-14a})$$

$$\delta(\theta) = \sqrt{\frac{(1+\cos\theta)^2}{2+\cos\theta}} \quad (\text{IX-14b})$$

and  $C_o$  is the concentration at the interface and  $C_\infty$  is the concentration in the bulk melt. An average value for  $\delta(\theta)^{-1}$  over the surface of the bubble is determined numerically:

$$\delta^{-1} = \frac{1}{N} \sum_{i=1}^N \frac{\sin\theta}{2\delta(\theta_i)} \quad (\text{IX-15})$$

The expression obtained by Levich describes the flux due to the concentration gradient at the surface of the bubble. Using simple mass balance relations, Cable (56) derived an expression which relates the flux at the bubble-melt interface to the rate at which a bubble will grow or shrink:

$$j = \frac{1}{3a^2} (3a^2 \rho_o + 2a\tau) \frac{da}{dt} \quad (\text{IX-16})$$

where

$$\rho_o = \frac{Mp_a}{RT} \quad (\text{IX-17a})$$

and

$$\tau = \frac{2M\sigma}{RT} \quad (\text{IX-17b})$$

If one equates the expression derived by Levich, which describes the flux at the interface due to concentration gradients in the melt, with the expression of Cable for the effect of that flux on the size of the bubble, one obtains for the shrinkage rate:

$$\frac{da}{dt} = \frac{Ka^{3/2}(C_o - C_\infty)}{ap_a + 4\sigma/3} \quad (\text{IX-18})$$

where

$$K = \frac{RTD^{1/2}}{M} \left( \frac{\rho g}{\pi\eta} \right)^{1/2} \frac{1}{\delta(\theta)^{-1}} \quad (\text{IX-19})$$

Two suggestions (72, 56) have been made concerning the concentration of dissolved gas at the bubble-melt interface. Each of these models may be combined with Eqn. (IX-18) to derive expressions for the rate of shrinkage of a bubble and for the time it takes to dissolve completely.

The first view (72) considers that the gas concentration at the bubble-melt interface is constant. If it is assumed that the melt is

saturated at the interface, i.e.,  $C_o = C_s$ , Eqn. (IX-18) becomes:

$$\frac{da}{dt} = - \frac{Ka^{3/2} (C_s - C_\infty)}{ap_a + 4\sigma/3} \quad (\text{IX-20})$$

Rearranging this expression and integrating from the initial bubble radius  $a_o$  to 0, one obtains the time for a bubble to dissolve as:

$$t = \frac{(C_s - C_\infty)}{K} \int_0^{a_o} \frac{ap_a + \frac{4}{3}}{a^{3/2}} da \quad (\text{IX-21a})$$

Upon integrating,

$$t = \frac{(C_s - C_\infty)}{K} \left( \frac{p_a a^{1/2}}{2} - \frac{2\sigma}{3} a^{-1/2} \right)_{a=0}^{a=a_o} \quad (\text{IX-21b})$$

This expression cannot be evaluated at the lower boundary, but Eqn.

(IX-21a) can be evaluated numerically. This approach was used in the present work.

The second view of the gas concentration at the bubble-melt interface (56) considers that Henry's law applies at the interface. That is:

$$C_o = \left( 1 + \frac{2\sigma}{p_a a} \right) C_s \quad (\text{IX-22})$$

Expressing the bulk concentration as a fraction  $x$  of the saturation value and combining Eqns. (IX-18) and (IX-22), one obtains for the rate of shrinkage:

$$\frac{da}{dt} = - KC_s a^{1/2} \frac{\left( \frac{2\sigma}{p_a} + (1-x)a \right)}{ap_a + \frac{4\sigma}{3}} \quad (\text{IX-23})$$

Rearranging and integrating (in this case, the integral can be evaluated at both  $a=a_o$  and  $a=0$ ), the time for a bubble to dissolve may be expressed:

$$t = \frac{2}{KC_s} \left\{ \frac{p_a \sqrt{a}}{1-x} + \sqrt{\frac{2 p_a}{1-x}} \left( \arctan \sqrt{\frac{(1-x) p_a}{2\sigma}} \right) \left( \frac{2}{3} - \frac{1}{1-x} \right) \right\} \quad (\text{IX-24})$$

The times to dissolve as calculated by Eqn. (IX-21) and by Eqn. (IX-24) are very close. For example, a bubble of initial radius 1.0 mm. with  $x = 0.9$  at  $1400^\circ\text{C}$  dissolves in 1040 seconds according to Eqn. (IX-21) and in 1044 seconds according to Eqn. (IX-24). Both of these analytical models indicate a dissolution time which is longer than that calculated by numerical solutions to the diffusion equation which take account of the effect of the moving boundary.

### C. Results

Fig. IX-2 shows how a bubble, initially 0.1 cm. in radius, shrinks as a function of time at several temperatures and under two levels of gravitational force (two velocities for a given size). Raising the temperature decreases the time to dissolve, at least for a constant 995 solubility, which is in accord with the results of Greene and Kitano (57). In each case, the ratio of  $C_\infty$  to  $C_s$  was 1.0, and it was assumed that Henry's law applies at the interface. For  $C_\infty/C_s = 1$ , the rate of dissolution increases as the bubble size decreases. With no convection, bubbles under these conditions would rise to the surface of a tank 4 feet deep before they dissolve. The time to dissolve under different initial conditions is shown in Table IX-1. When  $C_\infty/C_s = 1.0$ , it takes less time for a 0.1 cm bubble to rise to the surface than for a bubble half that size to dissolve.

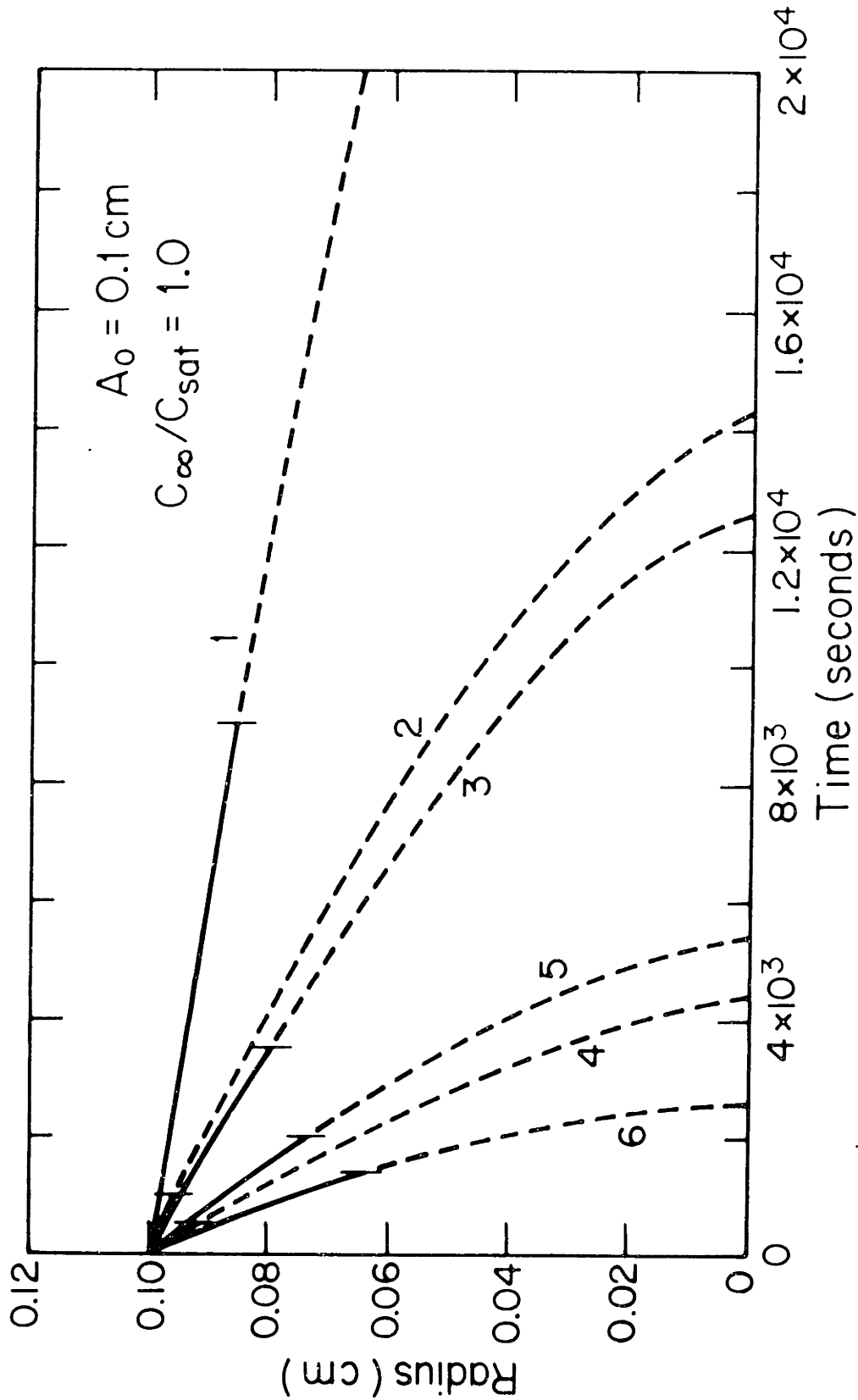


Figure IX-2 - Radius of bubble (initially 0.1 cm) as a function of time  $C_\infty / C_s = 1.0$ . Dashed lines indicate bubble would rise to surface before dissolving completely (1) 1200 C, gravity = 1g; (2) 1400 C, gravity = 1g; (3) 1500 C, gravity = 1g; (4) 1300 C, gravity = 10g; (5) 1400 C, gravity = 10g; (6) 1500 C, gravity = 10g.

Table IX-1

Calculated Dissolution Times for Oxygen Bubbles in  
Soda-Lime-Silicate Melts Under Several Sets of  
Conditions

<u>Boundary Condition</u>	<u>Initial Radius (cm)</u>	<u><math>C_{\infty}/C_s</math></u>	<u>Temperature (°C)</u>	<u>Gravity</u>	<u>Time to Dissolve (sec.)</u>			
1	0.10	1.0	1200	1	$4.2 \times 10^4$			
				10	$1.4 \times 10^4$			
			1300	1	$1.25 \times 10^4$			
				10	$4.5 \times 10^3$			
			1400	1	$5.5 \times 10^3$			
				1	$2.65 \times 10^3$			
			1	0.10	0.9	1200	1	$4.2 \times 10^3$
							10	$1.4 \times 10^3$
						1300	1	$1.3 \times 10^3$
							10	450
1400	1	540						
	1	260						
2	0.10	0.9	1300	1	1650			
				1	650			
				1	300			

In the column indicating boundary condition, 1 = Henry's Law applies at the interface; 2 = the concentration at the interface is constant and saturated.



Table IX-1 (Cont'd)

<u>Boundary Condition</u>	<u>Initial Radius (cm)</u>	<u><math>C_{\infty}/C_s</math></u>	<u>Temperature (<math>^{\circ}\text{C}</math>)</u>	<u>Gravity</u>	<u>Time to Dissolve (sec.)</u>
1	0.01	1.0	1200	1	650
				10	290
			1300	1	160
				10	93
				1	70
				1	35
1	0.01	0.9	1200	1	250
				10	130
			1300	1	80
				10	43
				1	26
				1	13
2	0.01	0.9	1300	1	170
			1400	1	60
			1500	1	28

If the ratio of  $C_{\infty}$  to  $C_s$  is decreased slightly to 0.9, the rate of dissolution increases substantially, so even a large bubble dissolves before it reaches the surface (Fig. IX-3). Changing the concentration of gas in the bulk changes the shape of the curve describing the size of the bubble as a function of time. When the bubble and its velocity are large and the driving force for dissolution is large, as with a small  $C_{\infty}/C_s$ , the bubble dissolves at a high rate and the rate decreases as the bubble size and velocity decrease until the bubble is small. For small bubbles (Fig. IX-4), when  $C_{\infty}/C_s$  is decreased to 0.9, the effect of increased solubility at the interface due to Henry's law is so great that the dissolution rate increases as the bubble size decreases.

If the curves describing the dissolution of 0.1, 0.05 and 0.01 cm. bubbles are compared, they superimpose very well over the range of common sizes. This indicates that the initial conditions used in the present analysis are realistic. More importantly, the history of a bubble is not significant in predicting its path to dissolution. The use of Levich's expression for the boundary layer thickness is most accurate for large bubbles where the diffusion layer is small compared with the size of the bubble. Hence this should not be a source of error in describing the shrinkage of large bubbles.

An increase in gravity by a factor of 10, as by centrifugation, increases the rate of dissolution by about a factor of 3; and the effect is the same for large and small bubbles. In glassmaking processes using centrifugation as a method of increasing the rate of fining, the distance a bubble must travel to reach the surface is much smaller than in

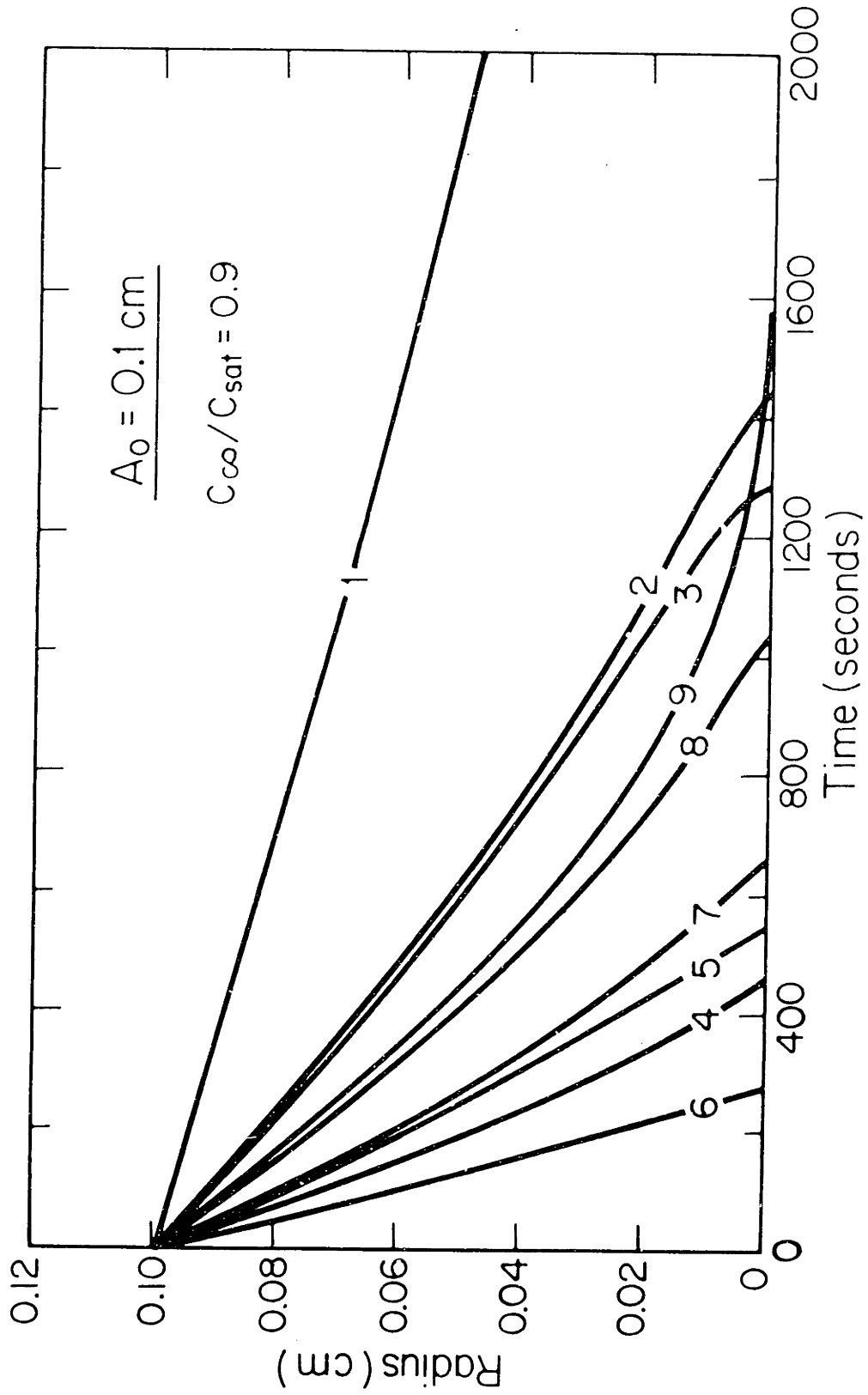


Fig. IX-3 - Radius of bubble (initially 0.1 cm) as a function of time,  $C_{\infty} / C_s = 0.9$ . (1) 1200 C, gravity = 1g; (2) 1200 C, gravity = 10g; (3) 1300 C, gravity = 1g; (4) 1300 C, gravity = 10g; (5) 1400 C, gravity = 1g; (6) 1500 C, gravity = 1g; (7) 1400 C,  $C_0 - C_s$ ; (8) 1400 C, Eq. IX-23; (9) 140. C, Eq. IX-20.

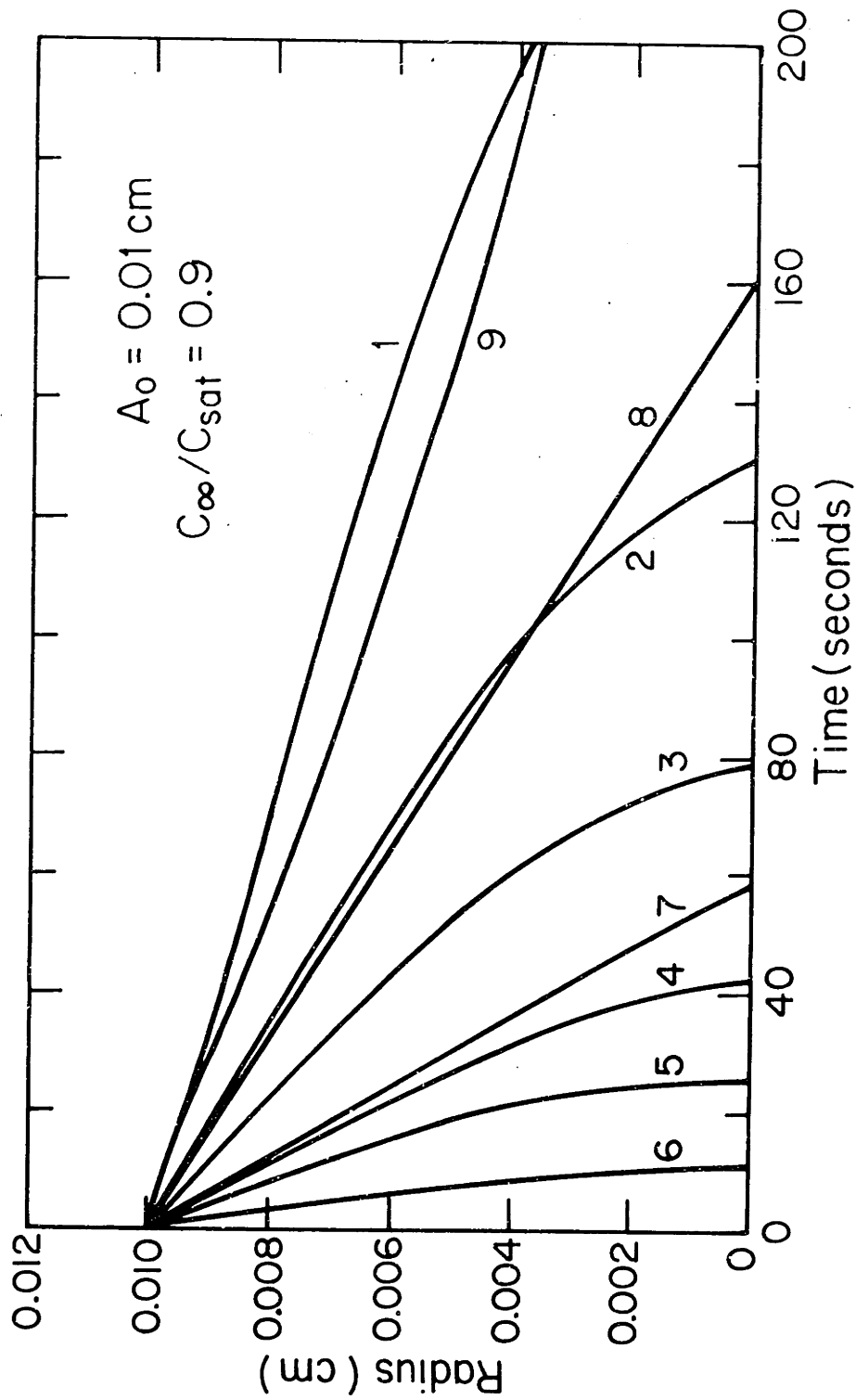


Figure IX-4 - Radius of bubble (initially 0.01 cm) as a function of time.  
 $C_\infty / C_s = 0.9$ . (1) 1200 C, gravity = 1g; (2) 1200 C, gravity = 10g; (3) 1300 C, gravity = 1g; (4) 1300 C, gravity = 10g; (5) 1400 C, gravity = 1g; (6) 1500 C, gravity = 1g; (7) 1400 C,  $C_0 - C_s$ ; (8) 1400 C, Eq. IX-23; (9) 1400 C, Eq. IX-20.

conventional processes, but the residence time is likewise much smaller. Large bubbles would have no trouble in reaching the surface in a short time. This is not the case with very small bubbles, however, particularly if the  $C_{\infty}/C_s$  ratio is not favorable. Further calculations show that if the gas solubility is decreased by a factor of 10, the time to dissolve is increased by about a factor of 10.

Figs. IX-3 and IX-4 also show the respective paths to dissolution for 0.01 and 0.1 on bubbles at 1400°C according to several solutions of the moving bubble problem. The model which assumes that Henry's law applies at the interface and numerically solves the diffusion equation indicates a high dissolution rate. Assuming a constant, saturated concentration at the interface decreases the dissolution rate, particularly for small bubbles. Eqn. (IX-3), which assumes Henry's law at the interface, indicates a dissolution rate that is substantially slower than if the diffusion equation is solved directly. If the concentration is constant at the interface, Eqn. (IX-20) indicates a very slow dissolution rate, particularly for very small bubbles.

Considering now the growth of gas bubbles in glass melts, the times required for a bubble to grow to a radius of  $2A_0$  and  $4A_0$  are shown in Table IX-2. Here  $A_0$  is the initial radius of the bubble. Table IX-2 also shows the time required for a bubble to rise a given distance above its initial position, and the size it has attained at that time. Fig. IX-5 shows the increase in bubble radius as a function of time. As the bubbles grow, their velocity increases; and this in turn increases their rate of growth. The effect of using a condition of Henry's law rather than

Table IX-2  
The Growth of Oxygen Bubbles in Soda-Lime-Silicate Melts  
Under Several Sets of Conditions

Condition	Initial Radius $A_0$	$C_\infty/C_s$	Time (sec.) to grow to		5 cm.		130 cm.			
			$2A_0$	$4A_0$	t (sec)	A (cm)	t (sec)	A (cm)		
			$2A_0$	$4A_0$	t (sec)	A (cm)	t (sec)	A (cm)		
1	.01	1.1	160	285	485	.064	1050	.145	1400	.203
2	.01	1.1	115	325	490	.059	1040	.143	1360	.207
1	.01	1.2	74	197	352	.074	698	.181	900	.265
2	.01	1.2	60	172	328	.076	662	.182	860	.266
1	.10	1.1	555	-	56	.108	360	.161	640	.216
2	.10	1.1	530	-	56	.109	360	.164	630	.220
1	.05	1.1	400	955	180	.07	670	.145	1000	.205
2	.05	1.1	365	900	170	.072	640	.147	960	.209
2	.001	1.1	3.9	40	600	.056	1230	.135	1600	.192
2*	.01	1.1	47	122	113	.037	252	.090	330	.13
2	.01	1.05	226	640	750	.046	1680	.109	2220	.157
2**	.01	1.1	50	148	290	.077	540	.165	700	.233
2**	.10	1.1	260	-	40	.113	210	.180	360	.239

In the column indicating boundary condition, 1 = Henry's Law applies at the interface, 2 = the concentration at the interface is constant and saturated. All calculations are at 1400 C and gravity = 1 g unless otherwise indicate.

\* gravity = 10g

\*\* Temperature = 1500°C

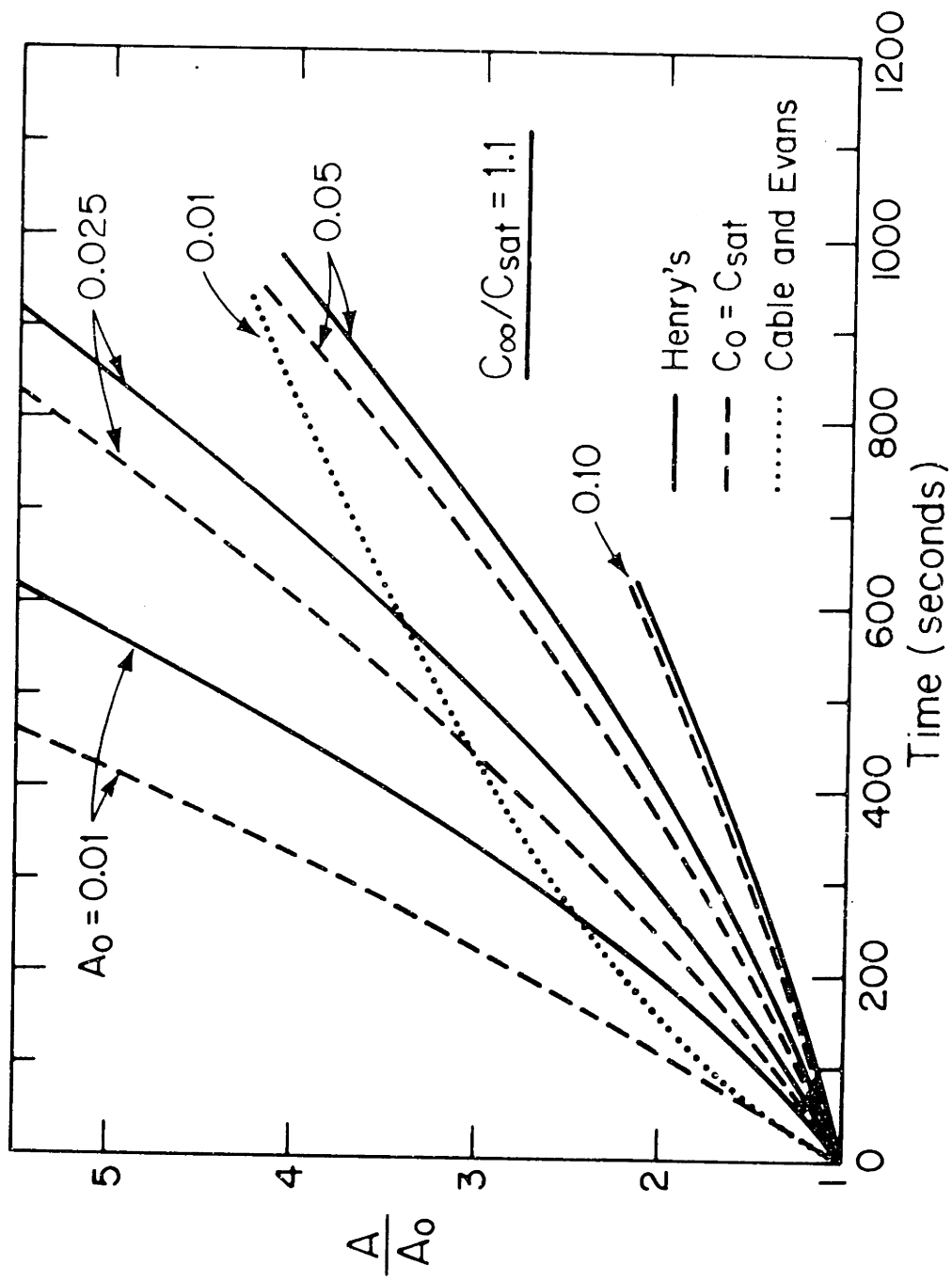


Figure IX-5 - Radius of growing bubble as a function of time at 1400 C.

a constant composition at the interface is found to have a sizable effect on the growth rate only for very small bubbles (see the times required for the bubbles to grow to  $2A_0$  and  $4A_0$ ). Since small bubbles rise slowly, the time required for a bubble to rise a given distance (as 5 cm. or 150 cm.) is not appreciably affected by the assumption that Henry's law applies at the interface. The size reached by a bubble when it has risen a given distance in the melt does not vary significantly for bubbles of significantly different initial sizes.

When  $C_\infty/C_s$  is increased, the time required for a bubble to rise a given distance decreases, and the radius reached at that distance increases. Increasing gravity by a factor of 10 increases the rate of growth of the bubbles by about a factor of 3; and decreases the time to move a given distance by about a factor of 4. Fig. IX-6 shows the distance risen by a bubble as a function of time, for several values of initial radius and  $C_\infty/C_s$ . It is seen that long times are required for small bubbles to grow sufficiently to rise even 1 cm.

#### D. Discussion

Several factors are important in determining the time required for a bubble to dissolve (or the rate at which it grows). Among these factors are: the relative saturation of the melt at various temperatures (which depends on the relative saturation prior to fining and on the change of glass solubility with temperature); the diffusion coefficient of the gas in the melt and the viscosity of the melt (which in turn depend on temperature); the driving force for bubble motion (gravity or mechanical forces); the size of the bubble; and the condition on gas concentration



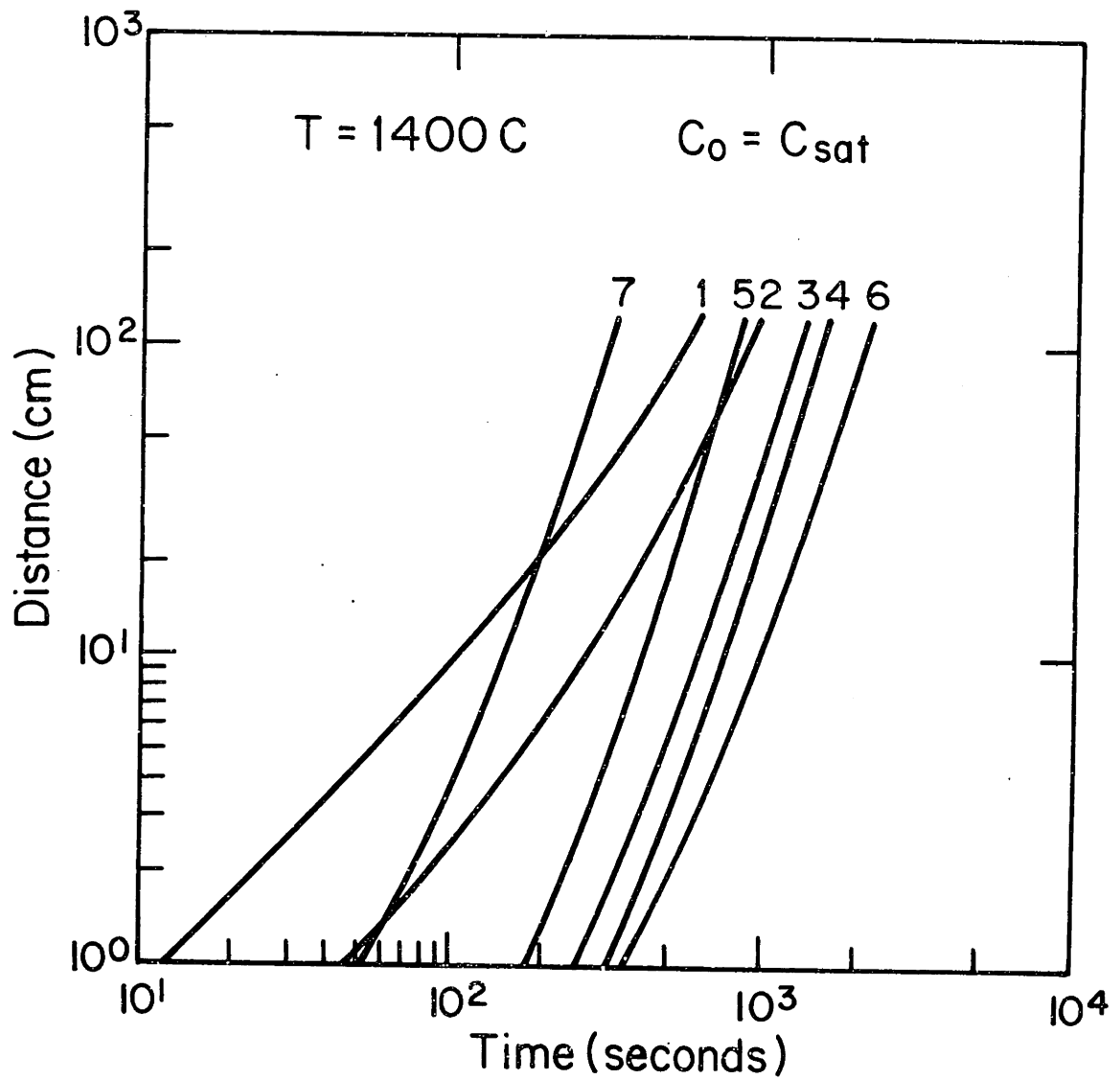


Figure IX-6 - Height a growing bubble has risen as a function of time.

(1)  $A_0 = 0.1$  cm,  $C_\infty/C_s = 1.1$ ; (2)  $A_0 = 0.05$  cm,  $C_\infty/C_s = 1.1$ ; (3)  $A_0 = 0.01$  cm,  $C_\infty/C_s = 1.1$ ; (4)  $A_0 = 0.001$  cm,  $C_\infty/C_s = 1.1$ ; (5)  $A_0 = 0.01$  cm,  $C_\infty/C_s = 1.2$ ; (6)  $A_0 = 0.01$  cm,  $C_\infty/C_s = 1.05$ ; (7)  $A_0 = 0.01$  cm,  $C_\infty/C_s = 1.1$ , gravity =  $10g$ .

at the bubble-melt interface.

If the results shown in Table IX-1 are compared graphically (Fig. IX-7), it can be seen how a slight increase in the concentration of gas dissolved in bulk melt increases the time required for a bubble to dissolve. For example, assuming Henry's law at the interface, a 0.1 cm. bubble in a melt with a  $C_{\infty}/C_s$  ratio of 0.8 at 1200 C takes the same time to dissolve as a 0.1 cm. bubble in a melt with a  $C_{\infty}/C_s$  ratio greater than 0.99 at 1500 C. The effect of increasing the gas concentration (relative to saturation) in the melt is smaller for small bubbles than for large bubbles.

Assuming a constant concentration equal to the solubility limit at the interface results in dissolution times which are longer than if Henry's law is assumed. At  $C_{\infty}/C_s$  values greater than 0.9, the differences in results obtained by using the two assumptions are substantial. To illustrate the differences which the two assumptions can make, consider the case where  $C_{\infty}/C_s = 1.0$ . If Henry's law applies for this case, a bubble will dissolve; while if the concentration at the interface is constant, the bubbles size will be stable. If  $C_{\infty}/C_s$  is slightly greater than 1.0, the bubble would still dissolve if Henry's law applies, while growth of the bubble would occur if the concentration at the interface is constant. If Henry's law applies, the concentration of dissolved gas in the glass is greater than the saturated concentration (solubility limit) after the bubble dissolves. Because the free energy required to form a melt-gas interface in nucleating a bubble, the supersaturated solution could be stable for long periods of time.

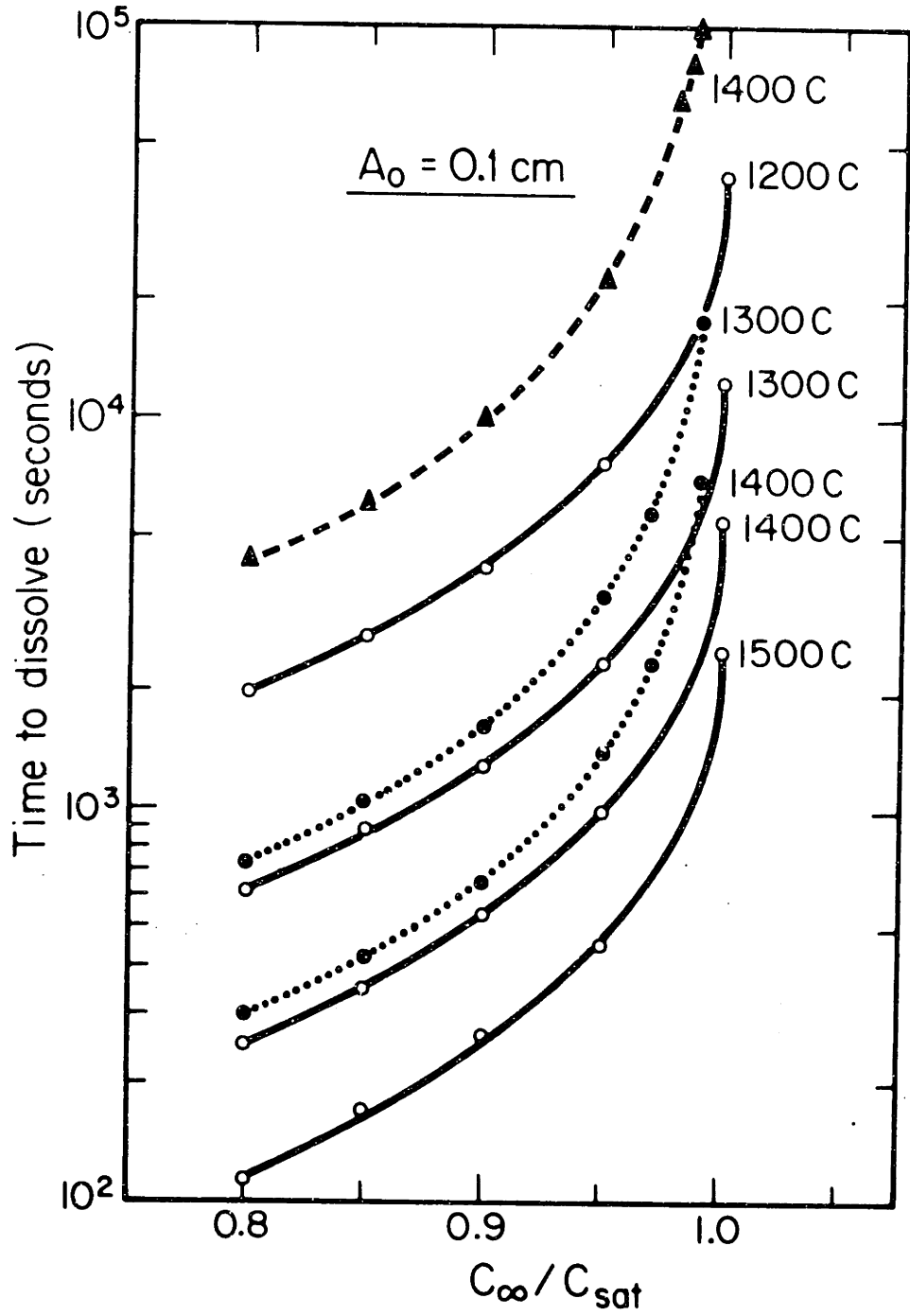


Figure IX-7 - Time to dissolve vs.  $C_{\infty}/C_s$ . Solid lines - Henry's Law at interface; dotted lines -  $C_o=C_s$  at interface; dashed line - stationary bubble according to Cable and Evans.

An increase in temperature for a given  $C_{\infty}/C_s$  results in a large decrease in the dissolution time. In practice, maintaining the melt at a high temperature is often not the solution to fining problems; and raising the temperature of an initially-cooled (and even refined) melt can result in the reboil phenomenon which is too often observed in sulfate-containing melts. Lacking data on the solubility of oxygen in a soda-lime-silicate melt as a function of temperature, we have assumed it to be constant in considering the temperature dependence of the dissolution rate. Since the dissolution rate depends strongly on the  $C_{\infty}/C_s$  ratio, it seems highly desirable to obtain data on the solubility in glass melts of oxygen and other gases of interest (particularly nitrogen) as a function of temperature--as well as data on the actual concentrations of gases in the melts. Available information indicates that  $C_{\infty}$  and  $C_s$  can be affected by the presence of refining agents in the melt (18, 19, 56), as well as by changes in the melt composition.

Comparing the time to dissolve for bubbles of different radii (Fig. IX-6) with the corresponding times obtained by Cable and Evans (75), it is found that motion of a bubble can significantly increase its rate of dissolution, and that the effects of motion in decreasing dissolution time are greater for large bubbles. Physically, the increase in dissolution rate reflects motion of the bubble away from its associated diffusion field into regions of relatively low concentrations of gas.

The previous estimates of dissolution times for stationary bubbles with which the present results are compared did not allow for the flux due to the moving boundary. As the bubble shrinks, the diffusing gas

must move in a direction opposite to that of the inward flux of the melt. This increases the distance which the gas must travel, and thus increases the dissolution time. Since small bubbles dissolve at a higher rate than large bubbles, the effect of the moving boundary is greater for small bubbles than for large ones. The fact that large moving bubbles take less time to dissolve than large stationary bubbles, in spite of the inclusion of the flux due to the moving boundary, accentuates the importance of bubble motion on dissolution rate.

Experimentally, Greene (53) showed that if a large bubble ( $a_0 > 0.05$  cm) is allowed to rise through a melt, its dissolution rate increases by an order of magnitude over the rate at which a stationary bubble dissolves. For example, the time required at 1400 C for a 0.1 cm bubble to dissolve increases an order of magnitude from 540 sec to 5500 sec when  $C_\infty/C_s$  is increased from 0.9 to 1.0. Under the same conditions, the time required for a 0.01 cm bubble to dissolve increases by only a factor of 2.7, from 26 sec to 70 sec. This agrees very well with the results shown in Fig. IX-7.

The effect of Henry's law on the dissolution time is not large for large bubbles (Fig. IX-8). For a 0.1 cm. bubble, the concentration at the interface is increased by only about 0.6%. For a 0.01 cm. bubble, however, the concentration at the interface is increased by about 6%. This has the same effect as decreasing  $C_\infty/C_s$  by a similar amount. Accordingly, the difference between the dissolution times calculated by the two models is large for small bubbles ( $a_0 \leq 0.025$  cm.).

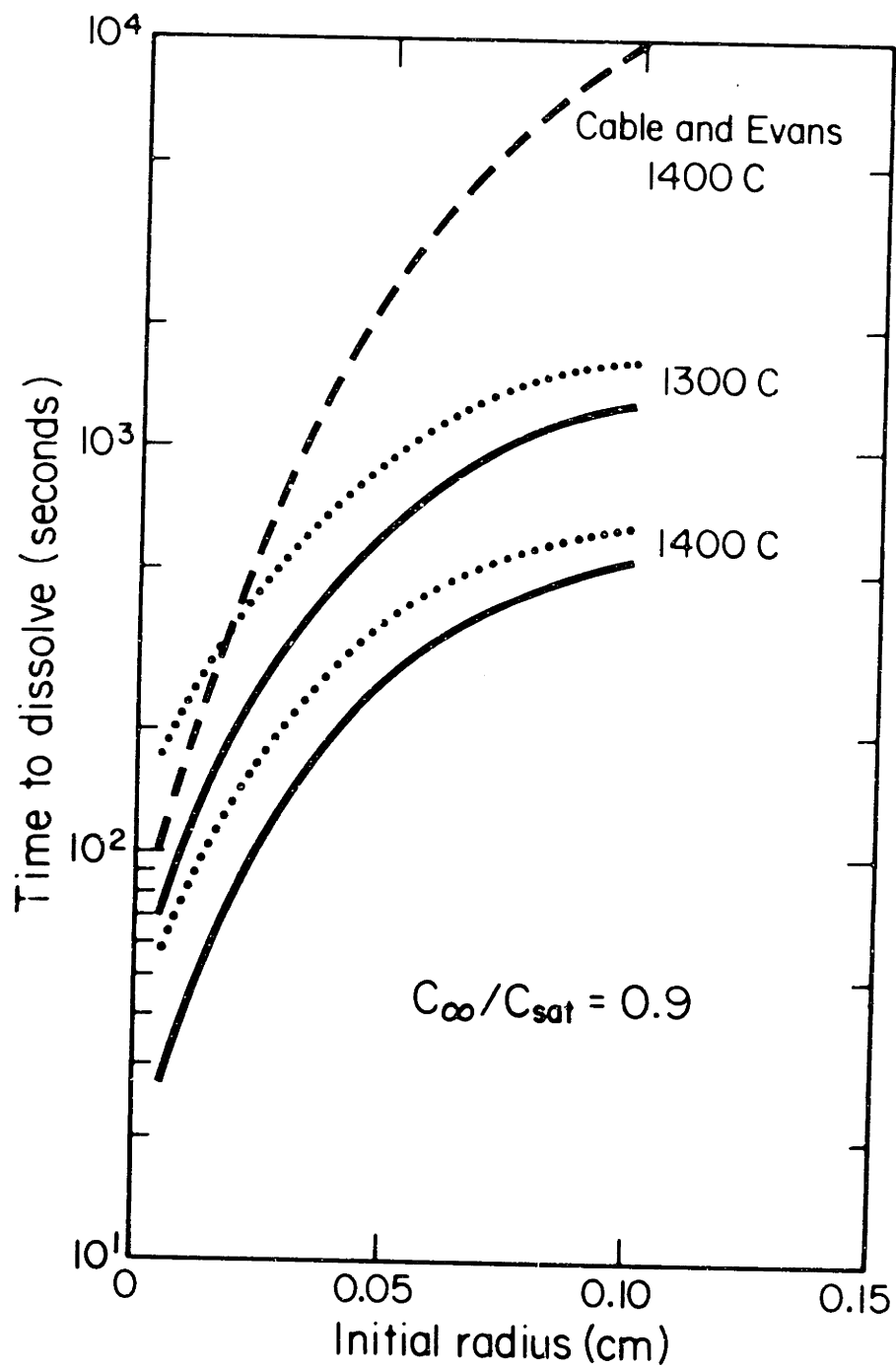


Figure IX-8 - Time to dissolve vs. initial radius. Solid lines - Henry's Law at interface; dotted lines -  $C_o - C_s$  at interface; dashed lines - stationary bubble according to Cable and Evans.

The velocity at which small bubbles rise through the melt is quite small; and hence the analysis for a stationary bubble should provide an appropriate description, at least under velocities calculated for normal gravitational forces. The diffusion layer around a bubble should approach a spherical shape as the bubble size and the bubble velocity approach zero. The solution due to Levich from which the shape of the diffusion field is derived assumes that the thickness of the diffusion layer is small compared with the size of the bubble. This solution provides a close description of the boundary layer for large bubbles ( $a_0 \geq 0.1$  cm.); but the accuracy of the description begins to limit the results for smaller bubbles ( $a_0 < 0.01$  cm.). Increasing the velocity of bubble motion (as by increasing gravity) serves to restore the applicability of the description to small bubbles by decreasing the thickness of the diffusion field, and by distorting the diffusion field from sphericity.

When a bubble grows, the effect of its motion (rising) through the melt cannot be ignore. Unlike the case of a shrinking bubble, in which the effect of the bubble motion decreases as time progresses (as its velocity decreases), the effect of the motion of a growing bubble on its size increases with time. Initially, the growth of a small stationary bubble, as  $A_0 = 0.01$  cm, is similar to the growth of a small rising bubble (Fig. IX-5). Before the bubble has doubled in radius, however, the results start to diverge. The time for a small bubble to quintuple in radius at  $1200^\circ\text{C}$  is 1400 sec--which is larger than that for a moving bubble by a factor of about 3.3. For larger bubbles, the effect is even greater. For example, a stationary 0.05 cm. bubble doubles its radius at  $1200^\circ\text{C}$

in 3500 sec., while a moving bubble at the same temperature doubles its radius in 350 sec.

Increasing the gravity as by centrifugation increases the rate of dissolution in two ways: First, it directly increases the velocity of the bubble; and secondly, by increasing the growth rate it increases the acceleration of the bubble rising through the melt. The growing bubble rises at an accelerating velocity so that it rapidly moves away from its diffusion field into a region in which the dissolved gas is not depleted. An increase in the dissolved gas content of the melt increases the rate at which bubbles disappear by causing them to grow faster, with a concomitant increase in the rate of their rise to the surface.

Under comparable conditions of supersaturation and undersaturation ( $C_{\infty}/C_s = 0.9$  or  $1.1$ ), the time required at  $1400^{\circ}\text{C}$  for a 0.1 cm. bubble to grow and rise to the surface of a 4 ft deep tank is the same as for it to dissolve, about 640 sec. For smaller bubbles, as  $A_0 = 0.01$  cm, the time to dissolve decreases to about 55 sec. while the time to rise to the surface increases to about 1300 sec. At  $1500^{\circ}\text{C}$ , the time required for a 0.1 cm. bubble to grow and rise to the surface of a 4 ft. deep tank (350 sec.) is greater than it is to dissolve (260 sec.). For smaller bubbles, as  $A_0 = 0.01$  cm, the time to dissolve decreases to about 28 sec. while the time to rise to the surface is about 700 sec. This assumes that the oxygen solubility in the melt is constant. In a large glass tank the problem is complicated by the non-isothermal conditions which cause convection as well as variations in the gas solubility.



bubble-melt interface--whether Henry's law or a constant concentration-- can have a significant effect on the dissolution time, particularly for small bubbles or under conditions where the concentration of gas in the melt is close to the solubility limit.

In a supersaturated melt, moving bubbles grow much more rapidly than stationary bubbles, with the increased growth rate becoming more significant as time progresses (as the bubbles grow in size). Increasing the velocity of bubble motion through the melt, as by increasing gravity, can increase substantially the rate of growth of the bubbles. The condition used to describe the concentration of gas at the interface does not have a significant effect on the rate of disappearance of bubbles by rising to the surface of the melt.

In toto, the present analysis offers the prospect for describing in detail the growth and dissolution of gas bubbles in glass melts. To take full advantage of the analysis, it will be necessary to obtain data on the solubility of gases (particularly oxygen and nitrogen) in glass melts as a function of temperature, as well as further sampling of gas concentrations at various stages of the melting process and various conditions of melting.

Convection has two principal effects on the process of fining besides its effect on homogenization, and hence on gas solubility. Specifically, convection can provide motion of gas bubbles with respect to regions of the melt, and can provide a longer residence time of the bubbles in the melt. The overall effect of convection is to increase the importance of dissolution relative to motion to the surface in eliminating gas bubbles from glass tanks.

### E. Conclusions

In this chapter the effects of bubble motion on the dissolution rate and growth rate of gas bubbles in glass melts has been investigated. It has been found that such motion can have a profound influence on the rates of dissolution and growth. The dissolution time for bubbles with an initial radius of 0.1 cm. moving under the force of gravity is smaller by more than an order of magnitude than the dissolution time for stationary bubbles of the same initial size. Increasing the rate of motion of the bubbles, as by centrifugation, can further increase the rate of dissolution.

The dissolution time can be dramatically decreased by decreasing the  $C_{\infty}/C_s$  ratio--that is, by decreasing the concentration to dissolved gas in the melt, or by increasing the solubility of the gas. Changes as small as 20% in the  $C_{\infty}/C_s$  ratio can change the dissolution time by a factor as large as 20. This effect is more pronounced for large bubbles than for small bubbles.

The condition used to describe the concentration of gas at the

## X. SUGGESTIONS FOR FURTHER WORK

The effect of changing the concentration of nucleating heterogeneities should be investigated. Crystallization statistics should be extended to include nucleating heterogeneities with the object of predicting the grain size distribution in partially crystalline bodies with complex thermal histories.

Semi-empirical models of viscosity (109, 110) should be applied to the simplified method for predicting critical cooling rate for glass formation. Measurements of heat of fusion for lunar samples would also aid in the refinement of this method. Correlations between nucleation barriers suggested by the simplified method, by measurement of the crystallization temperature upon reheating and crystallization statistics, and by direct measurement of the nucleation frequency should be examined.

The first stage cooling model by Simonds should be extended to take into account melting kinetics and three dimensional heat flow. The second stage cooling model should be extended to take into account convection.

More measurements of diffusion and solute partitioning in mineral systems should be made. Both solute partitioning and homogenization could be used for a wide range of compositions if this data were known. The model which describes homogenization within a grain should be extended to include solidification from the melt with diffusion in the liquid and the solid and effects of the moving boundary.

Models for the growth and the dissolution of gas bubbles in glass should be extended to include more than one bubble. The gas solubility

as a function of temperature and composition must be determined, as well as the dissolved gas concentration in actual melts. The model should be combined with existing models of commercial glass melting tanks to more realistically describe forces and flows.

APPENDIX ASOURCES OF VISCOSITY AND GROWTH RATE DATA

<u>Composition</u>	<u>Viscosity Reference</u>	<u>Growth Rate Reference</u>
15418	111	112
50095	113	113
70019	112	112
65016	113	113
79155	112	112
67975	114	114
14259	115	116
14310	115	116
15555	111	111
68502	111	-
74220	113	-
15498	117	117
15286 Intrusion	117	117
Anorthite	118	119
$\text{Na}_2\text{O} \cdot 2\text{SiO}_2$	120	120
Salol	84	121
o-terphenyl	84	121

APPENDIX BTHE THOMAS TRIDIAGONAL METHOD

The equations are:

$$a_i u_{i-1} + b_i u_i + c_i u_{i+1} = d_i$$

$$\text{for } 1 \leq i \leq R$$

$$\text{with } a_1 = c_R = 0$$

The algorithm is as follows:

First, compute

$$\beta_i = b_i - \frac{a_i c_{i-1}}{\beta_{i-1}} \quad \text{with } \beta_1 = b_1$$

$$\gamma_i = \frac{d_i - a_i \gamma_{i-1}}{\beta_i} \quad \text{with } \gamma_1 = \frac{d_1}{b_1}$$

The values of the dependent variable are then computed from

$$u_R = \gamma_R \quad \text{and} \quad u_i = \gamma_i - \frac{c_i u_{i+1}}{\beta_i}$$

This algorithm is taken from von Rosenberg (91).

APPENDIX C  
INTERDIFFUSION COEFFICIENTS IN OLIVINE

Experiments have been conducted by Buening and Buseck (43) and Misener (42) to determine interdiffusion coefficient data for Fe and Mg in olivine. Buening and Buseck used a crystal of one composition and a powder of another to make their diffusion couple; Misener used two crystals of different compositions placed together. In such experiments, the question of the quality of the grain-to-grain contacts is always present.

The diffusion data to be reported below are derived from experimentation wherein two different compositions, with the same crystallographic orientation, are placed in contact to form a diffusion couple. After annealing at a given temperature and  $FO_2$  for a predetermined time, the compositional profile across the boundary of the two phases is measured using an electron microprobe. This profile is subjected to the Boltzmann-Matano solution (Crank, 1956), from which the interdiffusion coefficient,  $\bar{D}$ , can be determined.

Isothermal heating experiments were conducted by Taylor et al. (31) to test the validity of interdiffusion coefficient determinations of Buening and Buseck (43) and Misener (42) for  $Fe^{++}$  and  $Mg^{++}$  diffusion between natural specimens of forsterite ( $FO_{92}$ ) and fayalite ( $Fa_{100}$ ). Chips from these phases were polished (1  $\mu m$  diamond compound in the last step), sized by sawing into 3 mm cubes, and joined together (with  $c$  axes parallel) across the cleaned, polished surfaces by placing them in  $Ag_{70}Pd_{30}$  foil, in turn wrapped with Pt wire. The reactants,  $FO_{92}$  and

Fa<sub>100</sub>, therefore, defined a diffusion couple for this experiment.

Two sets of experiments were designed in order to check for possible grain boundary effects upon diffusion of cation species between phases in the couple: (1) a sample, prepared as above, was sealed in an evacuated silica tube, duplicating the technique used by Misener; and (2) a free-floating silica rod, exerting a load of about 5 lbs/in<sup>2</sup> on the sample ("hot pressing") in the vertical position, was sealed in an evacuated silica tube. The loaded capsule was designed to minimize grain boundary effects upon cation diffusion rates.

Both charges were then heated at 1000°C for 311 hours, quenched, and examined with a binocular microscope to check the nature of the grain boundary contact surface. No apparent displacement along this surface could be discerned. Each couple was mounted in epoxy and a polished surface prepared such that the compositional profiles, measured with an automated, MAC 400S electron microprobe, were those across the center of the contact surface between forsterite and fayalite.

Optical observations of the fayalite in some experiments revealed evidence for noticeable oxidation of the fayalite to magnetite + silica. The experiments were consequently performed in triplicate. One set of charges were, in fact, subjected to heating at 400°C for 3 hours under a pumping vacuum prior to sealing of the silica tube. It would appear that some oxidation occurred late during the annealing process. In spite of these complications, compositional profiles away from the grain boundary into Fo<sub>92</sub> were obtained. The profiles are somewhat flatter than obtained



by Misener and about the same as calculated for  $fO_2 = 10^{-12}$  atm. from the data of Buening and Buseck. This indicates that the interdiffusion data by the latter authors is probably closer to correct. Also, no differences between profiles in the loaded and unloaded samples were detected. Therefore, the interdiffusion coefficient data for  $Fe^{++}$  and  $Mg^{++}$  as determined by the very thorough investigation of Buening and Buseck was used in the present study.

Concentration profiles in lunar samples 12002 and 15555 were measured by Taylor in conjunction with the development of the kinetic model presented in Chapter VIII. The applicability of the kinetic model is dependent upon a well-defined choice of phases from which a diffusion couple can be described. In the case of lunar samples 12002 and 15555, this entailed finding and measuring the compositions of olivines which had compositionally different cores and rims. The profiles across these grains, by necessity, had to flatten over cores and rims to ensure the reliability of cooling rate estimates from the data. Large, equant grains were chosen which exhibited differences in birefringence between rim and core (transmitted light, crossed polars). Several crystals were subjected to electron microprobe analyses in order to determine a grain with the largest compositional gradient. The regular geometries of the crystal cores and rims provided a means for choosing grains suspected of having symmetrical compositional profiles. Those grains containing melt or crystal inclusions were not chosen, since compositional gradients are perturbed in the vicinity of these inclusions.

Core and rim geometries and compositional profiles were defined by traversing each olivine grain such that compositional variations were known at all points on the grain. No measurable oscillatory or reversed zoning was present in any of the grains analyzed.

BIBLIOGRAPHY

1. Zachariasen, W.H.: J. Am. Chem. Soc. 54, 3841 (1932)
2. Zachariasen, W.H.: J. Chem. Phys. 3, 162 (1935)
3. Warren, B.E. and Biscoe, J.: J. Am. Ceram. Soc. 21, 49 (1938)
4. Adam, G. and Gibbs, J.H.: J. Chem. Phys. 43, 139 (1965)
5. Dietzel, A.: Glastechn. Ber. 22, 41 (1948)
6. Sun, K.H., and Huggins, M.L.: J. Phys. Chem. 51, 438 (1947)
7. Stanworth, J.E.: J. Soc. Glass Technol. 30, 56 (1946)
8. Uhlmann, D.R.: J. Non-Cryst. Solids, 7, 337 (1972)
9. Vreeswijk, J.C.A., Gossink, R.G. and Stevels, J.M.: J. Non-Cryst. Solids 16, 15 (1974)
10. Sarjeant, P.T. and Roy, R.: Matls. Res. Bull. 3, 265 (1968)
11. Dietzel, A. and Wickert, H.: Glastechn. Ber 29, 1 (1956)
12. Turnbull, D.: Contemp. Phys. 10, 473 (1969)
13. Jackson, K.A.: in Nucleation Phenomena. Am. Chem. Soc., Washington, 1966 pp. 37-40.
14. Suzuki, T. and Saito, S.: Mat. Res. Bull. 11, 221 (1976)
15. Uhlmann, D.R.: in Advances in Nucleation and Crystallization in Glasses, Am. Ceram. Soc., Columbus (1972) pp. 91-115
16. Christian, J.W.: The Theory of Transformations in Metals and Alloys. Pergamon Press, New York, 1965, pp. 399-405.
17. Avrami, M.: J. Chem. Phys. 9, 177 (1941)
18. Klein, L.: Ph.D. Thesis, MIT (1977)
19. Grange, R. and Keifer, J.M.: Trans. ASM 29, 85 (1941)
20. Uhlmann, D.R. and Chalmers, B.: in Nucleation Phenomena. Amer. Chem. Soc., Washington, 1966, pp. 1-13

21. Buckle, E. and Ubbelohde, A.R.: Proc. Roy. Soc. London A259, 325 (1961).
22. De Nordwall, H.J. and Staveley, A.K.: J. Chem. Soc., 224 (1954).
23. Thomas, D.G. and Staveley, A.K., J. Chem. Soc., 4569 (1952).
24. Turnbull, D. and Chech, R.E., J. Appl. Phys. 21, 804 (1950).
25. Hopper, R.W., Scherer, G., and Uhlmann, D.R.: J. Non-Cryst. Solids, 15, 45 (1974).
26. Hopper, R.W., Onorato, P., and Uhlmann, D.R.: Proc. of 5th Lunar Sci. Conf., Pergamon Press, New York (1974), pp: 2257-2273.
27. Hruby, A.: Czech J. Phys. B22, 1187 (1972).
28. Thornburg, D.D.: Matis. Res. Bull. 9, 1481 (1974).
29. Lasocka, M.: J. Matls. Sci. 11, 1771 (1976).
30. Simonds, C.H. Proc. 6th Lunar Sci. Conf., Pergamon Press, New York (1975), pp. 641-672.
31. Taylor, L.A., Onorato, P.I.K., and Uhlmann, D.R., Proc. 8th Lunar Sci. Conf., to be published.
32. Uhlmann, D.R. and Klein, L.C., Proc. 7th Lunar Sci. Conf., Pergamon Press, New York (1976), pp. 2529-2541.
33. Heiken, G.H., Butler, P., Phinney, W.C., Warner, J.L., Schmitt, H.H., Bogard, D.D., Simonds, C.H., and Pearce, G.W.: NASA TMX-58116 (1973).
34. Cadogan, P.H., and Turner, G.: Proc. 7th Lunar Sci. Conf., Pergamon Press, New York (1976), pp. 2267-2285.
35. Simonds, C.H., Warner, J.L., Phinney, W.C., and McGee, P.E., Proc. 7th Lunar Sci. Conf., Pergamon Press, New York (1976), pp. 2509-2528.
36. Carslaw, H.S. and Jaeger, J.C.: Conduction of Heat in Solids, Clarendon Press, London (1959), pp. 240-241.

37. Lovering, T.S.: Bull. Geol. Soc. Am., 46, 69 (1935).
38. Jaeger, J.C.: Amer. J. Sci., 255, 306 (1957).
39. Jaeger, J.C.: in The Poldervaart Treatise on Rocks of Basaltic Composition, John Wiley, New York (1968), pp. 503-536.
40. Provost, A., and Bottinga, Y.: Earth Planet Sci. Lett. 15, 325 (1972).
41. Walker, P., Kirkpatrick, R.J., Longhi, J., and Hays, J.F.:  
Geol. Soc. Amer. Bull. 87, 646 (1976).
42. Misener, J.D.: Ph.D. Thesis, Univ. Brit. Columbia (1973).
43. Buening, D.K. and Buseck, P.R.: J. Geophys. Res., 78, 6852 (1973).
44. Taylor, L.A., Uhlmann, D.R., Hopper, R.W., and Misra, K.C.: Proc. 6th Lunar Sci. Conf., Pergamon Press, New York (1975), pp. 181-191.
45. Cable, M.: Glasteknick Tidskrift, 25, 7 (1958).
46. Scholes, S.R. and Greene, C.H.: Modern Glass Practice, Cahners, Boston (1975), pp. 216-220.
47. Cable, M., Clarke, A.R., and Haroon, M.A., Glass Technol. 10, 15 (1969).
48. Karch, Z.: Sprechsaal Fuer Keramik Glas Email Silikate, 103, 427 (1970).
49. Kenworthy, R.: Silicates Ind., 37, 245 (1972).
50. Firth, E.M., Hodkin, F.W., and Turner, W.E.S.: J. Soc. Glass Tech., 11, 190 (1927).
51. Greene, C.H. and Gaffney, R.F.: J. Am. Ceram. Soc. 42, 271 (1959).
52. Greene, C.H. and Ktano, I., Glastech. Ber. B2K (1959) V/44-V/48.
53. Greene, C.H. and Lee, H.A.: J. Am. Ceram. Soc. 48, 528 (1965).
54. Boffe, M., Pecriaux, G., and Plumet, E.: in Symposium on nucleation and Crystallization in glasses and melts, Am. Ceram. Soc., Columbus, Ohio (1962), pp. 47-54.

55. Cable, M. and Haroon, M.A.: Glass Tech. 11, 48 (1970).
56. Cable, M.: Glass Tech., 2, 151 (1961).
57. Dalton, R.H.: J. Am. Ceram. Soc., 16, 425 (1933).
58. Baak, T., J. Am. Ceram. Soc., 42, 27 (1959).
59. Gehlhoff, G., Kalsing, H., and Thomas, M.: Glastechn. Ber. 8, 1 (1930).
60. Konijnendijk, W.L. and Buster, J.H.J.M.: J. Non-Cryst. Solids, 22, 379 (1976).
61. Nemec, L.: Glass Technol. 15, 153 (1974).
62. Lyle, A.K.: Fourth International Congress on Glass, Paris, paper II-4 (1956).
63. Bhuiyan, M.M. and Cable, M.: Glass Technol. 6, 206 (1965).
64. Okamura, T., and Uho, T., Res. Rep. Asahi Glass Co., 4, 1 (1954).
65. Greene, C.H. and Platts, D.R.: J. Am. Ceram. Soc. 52, 106 (1969).
66. Conroy, A.R., Manring, W.H., and Bauer, W.C.: The Glass Industry 84 (1966).
67. Conroy, A.R., Manring, W.H., and Bauer, W.C.: The Glass Industry 133 (1966).
68. Holmquist, S.: Phys. Chem. Glasses, 9, 32 (1968).
69. Swarts, L.: Bull. Am. Ceram. Soc.
70. Holmquist, S.: J. Am. Ceram. Soc. 49, 467 (1966).
71. Poole, J.P.: Proc. Int. Comm. on Glass, 212, 169 (1969).
72. Doremus, R.H.: J. Am. Ceram. Soc., 43, 655 (1960).
73. Readey, D.W. and Cooper, A.R.: Chem. Eng. Sci., 21, 917 (1966).
74. Cable, M.: J. Am. Ceram. Soc. 49, 436 (1966).
75. Cable, M. and Evans, D.J.: JAP 38, 2899 (1967).
76. Duda, J.L. and Vrentas, J.S., AIChE Journal, 15, 351 (1969).

77. Richards, R.S.: presented at 78th Annual Meeting of American Ceramic Society, Cincinnati, Ohio (1976).
78. Levich, V.G.: Physicochemical Hydrodynamics, Prentice-Hall, Englewood Cliffs, N.J. (1962), pp. 395-409.
79. Klein, L.C. and Uhlmann, D.R.: Proc. 7th Lunar Sci. Conf., Pergamon Press, New York (1976).
80. Onorato, P.I.K. and Uhlmann, D.R.: J. Non-Cryst. Solids, 22, 367 (1976)
81. Glasstone, S., Laidler, K.J., and Eyring, H.: The Theory of Rate Processes, McGraw-Hill, New York (1941).
82. Turnbull, D. and Cohen, M.H.: J. Chem. Phys. 52, 3038 (1970).
83. Gibbs, J.H. and DiMarzio, E.A., J. Chem. Phys. 28, 373 (1958).
84. Cukierman, M., Ph.D. thesis, M.I.T. (1972).
85. Laughlin, W.T. and Uhlmann, D.R., J. Phys. Chem. 76, 2317 (1972).
86. O'Keefe, J.D. and Ahrens, T.J., Proc. 6th Lunar Sci. Conf., Pergamon Press, New York (1975), pp. 2831-2844.
87. Floran, R.J., Phinney, W.C., Warner, J.S., Simonds, C.H., Jahn, B-M., Grieve, R.A.F., Dence, M.R., and Rhodes, J.M.: Geophys. Res. Lett.  
In press.
88. Masaitis, W.V., Mikhaylov, M.V., and Selivanouskaya, T.V.: Pub. of All Union Sci. Res. Geol. Inst. Nauk, Moscow, (1975), p. 124.
89. von Engelhardt, W., Geochim. Cosmochim. Acta, 31, 1667 (1967).
90. Stahle, V.: Earth Planet. Sci. Lett., 17, 275 (1972).
91. von Rosenberg, D.U.: Methods for the Numerical Solution of Partial Differential Equations, Elsevier, New York (1969).
92. Birch, F., Schairer, J.F., and Spicer, H.C., eds. Handbook of Physical Constants. Geological Society of America, Baltimore (1942).

93. Ahrens, T.J. and O'Keefe, J.A.: The Moon, 4, 214 (1972).
94. Horz, F.: Beitr. Mineral. Petrol. 11, 621 (1965).
95. El Goresy, A.: J. Geophys. Res. 70, 3453 (1965).
96. Hammersley, J.M. and Hanscomb, D.C.: Monte Carlo Methods, John Wiley, New York (1965), pp. 39-40.
97. Simonds, C.H., Warner, J.L., Phinney, W.C., McGee, P.E., and Floran, R.J. (1977), to be published.
98. Lofgren, G.E., Donaldson, C.H., Williams, R.J., Mullins, D.F., and Usselman, T.: Proc. 5th Lunar Sci. Conf., Pergamon Press, New York (1974), pp. 549-567.
99. Lofgren, G.E., Usselman, T.M., and Donaldson, C.H.: abstract in Lunar Science VI, Lunar Science Institute, Houston (1975), pp. 515-517.
100. Lasaga, A.C., and Richardson, S.M.: Eos Trans. AGU, 56, 459 (1975).
101. Hopper, R.W. and Uhlmann, D.R.: J. Geophys. Res., 81, 5721 (1976).
102. Taylor, L.A. and McCallister, R.H.: Earth Planet Sci. Lett. 17, 105 (1972).
103. Crank, J.: The Mathematics of Diffusion, Clarendon Press, Oxford (1956).
104. Medaris, L.G., Jr.: Amer. J. Sci., 267, 945 (1969).
105. Sato, M., Hickling, N.L., and McLane, J.E.: Proc. 4th Lunar Sci. Conf., Pergamon Press, New York (1973), pp. 1061-1079.
106. Bianco, A.S. and Taylor, L.A.: Abstract in Lunar Sci. VIII, Lunar Science Institute, Houston (1977), pp. 103-105.
107. Walker, D., Longhi, J., Lasaga, A.C., Stolper, E.M., Grove, T.L., and Hays, J.F., to be published in Proc. 8th Lunar Sci. Conf. (1977).
108. Doremus, R.H.: Glass Science, Wiley, New York (1973).



109. Bottinga, Y., and Weill, D.F.: Am. J. Sci., 272, 438 (1972).
110. Shaw, H.R.: Am. J. Sci., 272, 870 (1972).
111. Cukierman, M., Klein, L., Scherer, G.W., Hopper, R.W., and Uhlmann, D.R.: Proc. 4th Lunar Sci. Conf., Pergamon Press, New York (1973), p. 2685.
112. Klein, L., Onorato, P.I.K., Uhlmann, D.R., and Hopper, R.W.: Proc. 6th Lunar Sci. Conf., Pergamon Press, New York (1975), p. 579.
113. Uhlmann, D.R., Klein, L., Kritchevsky, G., and Hopper, R.W.: Proc. 5th Lunar Sci. Conf., Pergamon Press, New York (1974), p. 2317.
114. Uhlmann, D.R., Klein, L.C., Pettyjohn, C.H.: Proc. 8th Lunar Sci. Conf., to be published.
115. Cukierman, M., Tutts, P.M., and Uhlmann, D.R.: Proc. 3rd Lunar Sci. Conf., MIT Press, Cambridge (1972), p. 2619.
116. Scherer, G., Hopper, R.W., and Uhlmann, D.R.: Proc. 3rd Lunar Sci. Conf., MIT Press, Cambridge (1972), pp. 2627-2637.
117. Uhlmann, D.R. and Klein, L.C.: Proc. 7th Lunar Sci. Conf., Pergamon Press, New York (1976), pp. 2129-2131.
118. Cukierman, M. and Uhlmann, D.R.: J. Geophys. Res. 78, 4920 (1973).
119. Klein, L., and Uhlmann, D.R.: J. Geophys. Res., 79, 4869 (1974).
120. Meiling, G.S. and Uhlmann, D.R.: Phys. Chem. Glasses 8, 62 (1967).
121. Scherer, G.W.: S.M. Thesis, MIT (1972).

BIOGRAPHICAL NOTE

Paulette Irene Kantor was born in Chicago on January 2, 1951. She attended Roosevelt High School before entering MIT in September, 1968. In June, 1972 she received the degree of Bachelor of Science from the Department of Metallurgy and Materials Science. The following year was spent at the Centre National de la Recherche Scientifique in Vitry-sur-Seine, France through the generosity of the Rotary Foundation. In September 1973 she entered graduate school at MIT. On January 6, 1974 she married Joseph Onorato. For three years she was the recipient of the Owens-Illinois Fellowship in Materials Science. Her work has resulted in the following publications:

Onorato, P.I.K., and Uhlmann, D.R., "Nucleating heterogeneities and glass formation", J. Non-Cryst. Sol., 22, 367 (1976).

Onorato, P.I.K., Uhlmann, D.R., and Simonds, C.H., "Heat flow in impact melts: Apollo 17 Station 6 Boulder and some applications to other breccias and xenolith laden melts", Proc. Lunar Sci. Conf. 7th, 2449 (1976).

Onorato, P.I.K. and Uhlmann, D.R., "The moving shrinking bubble in a glass melt", paper presented at 78th Annual Meeting of the American Ceramic Society, May, 1976, Cincinnati, Ohio.

Klein, L., Onorato, P.I.K., Uhlmann, D.R., and Hopper, R.W., "Viscous flow, crystallization behavior, and thermal history of lunar breccias 70019 and 79155", Proc. Lunar Sci. Conf. 6th (1975) pp. 579-593.

Uhlmann, D.R., Klein, L., Onorato, P.I.K., and Hopper, R.W., "The formation of lunar breccias: Sintering and crystallization kinetics", Proc. Lunar Sci. Conf. 6th (1975) pp. 693-705.

Hopper, R.W., Onorato, P., and Uhlmann, D.R., "Thermal histories and crystal distributions in partly devitrified lunar glasses cooled by radiation", Proc. Lunar Sci. Conf. 5th (1974) pp. 2257-2273.

Kantor, P., Revcolevschi, A., and Collongues, R., "Preparation of iron sesquioxide glasses by ultra-fast quenching from the melt", J. Mat. Sci. 8 (1973) pp. 1359-61. Also presented at International Colloquium on Amorphous and Vitreous Systems, Chemical Society of Belgium, Charleroi, April, 1973, and published in the proceedings of that meeting.

Schmid, F., Viechnicki, D., and Kantor, P.I., "Reaction of MgO in  $\text{MgAl}_2\text{O}_4$  spinel with molybdenum crucibles during crystal growth", J. Appl. Phys. 44 [5], 1973, pp. 2417-18.